Novel Application of Phase Change in Thermal Management of Power Electronics

Yiyi Chen, BEng.

Thesis submitted to the University of Nottingham for the degree of Doctor of Philosophy

September 2019

Abstract

Thermal management is a crucial step in the design of almost all industries such as renewable energies, processors, space, transportation, food and beverage industries. It involves controlling the temperature by means of heat transfer, conduction, convection, radiation and transfer of energy by phase changes, etc. In the automotive applications, the insulated gate bipolar transistor (IGBT) power module is one of the most important components in the power supply and motor control circuits in hybrid electric vehicles (HEV) and electric vehicles (EV). Nowadays, the heat dissipation density of IGBT is continuously increasing due to power rating improvements and miniaturisation. Without suitable cooling technologies, excessively high temperature and uneven temperature distribution can cause high thermal stress, eventually leading to severe module failures such as solder-ceramic delamination and crack as well as bonding wire lifts off. Therefore, highly efficient and compact cooling solutions are required. In thermal management design, boiling processes are very widely applied in many technical applications such as cooling technology, the chemical industry, power plant technology, refrigeration engineering, etc. To enhance boiling heat transfer, a pool boiling experiment was carried out. Copper surfaces with different channel sizes were used as boiling surfaces. Fe_3O_4 and polydimethylsiloxane (PDMS)-silica nanoparticles were used to be deposited on the surfaces. These two nanoparticles are able to modify the surface energy, which further causes changing in surface wettability. The surface contact angles become 14^o and 145^o after Fe_3O_4 and PDMS-silica nanoparticles were coated on surfaces, respectively. The maximum heat transfer coefficient found upon heterogeneous, hydrophobic and hydrophilic wetting surfaces are 81.5 kW/m^2K,

77.4 kW/m^{2}K, 50.4 kW/m^{2}K, respectively, which are much higher than the 32.2 kW/m^{2}K of the plain copper surface. To present a better understanding of the boiling enhancement mechanism of heterogeneous wetting channel surfaces, high-speed visualisations were used to observe bubble dynamics including nucleate site density, bubble departure diameter, bubble growth rate. Also, an experimental investigation was carried out to investigate the effect of channel width on boiling heat transfer of the heterogeneous wetting surface. Four channel widths-600 µm, 1000 µm, 2000 µm, and 2500 µm were selected. The heat transfer coefficient of 110.3 kW/m^{2}K was obtained on the heterogeneous wetting surface with channel width of 600 µm. The enhancement ratio of heat transfer coefficient reached up to 35 %, 39 %, 45 % and 242 % compared with the surface with channel width of 1000 µm, 2000 µm, 2500 µm, and plain copper surface. This enhancement was mainly attributed to the increase the actural surface area, capillary-assisted suction ability, hydrophobic area percentage and reducing bubble base diameter.

In application of phase change in thermal management of power electronics, the aim is to develop a cooling solution to quickly transfer high heat flux and reduce the temperature gradient of the IGBT power module. The cooling solution based on vapour chamber in which phase change directly takes place was developed and analysed. The experiments and simulation confirmed that both the thermal and thermo-mechanical performances of IGBT with the novel designed are better than that of the IGBT with copper baseplate module. The experiment mainly analysed temperature distribution in layers, junction temperature, temperature uniformity and thermal resistance. The simulation study focused on thermo-mechanical performances of IGBT such as thermal stress, deformation,

creep and plastic strain energy dissipation and predicting thermal fatigue life. It also studied the failure mechanism under power cycling.

Publication

Chen Y, Li B, Wang X, et al. Investigation of heat transfer and thermal stresses of novel thermal management system integrated with vapour chamber for IGBT power module [J]. Thermal Science and Engineering Progress, 2019, 10: 73-81

Chen Y, Li.B, Wang X, et al. Vapour chamber direct phase change cooling of an IGBT power electronic module for automotive application. IEEE Transaction on Power Electronics [Under review]

Chen Y. Hann D. Yan Y, et al. Enhanced pool boiling heat transfer on nanoparticles-coated heterogeneous wetting channel surfaces. International Journal of Heat and Mass Transfer [Submitted]

Fu R, Liu Z, Chen Y, et al. Experimental investigation of turbulent forced heat transfer of Fe3O4 ethylene glycol–Water nanofluid with highly disaggregated particles [J]. Thermal Science and Engineering Progress, 2019, 10: 1-9.

Fu R, Yan Y, Roberts C, Liu Z, Chen Y. The role of dipole interactions in hyperthermia heating colloidal clusters of densely-packed superparamagnetic nanoparticles [J]. Scientific reports, 2018, 8(1): 4704.

Chen Y, Li B, Yan Y, et al. Modelling and Experimental Analysis of Heat Transfer for Power Electronic Module Integrated with Phase Change Thermal Management System [C]. International Heat Transfer Conference Digital Library. Begel House Inc., 2018.

Chen Y, Yan Y, Li B, et al. Thermal Characterization Analysis of IGBT Power Module Integrated with a Vapour Chamber and Pin-Fin Heat Sink[C]//PCIM Europe 2017; International Exhibition and Conference for Power Electronics,

Intelligent Motion, Renewable Energy and Energy Management. VDE, 2017: 1-8.

Acknowledgement

Firstly, I would like to express my deepest thanks to my PhD supervisors Prof. Yuying Yan and Dr. David Hann. Prof. Yuying Yan is always supportive and given me useful advice related to both my study and life. Thanks for his broad knowledge in each topic. I enjoyed the time working in his research group. Dr. David Hann was always available for research discussions and his encouragements were very beneficial to my study. I am deeply grateful for their help.

I would like to thanks Prof. David Reay from Newcastle University for inspiring discussions and for his very helpful feedback on my thesis.

I also would like to thanks Dr. Bo Li, for assistance in building the test rig, publishing papers and providing useful advice during my PhD study. Thanks also go to my colleagues and friends for giving me a great experience at university. Thanks for the fun times spent together.

Next, I would like to thank the technicians of the lab, Tony and Andy, who were always on hand for technical assistance and for helping me with any problems with my test rig.

My special thanks to Prof. Li Yong from South China University of Technology for his kind help.

Last, but not least, I would like to thank my mom and dad for supporting and encouraging me.

Table of Contents

List of Table

List of Figure

Nomenclature

Acronyms	Description
CU	Copper
DBC	Direct bonded copper
EV	Electric vehicle
IGBT	Insulated-gate bipolar transistor
MOSFET	Metal oxide semiconductor field-effect transistor
TIM	Thermal interface material
VC	Vapour chamber

Symbol	Description	Units
A	Creep rate coefficient	s^{-1}
A_c	Surface area	m^2
$B_{pix,hs}$	Camera resolution	m/pixel
Bo	Bond number	
C	Fourth order elasticity tensor	
C_p	Heat capacity	J/kg/K
C_{pl}	Heat capacity of liquid	J/kg/K
D	Duty ratio	
D_c	Diameter of cavity mouth	mm
D_b	Equivalent bubble departure diameter	mm
D_i	Bubble diameter	mm
$E_{SW(ON)}$	Switching on loss of IGBT	W
$E_{SW(OFF)}$	Switching off loss of IGBT	W

E_{rec}	Recovery loss	W
f	Bubble emission frequency	Hz
f_s	Switching frequency	Hz
F_b	Buoyancy force	N
F_{cp}	Contact pressure force	N
F_d	Drag force	N
F_i	Inertia force	N
F_s	Surface tension	N
h	Heat transfer coefficient	W/m^2K
I	Current	A
I_c	Current, collector	A
I_{cp}	Peak value of output current	A
Ja	Jacob number	
k	Thermal conductivity	W/mK
k_l	Thermal conductivity of liquid	W/mK
l	Thickness	m
L_c	Capillary length	m
m	Fatigue energy exponent	
n	Garofalo n parameter	
N_a	Nucleation sites density	$Sites/cm^2$
N_f	Fatigue cycles	
I_{CP}	Peak value of output current	A
P_{DC}	Conduction loss from diode	W
P_{rec}	Recovery loss of diodes	W
P_{SS}	Conduction loss from IGBT	W

P_{SW}	Switching loss	W
q_s	Volumetric heat generation	W/m^3
q	Heat flux	W/cm^2
Q	Heat input	W
ΔQ	Activation energy	J/mol
R	Thermal resistance	K/W
R_c	Radius of cavity mouth	m
R_g	Gas constant	J/molK
R_{CU}	One dimensional thermal resistance of copper	K/W
R_{VC}	One dimensional thermal resistance of vapour chamber	K/W
$R_{th(b-a)}$	Thermal resistance of heat sink	K/W
$R_{th(j-a)}$	Total thermal resistance	K/W
$R_{th(j-b)}$	Thermal resistance between chip and baseplate	K/W
R_{VP}	Thermal resistance of vapour chamber	K/W
R_{1D}	One-dimensional thermal resistance	K/W
T	Temperature	˚C
T_a	Cooling media temperature	˚C
T_b	Condenser surface of vapour chamber/copper temperature	˚C
T_t	Evaporation surface of vapour chamber/copper temperature	˚C
T_j	Junction temperature	˚C
T_{wall}	Tested surface temperature	˚C
t	Time	s

t_{growth}	Bubble growth time	s
$t_{waiting}$	Waiting time	s
v_g	Specific volume for air	m^3/kg
v_l	Specific volume for liquid	m^3/kg
V_b	Bubble volume	m^2
$V_{CE(SAT)}$	Forward voltage drop in IGBT	V
V_{off}	Voltage drop during OFF period	V
V_f	Forward voltage drop in the diode	V
W_f'	Fatigue energy coefficient	
ΔW_{cr}	Creep strain energy density	mJ/m^3
ΔW_{in}	Inelastic strain energy density	mJ/m^3
ΔW_{pl}	Plastic strain energy density	mJ/m^3
Δx	Distance between two adjacent thermocouples	m
cosϕ	Power factor	
:	Double-dot tensor product	

Greek	**Description**	**Units**
α	Thermal diffusivity	m^2/s
ε	Strain	
ε^{cr}	Equivalent uniaxial creep strain	
ε_{el}	Elastic strain	
ε_{in}	Inelastic strain	
θ	Contact angle	degree
σ	Surface tension	mN/m
λ	Thermal conductivity	W/mK

μ	Viscosity	Kg/ms
π	Ratio of a circle's circumference to its diameter	
ρ	Density	kg/m^3
ρ_l	Liquid density	kg/m^3
ρ_v	Vapour density	kg/m^3

1. Introduction

1.1 Motivation and objective

The power electronics become ever more important to many energy systems such as hybrid electric vehicles and electric vehicles. The insulated gate bipolar transistor (IGBT) power module as a power switching transistor device is one of the most important components for the development of higher voltage and current ratings. However, the heat dissipation density inevitably increases with increased power rating and reduced package size. Therefore, better designs of cooling systems are required to achieve higher heat dissipation. Cooling solutions with phase change are good choices to meet the needs of high heat flux of power modules.

For a vapour chamber heat sink, the heat transfer rate is high due to the evaporation/boiling and condensation processes. In the boiling heat transfer process, the boiling heat transfer coefficient depends on the bubble dynamics including bubble nucleation, bubble growth, nucleation site density, bubble diameter and interactions between adjacent bubbles. Hence, to enhance thermal performance during the boiling process, a fundamental understanding of bubble dynamics is required.

In this thesis, there are two main objectives. The first objective is to develop an experimental method for the investigation of heat transfer processes in pool boiling. In particular, it mainly investigated how different degrees of surface wettability on channels affect bubble dynamics in pool boiling. The second objective is to improve the operational reliability of IGBT power modules by integrating the design of the module with a cooling solution and applying phase

change heat transfer in cooling systems. The objectives and goals of these two major portions of this thesis are listed below.

1. Enhanced pool boiling heat transfer on nanoparticles-coated heterogeneous wetting micro-channel surfaces
   1.1 Building pool boiling test rig
   1.2 Fabrication of the surface with hydrophilic, hydrophobic and heterogeneous wetting pattern
   1.3 Quantifying the enhancement of heat transfer coefficient
   1.4 Bubble growth dynamics on homogeneous and heterogeneous wetting surface
   1.5 Effects of channel width on boiling heat transfer
2. Investigate thermal and thermo-mechanical performance of IGBT with integrated vapour chamber
   2.1 Design the IGBT electronics power module with vapour chamber cooling structure
   2.2 Fabrication of the IGBT power module integrated with vapour chamber module
   2.3 Experimental study of thermal performance including junction temperature, temperature uniformity, thermal resistance and heat transfer coefficient.
   2.4 Evaluating thermo-mechanical performances of IGBT power module and predicting thermal fatigue life under power cycling
   2.5 Analysis of the failure mechanism of the IGBT power module

1.2 Thesis structure

This thesis addresses the cooling of the IGBT power electronics and enhancement of nucleate pool boiling by controlled wettability pattern. Two sections are presented in Chapter 2. Firstly, it provides overviews of bubble dynamics in nucleate boiling and enhancement mechanisms related to surface wettability. Secondly, it analyses the significance of thermal management for power electronics and failure mechanisms regarding to the temperature. The power electronics module with different cooling techniques available in the market are summarised and discussed. Chapter 3 describes the experimental setup, preparations of boiling surface and results from the systematic study of nucleate pool boiling. The results are analysed in detail to understand the boiling enhancement mechanisms by surface wettability and channel width modification. Chapter 4 presents the design of new structure of IGBT power module. The experimental and simulation results are used to examine the thermal and thermo-mechanical performance. Finally, a summary of the thesis with concluding remarks and future work are presented in Chapter 5.

2. Literature review

In this chapter, two parts were reviewed. The first section presents a review of the previous research that has been conducted to study the pool boiling on a small length scale with vapour bubble growth dynamics. In particular, it focused on how surface wettability affects nucleate boiling thermal performance in the aspect of bubble dynamics. The second section gave an overview of the IGBT power modules. Future trends, challenges and module failure mechanisms were described. The conventional power module cooling solutions were analysed regarding advantage and disadvantages listed for each. The thermal problem is identified including optimisation of cooling of IGBT power modules to improve the module reliability and module performance.

2.1 Pool boiling enhancement on modification of wettability surface

Thermal management of high-power electronics has become more challenging as heat dissipation density increases. It is difficult for the conventional cooling solutions to handle high heat flux. Phase-change cooling is one of the most efficient cooling solutions for high heat flux cooling, since the heat transfer coefficient can reach 100 kW/m^2K due to phase change[1]. Therefore, the phase-change cooling solutions have been widely used in many applications such as heat exchangers and power electronics.

In this section, it presented a review of the previous researches that have been conducted to study pool boiling on a small length scale as well as vapour bubble growth dynamics. In the boiling process, four different boiling regimes are observed including natural convection boiling, nucleate boiling, transition boiling and film boiling, as shown in Figure 1. Generally, nucleate boiling

attracts the most attentions due to the high heat flux at low superheat. For thermal management, a requirement is to obtain lower superheat, high heat transfer coefficient, and to limit device junction temperature. Therefore, the enhancements of pool boiling heat transfer have been investigated for several decades.

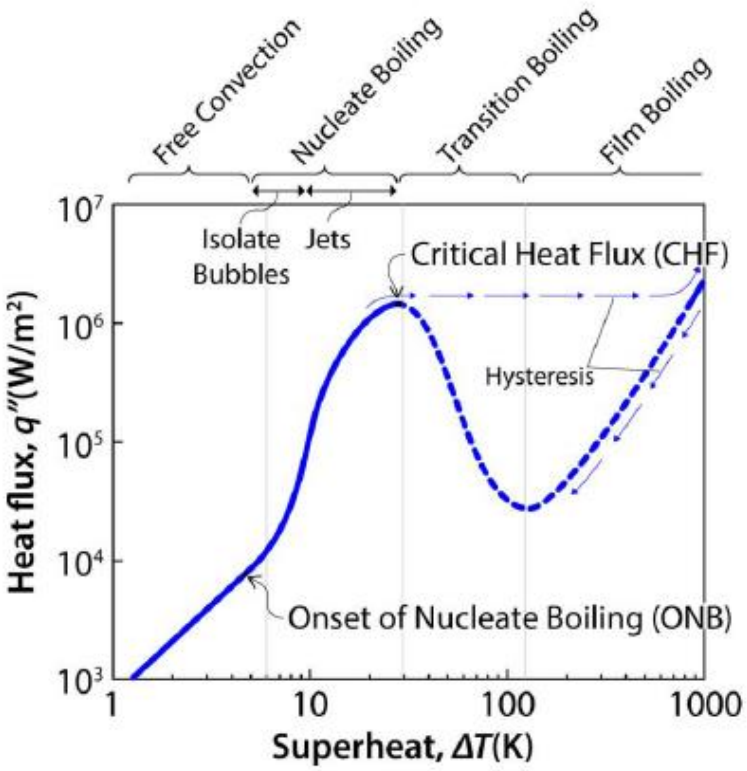

Figure 1 Pool boiling curve for saturated water[2]

As for the application of boiling heat transfer, heat pipes/ vapour chamber are regarded as super heat transfer devices, which use the latent heat of the working fluid for efficient heat transfer over a very small temperature drop to transfer large amounts of heat. High conductivity, passive operation, flexible size and minimum maintenance make heat pipe utilisable a widely used heat transfer material. With rapidly increasing heat emission density of heat source components such as semiconductor components in the electronics, the cooling

capacity of the thermal management system also needs to be improved to meet the requirement.

In order to improve the thermal performance of the wick structure, many researchers work on thermal resistance reduction by altering porosity, thickness, and the structure design [3-6], but less attention is paid to the micro nucleate boiling in wicks. In standard heat pipe operation, heat transfer is primarily conducted by conduction and convection under a low heat flux meanwhile menisci are formed at the wick to working fluid interface. With increasing the heat flux, the menisci recede into the wick surface due to the evaporation at the liquid vapour meniscus. As heat flux increases further, a higher wick superheat temperature leads to incipience of bubbles in the wick structure and nucleate boiling becomes the dominant mode of heat transfer. The heat transfer in the evaporation section mainly depends on nucleate boiling due to the much higher heat transfer coefficient [7]. Therefore, a good understanding of the nucleate boiling process and the effects of wick parameters on boiling is important for designing superior wick structures. To evaluate thermal performance of a wick structure, most researchers in this area out by test actual heat pipes and calculate the heat transfer coefficient. However, it didn't provide the detailed local phase change process by this means. Recently, novel approaches for characterising thermal performance of a wick structures are developed. Chen [4] put a heated wick sample into a sealed vapour containment vessel and investigated the parameters affecting heat transfer coefficient and critical heat flux during evaporation/boiling process. A similar experiment was performed by Gerardi[8] and the boiling on the heated wick was clearly observed by high speed infrared and visible cameras.

It is well known that heat transfer characteristics in nucleate boiling depends on wall superheat, bubble surface area, and the number of active nucleate sites[9, 10]. Many researchers investigated the micro phenomena during nucleate boiling and presented that nucleated boiling performance can be enhanced by modifying wettability of heated surfaces. Lots of works investigated the effect of surface wettability on boiling heat transfer and bubble dynamic [11-19]. However, the enhancement mechanism is still not clear, mainly because it is difficult to change the surface contact angle with whilst other parameters kept constant. For example, using a surfactant solution as the working fluid is a traditional approach to reduce surface contact angle and enhance wettability, but the surface tension is altered too. Oxidising the metal is another traditional way to modify the surface contact angle, but it may also change the surface roughness at the microscale. Takata[20], Mitsutake [21]and Sun [22] used the TiO_2 photocatalysis method to vary surface contact angle. The contact angle on a TiO_2 coated surface is irradiated by UV light. Although this method can provide the surface with high wettability, the stability is limited and the hydrophilic ability can disappear when it is stored in dark. Recently, nanofabrication on the boiling surface becomes a promising technology for enhancing boiling heat transfer. Many kinds of nanostructures came up with such as deposited nanowires, nanotubes and nanograss. Nanoparticle coating is efficient to modify the surface contact angle in a large range meanwhile it barely alters the surface topography at the microscale. Phan [23] controlled the changed contact angle in the range, ranging from 22º to 112º by using different nanoparticles for the surface deposition. The boiling heat transfer performance can be different with surface wettability. Compared with hydrophilic wetting surface, hydrophobic wetting

surface have an earlier onset of nucleate boiling, resulting in a better thermal performance at low heat flux. However, it reaches critical heat flux easily since the bubbles take a longer time to detach the surface due to the high affinity to the surface. In contrast, a hydrophilic surface treatment could rise the critical heat flux because of the reduced affinity, but it may not benefit the onset of the nucleate boiling since the nucleation becomes harder. Therefore, it is difficult for a homogeneous wetting surface to optimize the boiling heat transfer at both low and high heat flux.

Heterogeneous wetting surface, a mix of hydrophobicity and hydrophilicity, has received many attentions for improving the boiling thermal performance. Such a surface adopts the advantages of both hydrophobic and hydrophilic surfaces due to the synergistic effects. It can initiate the bubble nucleation early and delay the critical heat flux, thus enhancing the thermal performance at all regimes of the boiling process. Generally, a heterogeneous wetting pattern combined with multiscale surface structure improves bubble nucleation and bubble dynamics including liquid and vapour transport. Jo [11]fabricated a heterogeneous wetting pattern with self-assembled monolayer patterns onto the heads of micro-post. The results suggested that the boiling heat transfer was enhanced without deteriorating the critical heat flux. Kumar [24]produced a heterogeneous wetting surface by printing hydrophobic polymer patterns and deposited SiO_2 nanoparticles. A 98.5% of enhancement in heat transfer coefficient was obtained when the surface was with hydrophobic patterns and the deposition of a superhydrophilic SiO_2 nanoparticles.

To figure out the enhancement mechanism of nucleate pool boiling by wettability modification, Fritz [25] made a model to predict the relationship

between wettability and bubble departure diameter for nucleate pooling boiling. Pan[23] controlled surface wettability by nanocoating and studied the effects on nucleation mechanism. Son G.[26] Malla[27], Suroto[15], Betz[18] studied bubble emission frequency and active nucleate sites density at different surface wettability. O`Hanley et al. [28] suggested that a porous hydrophilic surface can delay the critical heat flux significantly and Betz[29] analysed the heat transfer coefficient at different heat flux and wettability. However, the effects of wettability on the heterogeneous nucleate boiling are not fully understood and there is still no identity agreement on many related aspects due to lack large amounts of experimental data. Actually, it is hard to change the contact angle but with whilst keeping all other parameters constant during an experiment. For instants, one conventional method to vary the liquid contact angle is the surfactant solution. Wen and Wang [12]observed that surfactant could enhance the heat transfer coefficient by increase wettability. However, reduction in surface tension and an increase in wettability can occur simultaneously during the surfactant process. Oxidising copper is another widely used method to change the wettability. According to Liaw and Dhir[30], they found oxidising copper can modify surface topography which is related to nucleate site. Therefore, it is difficult to make a conclusion that only wettability affects boiling heat transfer rather than other parameters. In this section, it summarises and evaluates bubble dynamics, emission frequency, active nucleate sites density, critical heat flux and heat transfer coefficient under varied wettability of boiling surfaces.

2.1.1 Bubble departure diameter

Bubble departure diameter is defined as the diameter of a bubble at the moment that bubble departs the heated surface. Many studies have been conducted on the correlations for prediction of the bubble departure diameter sizes, however, fewer researches directly revealed the relationship between bubble diameter and heat transfer capacity. Li[4] found that optimal evaporation/boiling heat transfer performance occurs when the bubble departure diameter is larger than wick thickness. Under this condition, no bubble will depart from the heated surface and no bubble flow inside the capillary wick structure, causing bubble generation frequency to be significantly enhanced without the increase in the time needed for the bubbles to depart. According to this observation, increasing bubble departure diameter is a way to enhance evaporation/boiling heat transfer performance.

Until now, the analytical description of bubble departure diameter during a boiling has been not satisfactorily resolved. Chen et al. [31]summarised the most used correlation conducted shown in Table 1. With regard to all correlations of bubble departure diameter, they can be divided into two parts, one includes the term of$\left(\frac{\sigma}{g(\rho_l-\rho_v)}\right)^{\frac{1}{2}}$, and the other doesn't include it. Many researchers have tried to relate the first part$\left(\frac{\sigma}{g(\rho_l-\rho_v)}\right)^{\frac{1}{2}}$. With regards to the first part, many researchers such as Fritz[25], Ruckenstein[32], Cole[33], Cole and Rohsenow[34], Kutateladze and Gogonin[35], Jensen and Memmel[36], Kim and Kim[37], Fazel and Shafaee[38] et al. Although many correlations have been established for prediction of bubble departure diameter for nucleate pool boiling under

different conditions, none of these theories predict an appropriate data trend, nor explain the reason efficiently.

Table 1 Correlations for bubble departure diameter

Reference	Correlation
Fritz [25]	$D_b = 0.0208\theta\sqrt{\frac{\sigma}{g(\rho_l-\rho_v)}}$ For pure liquid and mixtures
Ruckenstein [32]	$D_b = \left[\frac{3\pi^2\rho_l\alpha_l^2 g^{\frac{1}{2}}(\rho_l-\rho_v)^{\frac{1}{2}}}{\sigma^{\frac{3}{2}}}\right]^{\frac{1}{3}} Ja^{\frac{4}{3}}\sqrt{\frac{\sigma}{g(\rho_l-\rho_v)}}$ Not specified of liquid
Cole [33]	$D_b = 0.04Ja\sqrt{\frac{\sigma}{g(\rho_l-\rho_v)}}$ For pure liquid and mixtures
Cole and Rohsenow [34]	$D_b = C\sqrt{\frac{\sigma}{g(\rho_l-\rho_v)}}Ja^{C\frac{5}{4}}$ Where C is 1.5×10^{-4} for water, 4.65×10^{-4} for others
Kutateladze and Gogonin [35]	$D_b = 0.25(1+10^5K_1)^{\frac{1}{2}}\sqrt{\frac{\sigma}{g(\rho_l-\rho_v)}}$ $K_1 = \left(\frac{Ja}{\mathrm{Pr}_l}\right)^2 Ar^{-1}$ for $K_1 < 0.06$ For pure liquid and mixtures
Jensen and Memmel [36]	$D_b = 0.19(1.8+10^5K_l)^{\frac{2}{3}}\sqrt{\frac{\sigma}{g(\rho_l-\rho_v)}}$ For pure liquid and mixtures
Kim and Kim [37]	$D_b = 0.1649Ja^{0.7}\sqrt{\frac{\sigma}{g(\rho_l-\rho_v)}}$ For R113
Fazel and Shafaee [38]	$D_b = 40\left(\frac{\mu_v q}{\rho_l h_{lv}\sigma cos\theta}\right)^{\frac{1}{3}}\sqrt{\frac{\sigma}{g(\rho_l-\rho_v)}}Ja^{C\frac{5}{4}}$ For electrolyte solutions

In order to investigate the effect of surface wettability on bubble departure diameter, Fritz model as the first and classical model based on surface tension and buoyancy force, which directly indicates the wettability effect [39].

$$D_b = 0.0208\theta \sqrt{\frac{\sigma}{g(\rho_l - \rho_v)}} \; for \; \theta \leq 90^o \tag{1}$$

He found that the bubble departure diameter reduces when wettability of the heated surface is higher. This equation only considers buoyancy and surface tension while ignoring inertia and drag forces which depend on bubble growth velocity during the bubble departure. Also, the Fritz correlation was obtained only based on very limited the experimental findings on hydrophilic surfaces. He didn't publish this correlation in the original publication because there is a difference between the apparent bubble diameter and the equivalent diameter for a spherical bubble of the same volume. Until now, the relationship between contact angle and bubble diameter has not been validated by large amounts of experimental data. After Fritz, many researchers modified his model by considering for more factors such as pressure, Jacob number and bubble growth velocity to improve accuracy and reliability. Son and Dhir[26] were analysed the effect of static contact angle and wall superheat on bubble dynamics by means of numerical simulation and experiment of a growing departing bubble. The results showed that the bubble departure diameter became larger when the contact angle or wall superheat increased. They also gave the detailed explanation that the vapour volume required for bubble departure diameter increased due to the increase in surface tension for higher contact angle.

On the contrary, Jo[16] combined micro-post structure and self-assembled monolayers to form a mixed wetting surface. The results showed the surface generated bubble with a small departure diameter although the wettability was high. This could be caused by the effects of surface topography that surface resistance on the micro-post structure could restrict the increase of bubble diameter. Phan[23] observed the bubble formation on different wettability surface produced surfaces by a nanocoating method and drew a conclusion conflicting with Fritz. He observed that the bubble diameter increased with a reduction in static contact angle under a constant heat flux condition for hydrophilic surfaces. He supposed that there were not sufficient experiments under the conditions, in which only the surface wettability changed, to validate Fritz's correlation. Additionally, the Fritz correlation was concluded by measurement with air bubbles rather than vapour bubbles in boiling condition. Based on his experimental results, the original Fritz equation was modified by considering the energy factor which is believed to be the key parameter of the effects of the wetting on bubble growth. Energy factor is defined as the ratio of the energy needed to form a bubble with a contact angle θ on the surface to that needed to form a homogenous bubble with the same diameter. In other words, it is the volume ratio of the sphere which has a constant angle θ on the surface and the full sphere which has the same diameter. Its expression is given by:

$$f(\theta) = \frac{2 + 3cos\theta - \cos^3\theta}{4} \tag{2}$$

And the new bubble diameter correlation is given by

$$D_b = 0.626977 \times \frac{2 + 3cos\theta - \cos^3\theta}{4} \sqrt{\frac{\sigma}{g(\rho_l - \rho_v)}}, for\ \theta \leq 90^o \tag{3}$$

This new correlation fits most of the experimental data with a maximum error of 25%. However, this correlation has an inverse relationship with the Fritz equation.

2.1.2 Bubble emission frequency

The growing bubble absorbs heat from the microlayer close to the three-phase contact line through evaporation, the leading to a reduction in the vicinity of nucleate site showing a temperature. After the bubble grows big enough, the increased buoyancy makes it depart from the heating surface. The nucleate site with dropped temperature needs a recovering or waiting process until the temperature reaches the value; making a new subsequent bubble form again. Based on the micro-convection model from Mikic and Rohsenow[40], the heat transfer coefficient is proportional to the square root of the frequency of bubble departure. This could be explained by more heat being carried away and enhanced turbulence at a high frequency[41]. The bubble emission frequency can be defined as the number of bubbles departed over time and described as

$$f = \frac{1}{t_{growth} + t_{waiting}} \tag{4}$$

t_{growth} and $t_{waiting}$ represent the duration of bubble growth and duration between the departure of the former bubble and appearance of current bubble.

Table 2 summarises the bubble departure frequency. It can be found that most of them correlate with bubble departure diameter and it can be in the form of

$$fD^m = f(\rho_l, \rho_v g, \alpha_1, Ja) \tag{5}$$

Where m is an empirical number. fD^m mainly depends on vapour and liquid density, gravity, thermal diffusivity, surface tension.

Table 2 Relationship between bubble emission frequency and bubble departure diameter

Reference	Correlation
Jacob and Fritz[42]	$fD_d = 0.078$
Zuber [43]	$fD_d = 0.59\left[\frac{\sigma g(\rho_l - \rho_v)}{\rho_l^2}\right]^{\frac{1}{4}}$
Peebles and Garber[44]	$fD_d = 1.18(\frac{t_G}{t_w + t_G})(\frac{\sigma g(\rho_l - \rho_v)}{\rho_l^2})^{\frac{1}{4}}$
Cole[45]	$fD_d^{\frac{1}{2}} = 0.59\left[\frac{4g(\rho_l - \rho_v)}{3C_d\rho_l}\right]^{\frac{1}{2}}$
Ivey[46]	For dynamically controlled growth: $fD_d^{\frac{1}{2}} = constant$ For thermally controlled growth: $fD_d^2 = constant$
Kim et al.[47]	$fD_d^{4.85} = 7.2 \times 10^{-8}$
Mikic and Rohsenow[48]	$f^{\frac{1}{2}}D_d = \frac{4}{\pi}Ja(3\pi\alpha_1)^{\frac{1}{2}}\{(\frac{t_G}{t_w + t_G})^{\frac{1}{2}} + \left(1 + \frac{t_G}{t_w + t_G}\right)^{\frac{1}{2}} - 1\}$ For $0.15 < \frac{t_G}{t_w + t_G} < 0.8$ $D_d^2 = 0.6889Ja^2\pi\alpha_l$

Some researchers [23,26,49] found that the bubble growth duration increases with a reduction in wettability. This could be attributed to surface tension acting

parallel to the surface at the triple contact line. It is well known that surface tension increases with the reduction of wettability and surface tension prevents the bubble detaching from the heated surface during the bubble growth period. Therefore, the duration of bubble growth is prolonged. Also, the bubble generated on a lower wettability surface has a larger initial base and bubble departure diameter based on Fritz's correlation, causing longer time to be required to reduce the base and increase vapour volume for bubble departure. On the contrary, the waiting duration increases with wettability. There are two possible reasons. Firstly, as mentioned previously, after bubble departs the nucleate site undergoes a recovering process until the temperature exceeds the required value for next nucleation. Equation (6) derived by Griffith and Wallis[50] indicates that the minimum superheat ΔT required to initiate nucleation is inversely proportional to the embryonic bubble diameter.

$$\Delta T = \frac{2\sigma T_s (v_g - v_l)}{\Delta \mathrm{H}_{\mathrm{vap}} r_c} \tag{6}$$

where it σ is surface tension, $\Delta \mathrm{H}_{\mathrm{vap}}$ is the latent heat of vaporisation, and v_g and v_l are the specific volume for air and liquid. It is found from the equation that a bubble with a larger diameter needs a lower wall superheat to grow. Also, embryonic bubble diameter increases with a decrease in wettability. Consequently, it can be inferred that high wettability surface results in prolonged waiting duration.

Table 3 summarises bubble emission frequency, growth time and waiting time under various contact angle. Suroto, Jo[16] and Nam[51] observed a continuous bubble growth on the hydrophobic surface. After a bubble departs, one part of the bubble still remains on the surface and works as a nucleus for the next bubble. This means that there is no waiting time for this hydrophobic region. Totally, there is a divergence about the sum growth duration waiting duration. Majority of studies [14,17,49] show a surface with higher contact angle has lower bubble emission frequency whilst Jo got a reversed result. Based on the study from Jo, it should be noted here that the surface resistance on the micro-post structure could restrict bubble diameter, leading to high bubble emission frequency although the contact angle for the whole surface is up to 143˚. Moreover, wall superheat needs to be kept constant to compare the frequency at different wettability because it has a significant impact on bubble emission, especially for waiting duration which could change much more rapidly than growth duration.

Nonetheless, all of them agreed the general tendency of the bubble release frequency equation derived by Zuber:

$$fD_d = 0.59\left[\frac{\sigma g(\rho_l - \rho_v)}{\rho_l^2}\right]^{1/4} \tag{7}$$

In this equation, all the liquid and vapour properties remain constant under the same input heat flux condition. As a consequence of reduced departure diameter due to change surface wettability, the nucleate site has higher bubble emission frequency. In a future study, factors such as wall superheat, surface topography and roughness should be studied separately to deeply investigate the effect of wettability on bubble emission frequency.

Table 3 Summary of bubble emission frequency under different surface contact angle

	Contact angle	Input heat flux/superheat	Diameter	Bubble growth duration	Waiting duration	Frequency
Teflon coated wafer[51]	120°	ΔT_w: 2.9 ^oC	6.7mm	1.68s	0s	0.6 Hz
Silicon wafer[51]	30 °	ΔT_w: 4 ^oC	2.3mm	19.2 ms	0.8ms	50 Hz
Silicon wafer[16]	54 °	ΔT_w: 12.4 ^oC		10.5ms	0	95 Hz
Teflon hydrophobic surface[16]	123 °	ΔT_w: 4 ^oC		397ms	0	0.003 Hz
Aluminium-oxide [27]	13 °		3.2mm	14 ms	11ms	39.2Hz
Silicon [27]	57 °		3.6mm	43.3ms	0.5ms	22.8Hz
Teflon [27]	108 °		6.8mm	1.942s	0ms	0.5 Hz
Indium-Tin_oxide [52]	80 °	ΔT_w: 9. 4 ^oC	2.8 mm	10 ms	70 ms	12.5 Hz
Stainless steel with SiO_x deposition [53]	22 °	220 kW/m^2	1.7 mm	5 ms	28 ms	50 Hz
Stainless steel with TiO_2 deposition [53]	31 °		1.45 mm	2.5 ms	17 ms	130 Hz
Stainless steel with Pt deposition [53]	67 °		1.3 mm	2.3 ms	16 ms	160 Hz
Fe_2O_3 deposition	80 °		1 mm	2.2 ms	10 ms	210 Hz
Stainless steel [53]	85 °		0.8 mm	2.1 ms	8 ms	300 Hz
Silicon wafer [54]	44 °	ΔT_w: 4 ^oC	2.3 mm	15 ms	Not specified	52.6 Hz
Copper with CuO nanostructure[54]	7.5 °	ΔT_w: 5. 3 ^oC	1 mm	5.2 ms	0.34 ms	187 Hz

SAM: self-assembled monolayers

2.1.3 Microlayer

Nucleate boiling heat transfer can be improved by enhanced bubble surface area during growth and departure. The growing vapour bubble interacts significantly with wick structure when the pore length scale of wick structure is much smaller than the bubble departure diameter. This interaction leads to an increase in phase change heat transfer rate because more thin liquid films between the solid surface and vapour occur [10]. This thin liquid film area is called a microlayer. It is defined as the interface where its slope increases from 0 at the dry patch region to the macroscopic contact angle θ at the macro-region [55]. In the dry patch region, the heat transfer is poor due to the high thermal resistance of a vapour. Furthermore, the strong intermolecular force prevents its evaporation. The heat transfer in the macro-region can be regarded as single phase flow. The thermal resistance from wall to liquid-vapour interface is higher with the increase in film thickness, causing lower superheat in this area[56]. In the microlayer, the mirror influences of intermolecular and low heat resistance make strong evaporation due to its curvature and thickness. Zhang[57]found that the process of liquid evaporation absorbs about 40% of heat flux from the heated wall and Sebastian as shown in Figure 2 [58], therefore it is most effective heat transfer area compared against a single phase heat transfer area such as macro-region regime and dry patch regime. Cooper and Lloyd[59] conducted the thickness expressed as

$$l = 0.8\sqrt{v_l t} \tag{8}$$

where v_l is liquid velocity normal to the vapour-liquid interface. But this estimation doesn't consider the effect of wettability. Utaka at al. [60] used laser extinction technology to investigate microlayer thickness in nucleate boiling

process. They found that the initial microlayer thickness increases linearly from the site of bubble incipience when bubble is still in a semi-spherical shape, and then the shape of the bubble changes to the spherical segment geometry meanwhile microlayer thickness reduces due to the evaporation process. From Figure 3, it can be seen that there is no liquid micro layer underneath the bubbles for a hydrophobic surface while the liquid film area increases with lower contact angle for a hydrophilic surface. In addition, a bubble with a large contact angle hysteresis also can enhance this thin liquid film area. Although the thin liquid film caused by the interaction between bubble and wick benefits heat transfer during a boiling, this interaction can result in added drag and significantly delay the departure of bubbles[10]. Therefore, there is a trade-off between time averaged and transient boiling heat transfer coefficient under different conditions of bubble characteristics.

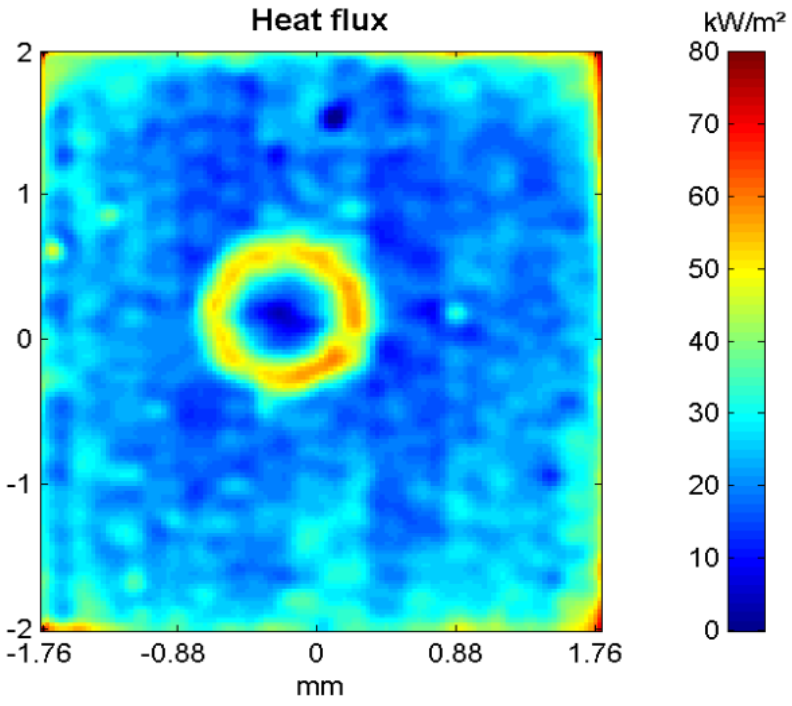

Figure 2 Heat flux distribution during bubble growth[58]

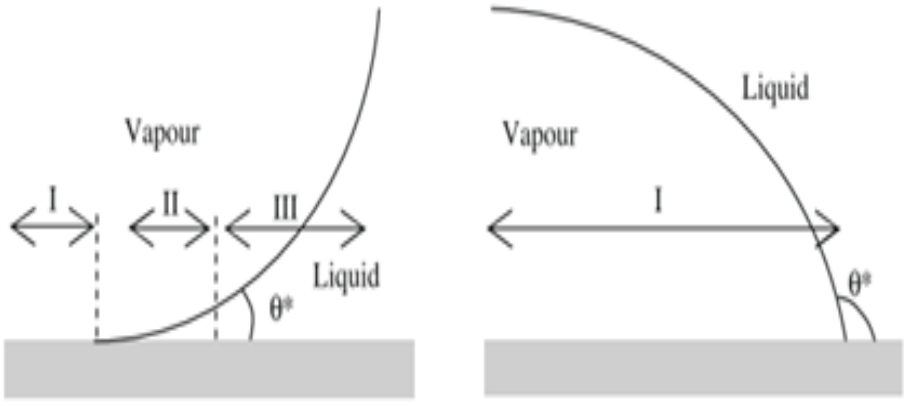

(a) (b)

Figure 3 Heat transfer mechanisms on (a) hydrophilic and (b) hydrophobic surfaces

2.1.4 Active nucleate sites density

The active nucleate site on a heated surface is a significant parameter to predict heat transfer and account for heat absorbed away by the bubble departing from the heated wall in a nucleate boiling system. In general, active nucleate site density is dependent on several parameters such as wall superheat, distribution of cavities on wall surfaces, bubble contact diameter, wettability, as well as other properties for both the wall and liquid[61].

Wettability modification is suggested to enhance boiling heat transfer by the increased availability of active nucleate sites. Wang and Dhir [62] might be the first to perform a systematic study of the effect of contact angle on the density of active nucleation sites. They have conducted boiling experiments about copper heaters oxidised at different degrees to change the contact angle. It was found that active nucleation site density strongly depends on wettability and the

density of active nucleate sites increases with the contact angle. They correlated density of active nucleate site N_a with contact angle $\emptyset$ and diameter of cavity mouth D_c as:

$$N_a = 5 \times 10^5 (1 - \cos \emptyset) D_c^{-6} \; for \; \emptyset < 90^o \tag{9}$$

The diameter of cavity mouth D_c depends on wall superheat ΔT_w as shown in equation (6). It was found that nucleate site is not only related to surface wettability but also affected by wall superheat. Betz [18]analysed the effects of wettability and wall superheat on the density of active nucleate site through a nucleate boiling experiment. They observed that it is more difficult to measure nucleate sites on a hydrophobic surface at a high wall superheat because many bubbles nucleate and then quickly merge, leading to a single bubble departing from the respective surface. Therefore, they counted the number of nucleating bubbles immediately after bubble departure. It was found from Figure 4 that the hydrophobic surface offers more nucleate sites than the hydrophilic surface at low wall superheat. Also, the hydrophobic surface starts to nucleate prior to the hydrophilic surface while stops nucleating at a lower superheat due to low critical heat flux.

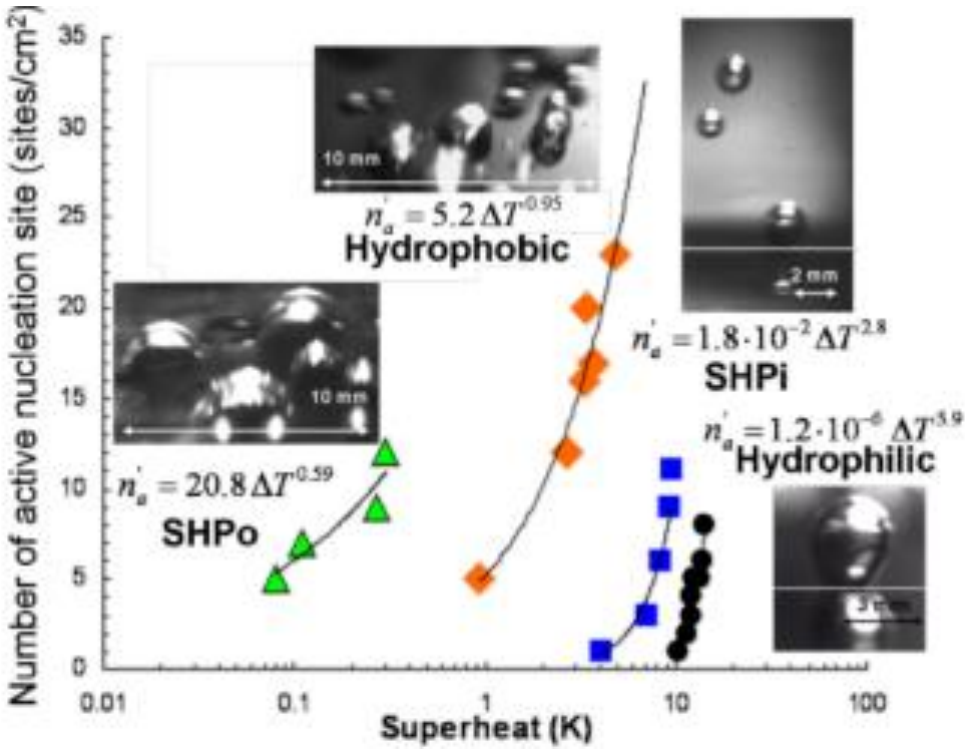

Figure 4 Density of active nucleate sites [18]

2.1.5 Critical heat flux

Nucleate boiling is bounded at high heat fluxes by something called the critical heat flux (CHF) limit because a continuous vapour layer with lower thermal conductivity occurs on the boiling surface, which leads to a sudden, large reduction in heat transfer coefficient. The occurrence of CHF causes the surface suffer from dry-out and the surface can be damaged due to a rapid increase of the surface temperature. Therefore, it is important to control and increase the CHF value within a reasonable range. Researchers have focused on the surface modification which can delay delaying the critical heat flux, such as microporous coating, nanorods, micropillars etc. Wettability is a key parameter affecting the bubble wall interaction, bubble growth, and bubble departure. Many experiments and models related to the effects of wettability on critical heat flux were performed. Garetner [63] coated a heater surface with a non-

wetting film of grease and concluded non-wetting film results in a large reduction in CHF. Chen et al. [64] fabricated a superhydrophilic surface made by nanowire arrays on a Cu substrate and found this heated surface can lead to more than 100% increase in CHF. O`Hanley et al [28]conducted an experiment to investigate the effects of porous surfaces with different wettability on CHF. Results showed that the porous hydrophilic surface increased CHF by 50-60%, whilst the porous hydrophobic surface led to a reduction of CHF by 97%. Kandlikar[65] was one of few researchers to include the effect of wettability on critical heat flux in correlation as expressed by:

$$q_{CHF} = \left[\frac{1+cos\beta_r}{16}\right]\left[\frac{2}{\pi}+\frac{\pi}{4}(1+cos\beta_r)cos\varphi\right]^{\frac{1}{2}}[\rho_g^{\frac{1}{2}}h_{fg}[\sigma g(\rho_f-\rho)^{\frac{1}{2}} \quad (10)$$

where β represents a dynamic receding contact angle. The equation implied that high surface wettability enhances critical heat flux. To be detailed, the hydrophilic surface delays CHF since the ability of rewetting of nucleation site after bubble departure is high. On the contrary, hydrophobicity surfaces with low wettability repelled water from the nucleation sites, resulting in bubble coalescence and causing it to be more difficult to depart from the surface. Besides, bubbles on a lower wettability heated surface require less energy to form than on higher wettability surface. Therefore, the vapour film formed by the coalescence has a small thermal conductivity, which leads to a large reduction in CHF.

2.1.6 Heat transfer coefficient

In the nucleate boiling process, there are three ways about heat transferred from the heating surface to a fluid: evaporation around bubble-liquid interfaces,

transient conduction, and micro-convection generated by nucleation, growth, and departure of bubbles[66]. Evaporation is the most efficient heat transfer model. The thermodynamic efficiency of nucleate boiling is evaluated by the heat transfer coefficient (HTC) which is the ratio of the imposed heat flux (q) to the temperature difference between the heated wall (T_w) and saturated fluid temperature (T_s). It is expressed as

$$h = \frac{q}{T_w - T_s} \tag{11}$$

Heat transfer coefficient for nucleate boiling is affected by many factors such as bubble diameter, emission frequency, the density of the nucleate site, liquid thermal conductivity, and liquid latent heat and so on. This is in agreement with many investigations[23] [29] [49] [18], which reported that hydrophobic surface has a larger heat transfer coefficient at low superheat while the hydrophilic surface provides a higher heat transfer coefficient under high superheat conditions because the majority of nucleation and boiling occur on the hydrophobic surface prior to hydrophilic surface. However, Betz[29] mentions that although hydrophobic surface has better performance at low superheat, the heat transfer coefficient remains constant with the an increase in superheat as large vapour film contact area restricts the density of active nucleate sites and bubble departure is a problem for low wettability surfaces. Based on his experimental results, the surface with a static contact angle of 165 ^{o} keeps the heat transfer coefficient of 13kW/m^{2}K constant and the surface with the static contact angle of 0^o increases from 0 kW/m^{2}K to 28 kW/m^{2}K when superheat increases from 0 ^{o}C. Figure 52 summarises the heat transfer coefficient and critical heat flux at different wettability. A general conclusion could be drawn

that high wettability enhances heat transfer coefficient and delays critical heat flux.

Table 4 Summary of heat transfer coefficient and critical heat flux

Pattern	Fabrication	Dimension	Liquid	heat flux/superheat	Contact static angle	CHF (kW/m^2)	HTC
Rough porous Hydrophilic Indium Tin Oxide surface [28]	Layer by layer deposition of 50nm diameter SiO2 particles, fifty layers	50.8mm×5 0.8mm	water	From 0 to CHF	<5°	1591 kW/m^2	Not specified
Rough Porous Hydrophobic Indium Tin Oxide surface[28]	Layer by layer deposition of 50nm diameter SiO2particles, fifty layers chemical vapour deposition of fluorosilane	50.8mm×5 0.8mm	water	From 0 to CHF	140°	20-40 kW/m^2	Not specified
Smooth hydrophilic [28]	SiO_2 deposition	50.8mm×5 0.8mm	water	From 0 to CHF	<5°	1009 kW/m^2	
Smooth hydrophobic [28]	Chemical vapour deposition of fluorosilane	50.8mm×5 0.8mm	water	From 0 to CHF	112°	968 kW/m^2	
Stainless steel with nanoparticle deposition[23]	SiO_x deposition	100mm×5 mm	water	From 0 to 300 kW/ m^2	22°	Not specified	13kW/m^2 K
Stainless steel with nanoparticle deposition[23]	TiO_2 deposition	100mm×5 mm	water	From 0 to 300 kW/ m^2	31°	Not specified	11.5kW/ m^2K
Stainless steel with nanoparticle deposition [23]	Pt deposition	100mm×5 mm	water	From 0 to 300 kW/ m^2	67°	Not specified	10.5kW/ m^2K
Aluminium Oxide[49]	Deposited in a thin layer of 100 nm thickness by RF sputtering	10mm×10 mm	water	From 0 to CHF	13°	1250 kW/m^2	36kW/ m^2K
Plain Silicon[49]	Uncoating	10mm×10 mm	water	From 0 to CHF	55°	720 kW/m^2	20 kW/ m^2K
Teflon[49]	Teflon solution was spin-coated on the silicon substrate	10mm×10 mm	water	From 0 to CHF	108°	130 kW/m^2	4kW/m^2 K
Silicon superhydrophilic surface[18]	Oxidised silicon surface	10mm×10 mm	water	Up to 10K superheat	0°	Not specified	28kW/m^2 K
Silicon superhydrophobic surface[18]	Random nanostructuring, microlithography and fluoropolymer-coated	10mm×10 mm	water	10K superheat	150-165°	Not specified	13kW/m^2 K

2.2 State of art of IGBT thermal management

2.2.1 Future trends and challenges for IGBT module in automotive applications

From the viewpoint of protecting the global environment, the reduction of carbon dioxide emissions has been required. In the automotive field, hybrid electric vehicles and electric vehicles tend to have lower carbon dioxide emissions. Figure 5 illustrates the main components of a hybrid electric vehicle and the location of invertor [67]. The IGBT in the inverter is used to switch with high speed for satisfying the frequency requirement.

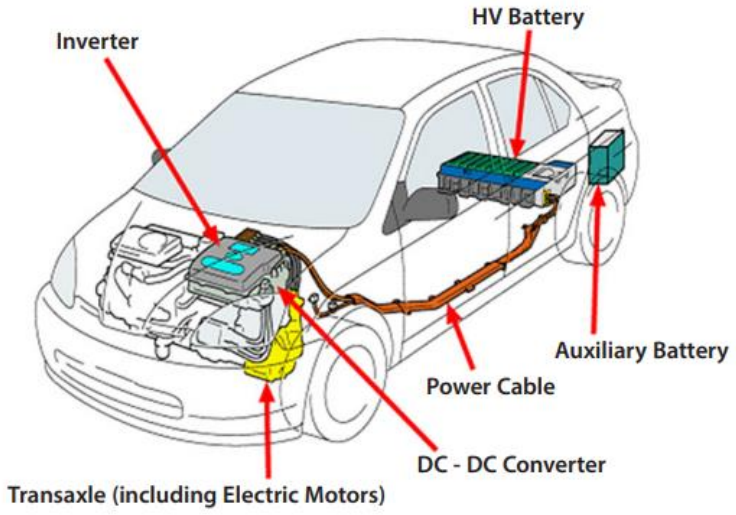

Figure 5 Main components and the location of invertor in a hybrid electric vehicle [67]

Table 5 summarises thermal challenges for IGBT modules. Currently, the IGBT modules are required to be compact and highly integrated due to limited space in the automobile, therefore the IGBT power module will inevitably dissipate more heat. In hybrid electric vehicles, the heat flux of IGBT module will increase from 100-150 W/cm^2 to 500 W/cm^2or even higher in next generation [68-71]. Mertens et al.[72]calculated the heat flux of a typical IGBT in term of

switch frequency at different duty cycles with careful consideration of the turn-on and turn-off curves as shown in Figure 6. Higher switching frequencies and duty cycles will result in a greater loss. Currently, the commonly used IGBT switching frequency ranged between 20 and 50 kHz[73].

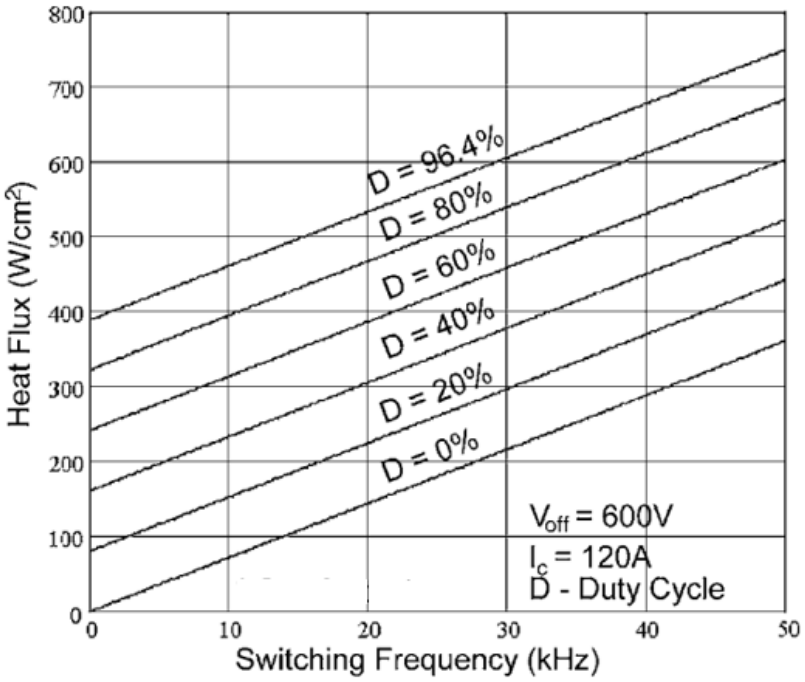

Figure 6 Heat flux versus switching frequency for different duty cycles [72]

(V_{off}=600V, I_c=120A)

The heat flux originates from power loss due to voltage drop and the current flowing through the device simultaneously. Power loss mainly consists of conduction loss and switch loss, resulting in the junction temperature rise. Currently, with consideration of structure components, solder materials, reliability and cost, the temperature of the entire IGBT module is required to be below the maximum junction temperature of 150 ℃ or 175 ℃[74-76]. Sheng et al.[77] reviewed IGBT modules published in the literature with analyses of the different circuit conditions, structures and thermal considerations which are the

basis for thermal management. Mohammed et al.[78]gave a review on the power electronic applications for power systems and indicated that silicon carbide is a promising choice for high power, high temperature and high-frequency applications due to its high electric breakdown property, high carrier drift velocity and high thermal conductivity. Table 5[79] summarizes the power electronics trends and their effects in automotive area. It can be found that the heat dissipation density will inevitably increase and operation conditions become increasingly harsh.

Table 5 Thermal challenges for power semiconductors

Trend	Effects
Placement under bonnet or on-engine.	Increasing ambient operating temperatures
Highly integrated components	Higher power losses
Increasing voltage and current capability	Higher power losses
Electrically isolated baseplate	More difficult to cool power devices
Increasing switching speeds Miniaturisation	Higher heat fluxes Higher heat dissipation density

2.2.2 Failure mechanisms

The lifetime of the IGBT modules is determined by the failure mechanism related to thermal stress. Thus, to predict the lifetime, it is important to investigate the failure mechanism of the IGBT modules. The thermal stress generates when the IGBT module operates, therefore the bonded surfaces, solder layer, and wire bonding are continually affected. In the IGBT modules, solder joint cracking, delamination of DBC, heel cracks and bonding wire lift-off are the main failure modes. These failures are exacerbated by power cycling. As the failures rise, the thermal deformation and cracks result in less area available for heat transfer, leading to an increase in the thermal resistance of the module. Then the high operating temperature results in power cycles of large amplitude, causing high thermo-mechanical stresses and crack growth rates, and eventually leading to the module failure of the IGBT by overheating [80]. Qian et al. [79] summarised the potential failures of the IGBT power module as shown in Table 6. Fatigue is the most reported failure resulting from overheating. Therefore, it is urgent to improve the thermal management to achieve long term reliability.

Table 6 Potential failures of IGBT power module

Failure sites	Causes	Stresses	Modes	Mechanisms
Bond pad	High temperature	Thermal overstress	Open circuit	Metallisation reconstruction
Bonding wire	CTE mismatch, high temperature	Thermomechanical stress	Bond wire lift off, heel crack	Fatigue
Solder joint	CTE mismatch, transformation in solder microstructure at high temperature	Thermomechanical stress	Solder joint cracks	Fatigue or grain growth
Ceramic substrate	Thermal shock	Thermomechanical stress	delamination	Delamination of metallisation

The solder layer is used for joining the chip and DCB layer, and the DCB layer and substrate. Melting temperatures of solders are low and the deformation of solder is highly dependent on the temperature and strain rate[81]. With increases in temperature and thermal stress, delamination and cracking of the solder will be promoted, leading to thermal resistance increase and junction temperature growth, and therefore accelerating failure.

When the IGBT module is operates under high current ratings and switching operation, wire-bondings suffer from almost the full temperature swings imposed by both heat dissipation in the silicon and the wire itself. Generally, the

wire bonding failure takes place predominantly as a result of fatigue resulting from shear stresses generated between the bond pad and the wire bonding. Eventually, the wires gradually lift off or suffer from heel crack propagation until they reach the open circuit condition.

Thermal fatigue life of the DCB substrate depends on the growth of a fatigue crack in copper from a geometric singularity and close to the interface between upper copper and ceramic layer. The crack bifurcates and breaks the ceramic layer when it reaches critical condition.

2.2.3 Significant of thermal management

Under normal working conditions, IGBT power modules suffer severe stresses which lead to thermo-mechanical fatigue and finally induce failure mechanisms. The mismatch in coefficient of thermal expansion and the temperature gradients within material layers are responsible for the stresses experienced by the IGBT power module[82].

Currently, IGBT module tends to dissipate more heat due to increasing functionality and reducing die feature size allowing more processing to be packed into a smaller volume. With an increase in heat flux, IGBT modules are observed to suffer many thermal reliability problems such as performance degradation, module deformation, and even permanent damage. Furthermore, IGBT modules operate under harsh conditions such as high temperature and frequent thermal cycles. This will induce repetitive stress which results in fatigue and failures, particularly at solder layer and bonded wires. Based on data courtesy of the US Air Force shown in Figure 7 [83], temperature is the most important factor for all electronic failure, which accounts for 55%. In addition,

the IGBT open circuit failure and bond wires lifting off can be caused by vibration.

Thermal management systems become a major technical barrier in developing advanced IGBT modules. High-performance cooling strategies of the IGBT module can not only enhance reliability by decreasing overstress and the severity of fatigue mechanisms, but also improve the operational performance of the system. The thermal management systems should ensure that low temperature gradient is distributed on the chip and the local chip temperature does not exceed the designed junction temperatures such as 125 ℃, 150 ℃ and 175 ℃, otherwise the module operational performance and reliability are affected.

Due to the importance of thermal management, the market for thermal management technology in consumer products is rising faster than the production of consumer products. Research and Markets [82, 84] reported that the global market for thermal management products will rise from $10.7 billion in 2015 to nearly $11.2 billion in 2016 and $14.7 billion by 2021.

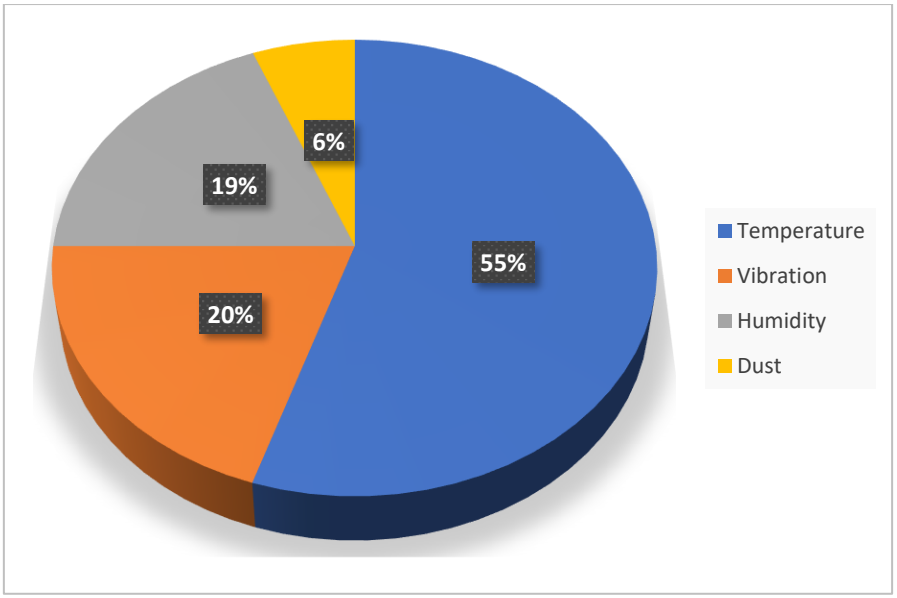

Figure 7 Environmental causes of failure in defence-related electronic systems based on a survey conducted by US Air Force[83]

2.2.4 Research area for thermal management system

The main technical challenge for thermal management of automobiles is to develop a system with the high cooling capacity and reliable operation for dissipating a large amount of heat in a compact space under harsh environmental conditions. In addition, it is desired to minimise the overall system cost, complexity, and size. Table 7 summarises the research area for thermal management systems [85].

Table 7 Research area for thermal management system

Research areas	Research solutions
Integration of thermal management system	• Identify thermal requirements • Evaluate each thermal solution • Combine cooling method with electrical power module
Cooling methods with high cool capacity and low cost	• Modelling and experimental characterisation of the thermal performance of the integrated module
Thermal stress and reliability of thermal management and power component	• Develop predictive thermal stress and reliability models • Guide research decisions and identify the potential barriers

2.2.5 Current thermal management systems

The typical thermal path can be simply described as follows:

1. Heat dissipated by the power module.

2. The heat is conducted to the cooler through several layers of the power module.

3. The heat is then transferred by convection to the coolant fluid

Currently, there are a number of methods to cool power electronics in different applications. Large variation exists in complexity, cost, cooling capacity, weight, life span, reliability of each cooling method. Table 8 shows thermal performance for various cooling methods and their typical range of heat transfer coefficients

[1]. The convective heat transfer coefficient depends on physical properties of fluid and physical situations such as contact surface geometry, the properties of walls, bulk fluid velocity, and nature of fluid motion. The high heat transfer coefficients of boiling heat transfer range from 2,500 W/m^2K to 100,000 W/m^2K. Boiling heat transfer dissipates large amounts of heat from heat source by using the transport of latent heat with a phase change, which is suitable for electronics devices with high heat dissipation rate.

Table 8 Cooling solutions and their heat transfer coefficient [1]

Cooling solution	Heat transfer coefficient $[W/m^2K]$
Natural convection by air	2-25
Forced convection by air	25-250
Natural convection by water	50-1000
Forced convection by water	100-20,000
Phase change by boiling	2,500-100,000

Table 9 summarises current cooling methods used in IGBT power modules and Table 10 evaluates each current cooling solutions. Single-phase cooling technologies including air, water-glycol, etc. are the most-used in thermal management of IGBT modules. With increasing heat dissipation, however, it is predicted that conventional air cooling solutions struggle to meet cooling demand, especially when the power dissipation exceeds 1500 W [86]. Micro- and mini-channel liquid cooling solutions were focused on over the past decade. They have a major advantage is the simplicity of heat sink design due to compactness and lightweight. They can also offer a higher cooling capacity (typically 120 W/cm^2) in comparison with that of air cooling (typically 50

W/cm^2) [71]. Yin et al. [87] designed a rectangular microchannel heat sink fabricated directly in the AlN-layer of the substrate. The simulation results show the thermal resistance of the proposed structure is 0.128 ˚C/W at a pressure drop of 66.6 kPa, which was reduced by 80% compared with the conventional structure. Stevanovic et al. [88] developed an integral microchannel heat sink for power electronics. Arrays of sub-millimetre channels were directly fabricated onto the backside of the substrate. The junction to fluid thermal resistance for IGBTs was 0.17 ˚C/W. Vafai et al.[89] proposed a numerical model to analyse two-layered micro-channel heat sinks with respect to thermal performance and pressure drop. It is found that the streamwise temperature rise on the base surface and pressure drop were both reduced compared with one layered heat sink. Naqiuddin et al. [90] reviewed micro-channel design for high heat flux application such as solar cells, fuel cells, heat exchangers, and medical systems. However, the low temperature uniformity caused by flow redistribution, channel clogging erosion, and low term reliability is still needed to be carefully considered. In particular, the heat transfer coefficient of the micro channels strongly depends on the size of the channel and fluid flow rate. However, the pumping power inevitably increases with the heat transfer rate. In order to decrease the working load of the pump, jet impingement becomes an attractive cooling method. It is able to generate a high flow rate of fluid with lower pumping power and yield high local heat transfer rate. Jörg et al. [91] developed a direct single impinging jet for cooling of a MOSFET power electronic module. The heat transfer rate could be as high as up to 12,000 W/m^2°C. Nonetheless, the temperature distribution of the cooled surface is non-uniform because cooling performance rapidly degrades when it is away from the centre of the jet

region[92]. In order to improve temperature uniformity, array impingement cooling was paid more attention. Bhunia[92] carried an experiment about an array impingement cooling system with 441 nozzles, each with a diameter of 200 μm. Results indicated that the average heat transfer coefficient doesn't largely reduce and it is capable of cooling an area from a few cm^2 areas, to a few hundred cm^2 area. Gould et al. [93] compared the thermal performance of cold plat cooling, microchannel cooling, and the array jet impingement cooling when they were used to cool silicon carbide power conversion modules for vehicle application. The jet impingement cooling reduces junction-to-coolant thermal resistance by 2.8 and 1.7 times compared to a cooling plate and microchannel cooler system. In general, for single-phase and phase-change impingement, the heat flux of 250 W/cm^2 and 1,000 W/cm^2 can be dissipated with using water as the working fluid, respectively [94-96]. Although jet impingement can achieve a very high heat transfer coefficient, the applicability of this strategy is limited by problems of high cost, complex cooling flow redistribution, cooling loop leakage, and channel blockage. Therefore, a cost-saving but more a reliable thermal management device is required purposes. Phase-change cooling strategies become more attractive for with higher thermal demands.

Table 9 Summary of current thermal management system

Authors	Type	Cooling solution	Dissipating heat	Heat flux on IGBT chip	Flow rate	Heat transfer coefficient	Peak T	Heat sink size
Dupont [97]	600V 200A	Forced air-cooling extruded aluminium heat sink	600W			1.4 kW/m^2˚C		122mm× 60mm
Howes[98]	1700V 450A	Air-cooled extruded aluminium heat sink	600W		150 cfm	1.4 kW/m^2˚C	120˚C	122 mm × 62 mm
Howes[98]	1700V4 50A	Water-cooled aluminium cold plate (bonded copper D shape tubing	1070W		7.5 l/min	3.5 kW/m^2˚C	120˚C	122 mm × 62 mm
Howes[98]	1700V4 50A	Cold plate cooling R-134A dielectric liquid	1461W		1.51 l/min	16.5 kW/m^2˚C	120˚C	122 mm × 62 mm
Lee [99]	600V 600A	Integrated liquid cooled	1200W	111 W/cm^2		6 kW/m^2˚C		98 mm × 51 mm
Bostanci [100]		Two-Phase Spray Cooling FC-72 dielectric liquid	700W	400 W/cm^2	0.15 l/min	280 kW/m^2˚C	125˚C	10 mm× 20 mm
Semikron [101]	450V 400A	Single-phase liquid-cooled base plate with pin-fin		64 W/cm^2	20.1 l/min	17.3 kW/m^2˚C	125˚C	
Wang[71]	Toyota Prius IGBT	R134a- cooled two phase cold plate	2400W	120 W/cm^2	8.3 l/min	29 kW/m^2˚C	68.3˚C	81.3 mm ×216.4 mm
Giliot[102]	1600V 50A	Double side cooling	1200W			75 kW/m^2˚C		40 mm × 29 mm
Stevanovic [88]	1200V 200A	Micro-channel Liquid Cooling	500W	470 W/cm^2	3 l/min	60 kW/m^2˚C		26.9 mm ×25mm
Bhunia[69]	1200V 150A	Direct Single Impinging Jet Cooling	1170W		0.7l/min	10.2 kW/m^2˚C		122 mm× 62 mm
Turek[103]	450V 400A	Evaporative Spray cooling	1545W	140 W/cm^2	3.7 l/min	61 kW/m^2˚C	125˚C	

Table 10 Evaluation of various thermal management system

Method	Pros	Cons
Forced Air Cooling System	• Low-cost heat sinks and fans. • Large supplier base and range of options. • Air can cool other components such as bus bars, electronic circuits. • Low maintenance. • Very broad design knowledge base.	• Not very efficient for heat transfer. • The large volume of air requires ducting which can impose constraints on mechanical layout and design. • Space inefficient. • Acoustical noise. • Performance is affected by altitude
Water-based Cooling System	• Water is readily available. • Choice of liquid cold plate suppliers with different price/performance ratios. • Small size and low weight of cold plates. • The heat exchanger can be placed remote to a heat source.	• Fluid leaks can cause serious damage and failure of equipment. • Water can be corrosive and has the potential for biological contamination. • High flow rates require large pumps, power supply, pipe diameters and reservoir. • Protection required as a pressurised system. • If operated in series there is thermal stacking. • Potential for condensation. • Ethylene glycol is not environmentally friendly.
Double side cooling	• Compact system • Increased current carrying capability/chip area • Lower thermal resistance	• High cost • Redesign IGBT structure if double-side cooling applied • Adding one DCB layer

	• Tolerating higher cooling liquid temperature than that of one side cooling • Low thermal impedance • Enables multi-dimensional heat transfer	
Vapour chamber	• Excellent thermal conductivity • Low thermal resistance • Suitable for multiple heat source • Spreading heat evenly and contributing to eliminate hot spots across the IGBT module • Reliable thermal device due to without moving parts or any corrosive material. • High integration since it enables to directly bond to the electronics module • Overcoming gravity and working in any orientation because of capillary force • Ideal for high heat flux application ranged from 60 W/cm^2 to 750 W/cm^2 • Freeze/thaw tolerant • Not affected by thermal cycling	• Higher initial cost than air-cooled or water-cooled methods • Requiring careful design to avoid dry out. Vapour chamber no longer function properly if dry out occurring. • Integrated with heat sinks or either copper or aluminium material.
Jet impingement cooling	• High cooling capacity • Efficient	• Only practical in a stable and stationary environment

	• Less design tolerances on nozzles than spray cooling • Quickly heat removal	• Large space and equipment required • Coolant fluid filtration required • Heavier system due to much higher working fluid required than that in spray cooling
Spray cooling with the change of phase	• High heat transfer coefficients • Faster heat transfer • Less working fluid required compared to force convection bulk flow and jet impingement cooling • Temperature uniformity	• Only practical in a stable and stationary environment • High technical complexity • Significant reduction of thermal performance if applied for non-uniform heat sources • Large space and equipment required • Corrosion and long term-term wear of nozzles • Erosion of the surface • High-pressure pumping required • High cost • High maintenance

2.3 Summary

In this chapter, nucleate pool boiling and thermal management of IGBT power module are reviewed. Until now, effects of wettability on performance of heterogeneous nucleate boiling are not fully resolved and there is still no identity agreement on many related aspects due to lack large amounts of experimental data. Based on the results from majority researches, high wettability surface enhances nucleate boiling due to larger liquid microlayer underneath bubble, quicker bubble departure, high critical heat flux. However, the surface with low wettability also could enhance boiling performance. Although the vapour films

generate on low wettability surface earlier, leading to a rapidly reduction in heat transfer coefficient, and much longer bubble emission duration, it has advantages of phase change occurs prior to high wettability surface and much more active nucleate sites.

The heat dissipation rate of IGBT power modules increase rapidly due to high power rating and reduced the package size, leading to a high requirement for thermal management systems. The current single-phase cooling solutions including air and liquid convection cooling become difficult to achieve high heat dissipation rate and uniform temperature distribution. Thus, more attention is focused on phase change cooling solution due to its high heat transfer rate and temperature uniformity. In the following study, it is aimed to investigate the effect of surface wettability on pool-boiling phase change heat transfer and enhance pool boiling heat transfer by control bubble dynamics. Furthermore, it also aims to integrate IGBT power module with phase change heat transfer process to increase cooling capacity and improve the temperature uniformity.

3. Enhanced pool boiling heat transfer on nanoparticles-coated heterogeneous wetting micro-channel surfaces

In this study, it aimed to investigate of the nucleate pool boiling heat transfer with an accurately controlled microstructure and heterogeneous wetting pattern to gain insights into heterogeneity on boiling process. Silica-PDMS and Fe_3O_4 nanoparticles are used to produce homogeneous and heterogeneous wetting surfaces. Heterogeneous wetting surface induces synergistic effects. Hydrophilic and hydrophobic nanoparticles are separately deposited onto the inside of micro channel and the top of channel surface to promote bubble generation and departure. High-speed camera is used to record bubble dynamics on different surfaces. In addition, four heterogeneous surfaces with various widths of channel were prepared to investigate the channel size effect on boiling heat transfer.

3.1 Research Methodology

In this section, the pool boiling setup and surface preparation methods are presented. Firstly, a description of the experimental test rig is given, and the basic measurement methods are described. And then the surface coating methods are explained in detail. Finally, surface characteristics are measured and analysed.

3.1.1 Experiment setup for pool boiling

The pool boiling vessel is a 360 mm×304 mm×220 mm stainless-steel tank shown in Figure 79 in appendix. Two glass windows are fixed in place by stainless steel covers and screws and are sealed with PTFE gasket. They are equipped with the vessel to allow observation of heated surface.

The bottom part of the vessel contains a hole with diameter of 100mm. A thermal insulation block made with PEEK (polyether ether ketone) insulation with low thermal conductivity of 0.25 W/mK is inserted into it to reduce heat loss shown in Figure 8. Several O-ring grooves are designed on the bottom of the PEEK cylinder to prevent liquid leakage. A bottom flange is bolted with the pool boiling vessel and the PEEK cylinder.

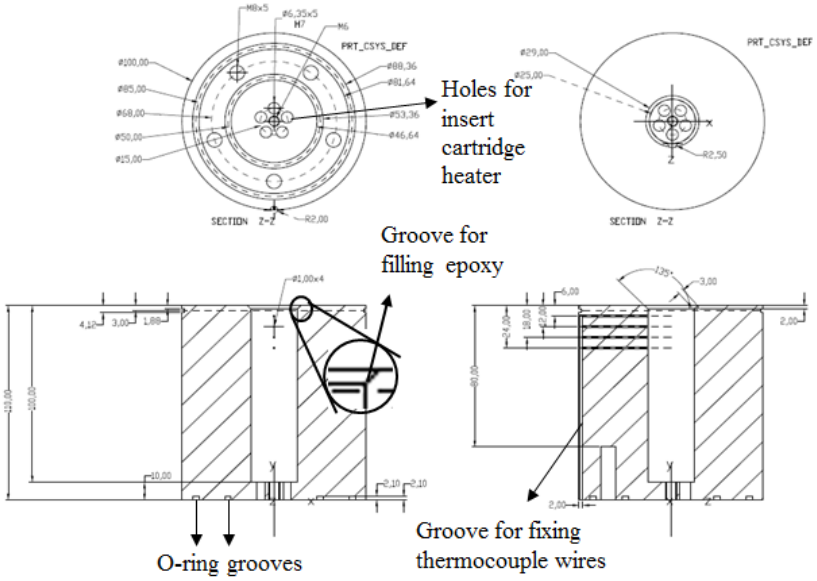

Figure 8 Schematic of PEEK insulation block

A copper heating block of 25 mm in diameter is inserted into the centre of PEEK cylinder shown in Figure 9 and Figure 77 in appendix. It is heated by five 175 W capacity cartridge heaters inside the copper block. The heat flux is obtained by four thermocouples inserted in the copper heater. The input heating power is supplied by a Keysight AC6802A programmable power module.

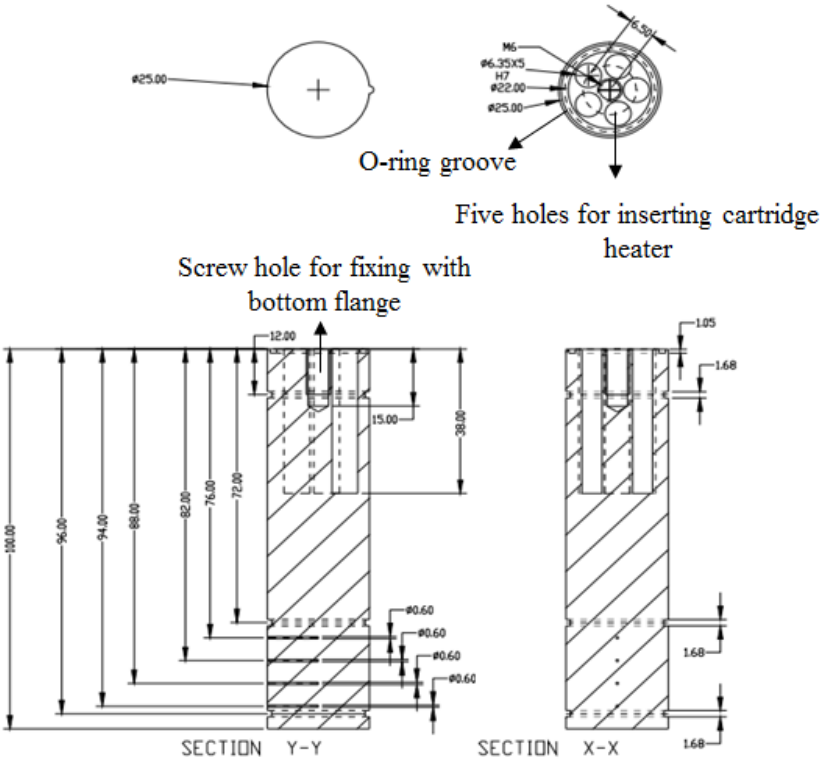

Figure 9 Schematic of copper heater

The test chip is placed on the top of copper heating block. The test chip used in this study consisted of a 30 mm×30 mm square copper chip with a 25 mm×25 mm boiling region as shown in Figure 13. The excess area outside the boiling region is covered with Kapton tape (thermal conductivity of 0.16 W/mK) to prevent boiling. Two thermocouples are embedded in the copper chip to measure the accurate surface temperature. To ensure the tested chips are precisely tightened to the heating surface and minimise the thermal contact resistance between test chip and copper heating block, thermal grease is introduced in conjunction with compression screws, which are applied to apply the same amount of pressure to the chips. High vacuum silicone grease and epoxy are applied around the edge of tested surface to prevent bubble emission from the gap between the chip and PEEK support block.

Figure 10, Figure 11 and Figure 12 show the pool boiling apparatus. Four K-type thermocouples that are 0.5mm in diameter are placed vertically at the centre of the copper heating block (M) to measure axial temperature gradient. All thermocouples with accuracy of ±0.5 K are calibrated before the experiment and all the temperature data is recorded by an Agilent 34972A acquisition system. High temperature silicon rubber O-rings are used in the gap between copper heater and PEEK block for sealing purpose. An auxiliary immersion pre-heater (B) is connected to a proportional integral derivative controller with K-type thermocouple (G) measuring bulk temperature, which controls the temperature fluctuation of bulk liquid and maintains the liquid temperature at the expected value. Reflux condenser (C) is connected to a water bath (E) to prevent evaporation water loss from the test pool and maintain atmospheric pressure inside the pool. A hole can be opened to air on the upper flange plate if the inside pressure is required at atmospheric pressure. Deionized water is used as the working fluid and it is degassed by continuously boiling for at least one hour before experiment. The bubble dynamics on the test surface are captured by of a high-speed camera (Phantom v12.1) with a recording speed of 1000 frames/s. 2 LED lights with a DC light source are applied in front of the pool boiling vessel. To improve the illumination, a white panel is placed behind the test chip to reflect lights onto the surface.

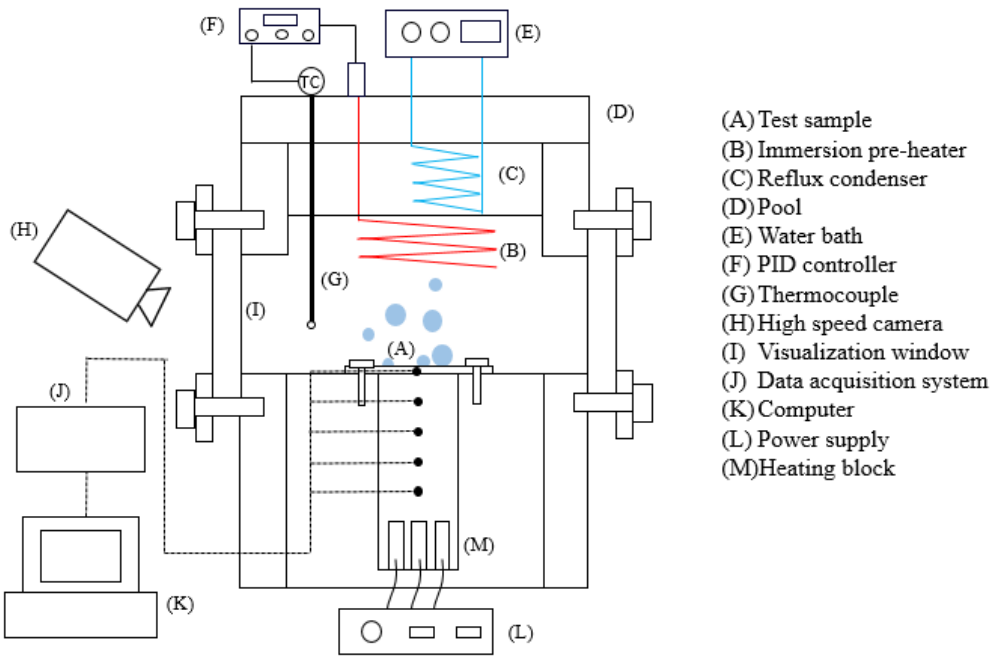

Figure 10 Experimental schematic of pool boiling

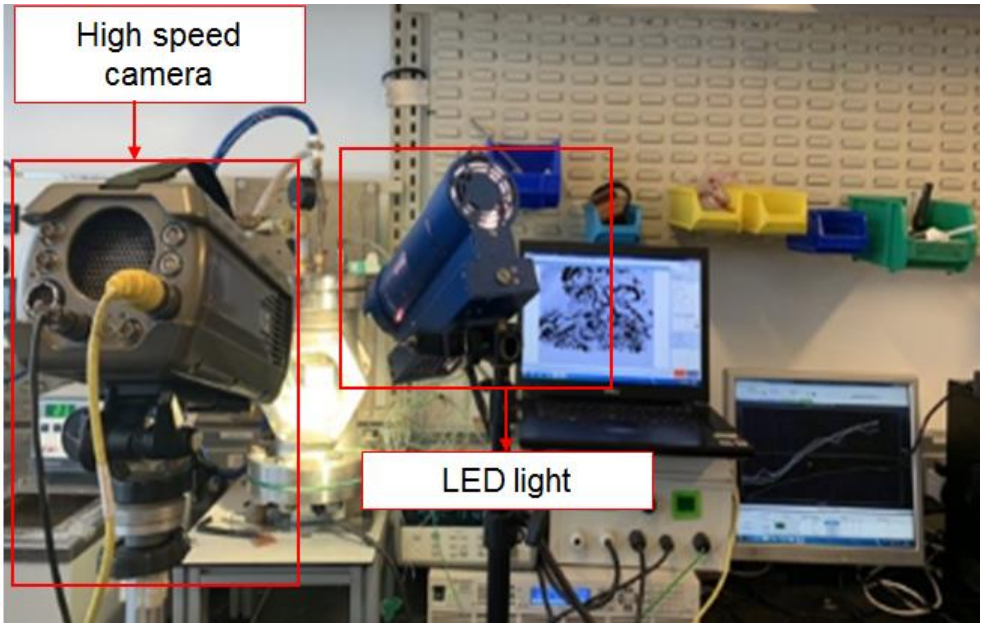

Figure 11 Pool boiling facility with high speed camera and light.

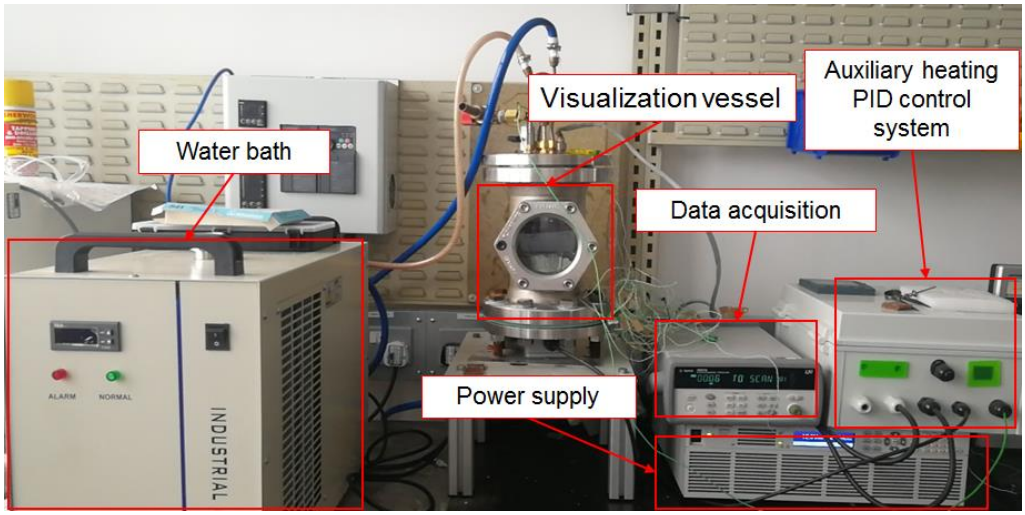

Figure 12 Experimental apparatus of pool boiling

The heat input of copper block is increased at an interval of 20-40 W by controlling the applied electric power. The heat flux is obtained the with Fourier's Law:

$$q = -k_{cu}\frac{dT}{dx} \tag{12}$$

The surface temperature also can be calculated by using (13. The thermal conductivity of copper, k and the distance from the thermocouple to the test chip,

$$T_s = T_4 - q\frac{d}{k_{cu}} \tag{13}$$

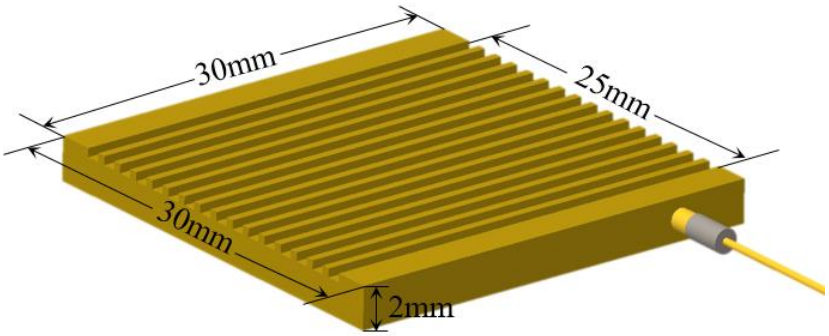

Figure 13 Schemtic of tested boiling chip

3.1.2 Preparations of hydrophilic, hydrophobic and heterogeneous wetting coating

One of the purposes of this research is to investigate the effect of the surface wettability on pool boiling heat transfer. In this study, hydrophilic and hydrophobic nanofluids were prepared to obtain hydrophilic, hydrophobic and heterogeneous surfaces.

Fe_3O_4 -water nanofluid was selected as hydrophilic material. The nanoparticles were prepared by co-precipitation[104]. Firstly, 8.8g of $FeCl_2 – 4H_2O$ and 24g of $FeCl_3$- 6 H_2O was dissolved in 100 ml of water and then the mixture solution was heated up to 50 $^{\circ}$C. Next, oxygen was removed by bubbled with N_2. 50 ml of ammonium hydroxide was added and the liquid was stirred for 30 minutes. After that, the black precipitate stayed at the bottom of flask and was collected with a magnet. After being washed with water for 5 minutes, the black precipitate was dispersed into 120 ml of water with the aid of ultrasonic treatment. Next, citric acid was added and the suspension and was stirred at the temperature of 50 $^{\circ}$C under the protection of N_2 for 2.5 hours. The diluted HCl solution was used for washing the particles. The citric acid modified Fe_3O_4

particles were dispersed again in water after the dumping the supernatant and the concentration of nanoparticles in water was 0.25% by volume.

The hydrophobic nanofluid was fabricated as follows[105]. The hydrophobic nanofluid is prepared by using a combination of nanoparticles and functional materials in solution. Firstly, polydimethylsiloxane (PDMS) with molecular weight of 95000 was dissolved in the solution of white spirit, which forms the solutions with concentration of 6 wt%. Next, silica nanoparticles (14nm) were added into the solutions to form colloidal nanosuspensions. The concentration of nanoparticles in solution was 2 % weight in gram/v in millilitre. Finally, the hydrophobic nanofluid was fully mixed for 30 min using a magnetic mixer stirrer.

Before preparing hydrophilic, hydrophobic and heterogeneous wetting surfaces, the copper surfaces were polished and cleaned. Then, the nanosuspension with 1.5 ml was poured in air brushing and sprayed onto the surfaces. The coated surface was dried in an oven at 50 $^{\circ}$C overnight before testing. Figure 38 shows the fabrication procedure of the heterogeneous wetting surface.

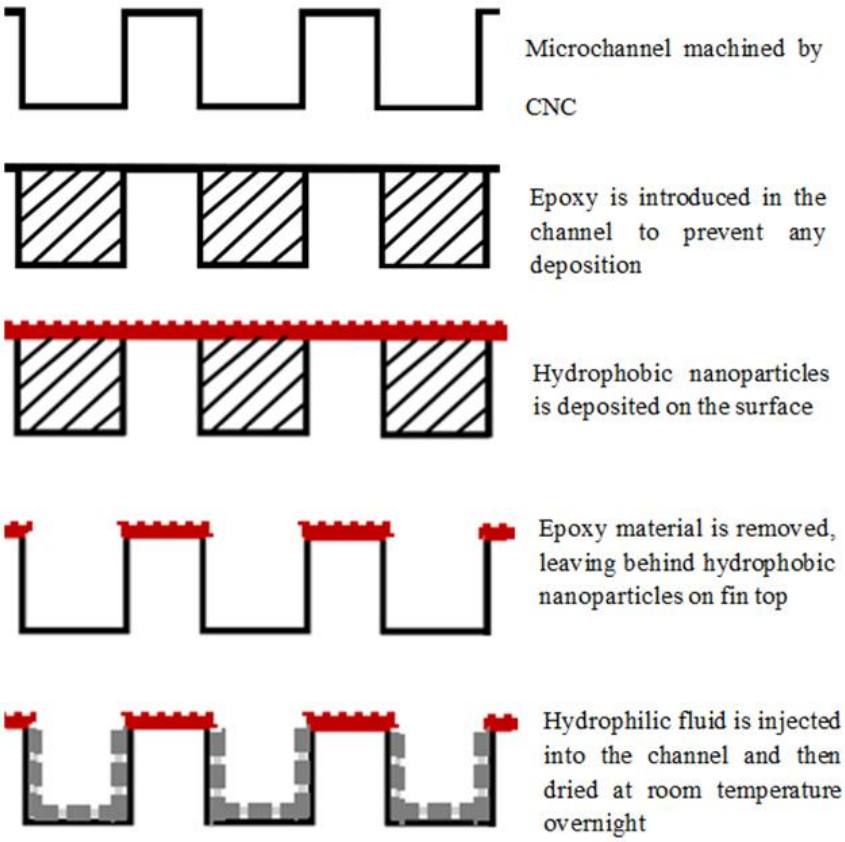

Figure 14 Fabrication of heterogeneous wetting surface

The contact angles were measured at the ambient temperature before conducting boiling experiments. Figure 15 demonstrates the static contact angle of a droplet on a solid surface. Based on Young's equation[106], the contact angle can be determined by liquid/vapour, liquid/solid and solid/vapour interfacial tensions. As shown in Figure 16, Figure 17 and Figure 18, the plain copper surface with a static contact angle of 73° becomes highly hydrophobic and hydrophilic after the deposition of the PDMS-silica and Fe_3O_4 nanoparticles, respectively. The contact angles were measured to be 145° for hydrophobic surface and 14° for the hydrophilic surface.

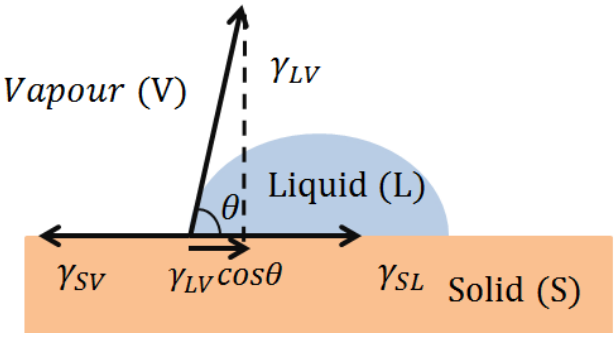

Figure 15 Schematic of the static contact angle of a droplet on a solid surface and graphical dervation of Young's equation

Figure 16 Water static contact angle on uncoated copper surface

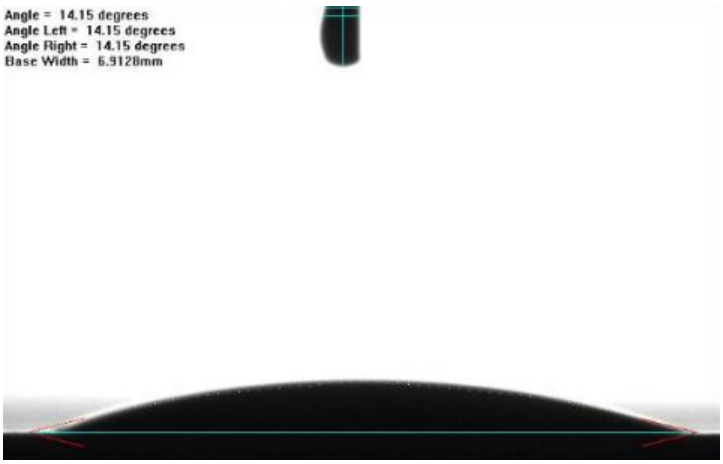

Figure 17 Water static contact angle on Fe_3O_4 nanoparticles coated copper surface as a hydrphilic surface

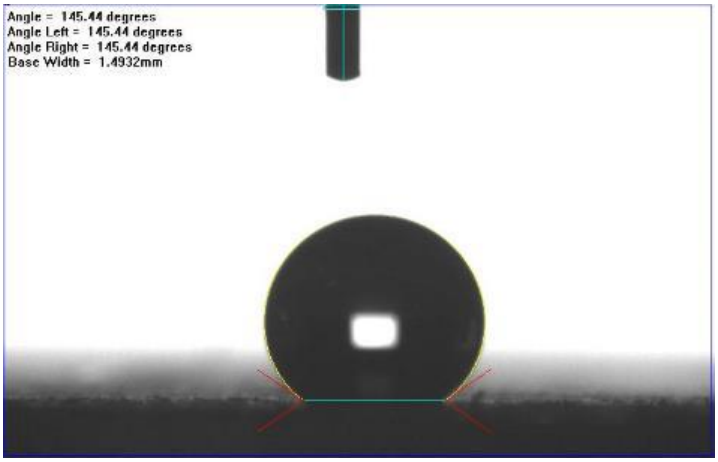

Figure 18 Water static contact angle on PDMS-silica nanoparticles coated copper surface as a hydrophobic surface

Figure 19 and Figure 20 show the SEM images for PDMS and Fe_3O_4 nanoparticles coated on the copper surface. As shown in Figure 19 (b), it can be seen that the silica nanoparticles are irregular and the diameter ranges from 30 to 80 nm, which is larger than the particle size, 14 nm, provided by the manufacturer. This is attributed to the strong tendency to agglomerate caused by van der Waals attraction between the particles. As shown in Figure 20, it can be observed that there are many large cracks on Fe_3O_4 nanoparticles coated surface. The crack formation is common for coatings forms during dehydration process of Fe_3O_4 coating. This is attributed to presence of capillary force when solvent evaporates from surface and drying shrinkage.

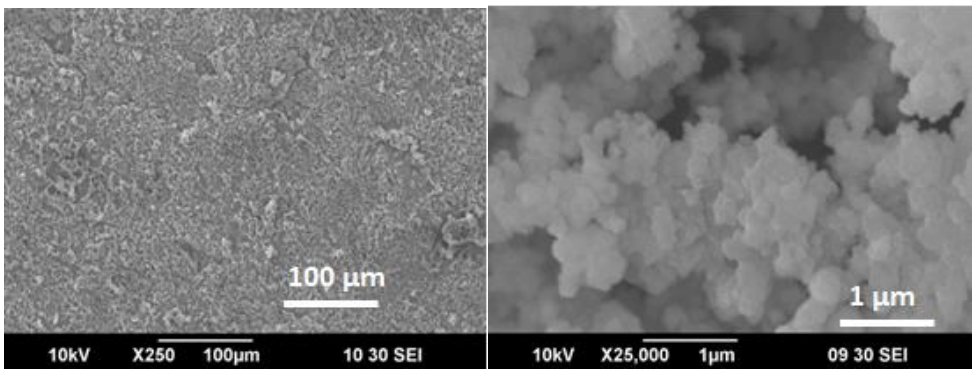

(a) (b)

Figure 19 SEM images of hydrophobic surface (a) at ×250 magnification (b) ×25,000 magnification

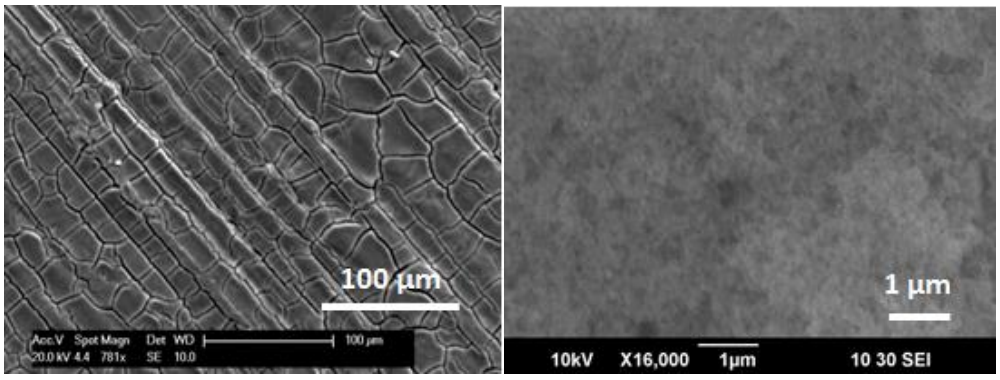

(a) (b)

Figure 20 SEM images for hydrophilic surface SEM images of hydrophobic surface (a) at ×781 magnification (b) ×16,000 magnification

In this research, the heat transfer surfaces used are summarised in Table 11. Plain bare surface is a non-coated copper surface that is polished with 1200 grit sandpaper and the contact angle is 73° in room temperature. As for other surfaces, various surface wettability and channel widths were fabricated to investigate the effects of surface wettability and channel width on thermal performance of pool boiling.

Table 11 Heat transfer surfaces in pool boiling

	Fin width and depth	Channel width	Number of channels	Surface coated
Plain Bare surface				None
W600	600	600	21	hydrophilic
W600	600	600	21	hydrophobic
W600	600	600	21	heterogeneous
W1000	600	1000	16	heterogeneous
W2000	600	2000	10	heterogeneous
W2500	600	2500	9	heterogeneous

3.1.3 Bubble image processing

The bubble growth periods were recording by the high-speed camera with speed of 1000 frames per second. The images were performed by Phantom Camera Control software.

To obtain the bubble equivalent diameter, the bubble diameter D_i is defined by the bubble edge $x_{b,i}$,

$$D_i = \max(x_{b,i}) - \min(x_{b,i}) \tag{14}$$

The unit of d_i is pixel is the equivalent bubble volume V_b in pixel can be calculated by

$$V_b = \frac{\pi}{4} B_{pix,hs}^3 D_i^2 \tag{15}$$

Camera resolution $B_{pix,hs}$ is 60×10^5m/pixel in this study. V_b can be converted into the equivalent bubble diameter $D_b$assuming a sphere of the same volume.

$$D_b = D_{b,volume} = \sqrt[3]{\frac{6}{\pi} V_b} \tag{16}$$

3.1.4 Data reduction and uncertainty

The heat flux is calculated by using Fourier 1D conduction equation,

$$\mathrm{q} = -\mathrm{k_{cu}} \frac{\Delta T}{\Delta x} \tag{17}$$

where $\mathrm{k_{cu}}$ is the thermal conductivity of copper $\Delta \mathrm{T}/\Delta \mathrm{x}$ is the temperature gradient in copper heating block. Δx is the distance between each adjacent thermocouple, and boiling surface and thermocouple T_d, Δx is equal to 6 mm.

The tested surface temperature T_{wall} can be obtained by the equation

$$T_{wall} = T_d - q(\frac{x}{k_{cu}}) \tag{18}$$

To make sure the heat flux is transferred by 1D conduction to the test surface heat loss is analysed. The equation (18) suggests that temperature distribution in the test section is expected to be linear. Figure 21 shows the temperature of T_a, T_b, T_c and T_d at heat flux of 12W/cm^2, 29W/cm^2, 53W/cm^2 and 77 W/cm^2 for bare plain chip. It is found that temperature is linear with the distance. The heat flux is proportional to the thermal gradient and $\frac{dT}{dx}$ is a constant at any point along

the axis of the copper heater. Therefore, the heat loss along the length of the copper heater can be neglected.

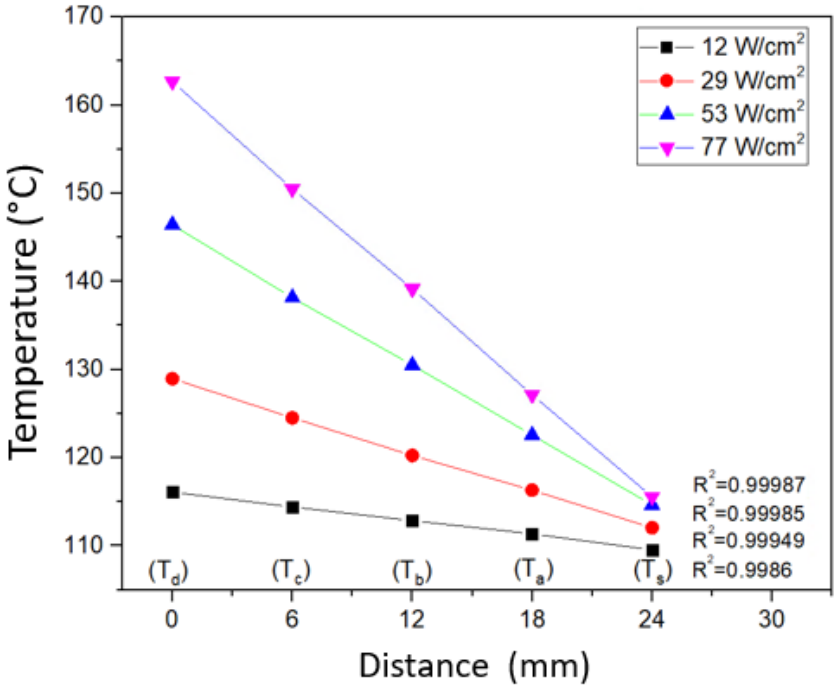

Figure 21 Temperature distribution in heat flux of 12 W/cm^2, 29 W/cm^2, 53 W/cm^2 and 77 W/cm^2 plotted between T_d and T_a for uncoated copper surface

The heat transfer coefficient can be calculated by using equation:

$$h = \frac{q}{T_w - T_s} \tag{19}$$

T_w is surface temperature and T_s is saturated liquid temperature, q'' is the heat flux transferred from heater to the liquid. It can be calculated by using equation (20)

$$q = \frac{VI}{A_c} \tag{20}$$

where V and I are voltage and electric current of heater and A is the heat transfer area. In this experiment, the heater is isolated by PEEK block with low thermal conductivity of 0.25W/mK, therefore one-dimensional conduction heat transfer is the dominant.

The heat input value obtained from the measurements of voltage drop (V) and current (I) of the power supply. Uncertainty analysis is carried out by using method proposed by Kline and McClintock [107] as shown below.

$$\mathrm{U_q} = f(V, I, A) \tag{21}$$

$$\frac{U_q}{q} = \sqrt{\frac{U_V^2}{V^2} + \frac{U_I^2}{I^2} + \frac{U_{A_c}^2}{A_c^2}} \tag{22}$$

The heat flux measurement uncertainty was estimated as 3.5% caused by current, voltage and surface area of heater. The maximum uncertainty on individual temperature measurements are estimated as ±0.5 K in full scale.

A plain copper surface has been tested to compare to the plain copper surface data in literature, as shown in Figure 22. The boiling curve agrees with other researchers' experimental results such as Partil[108], Wang[109], Akbary[110], Gheitaghy[111], Mori [112] and Takata[13]. The plain copper surface has slightly lower heat flux than the plain surfaces for several studies at high superheat. This could be attributed to the lower roughness of the plain copper surface of 0.38μm used in this study.

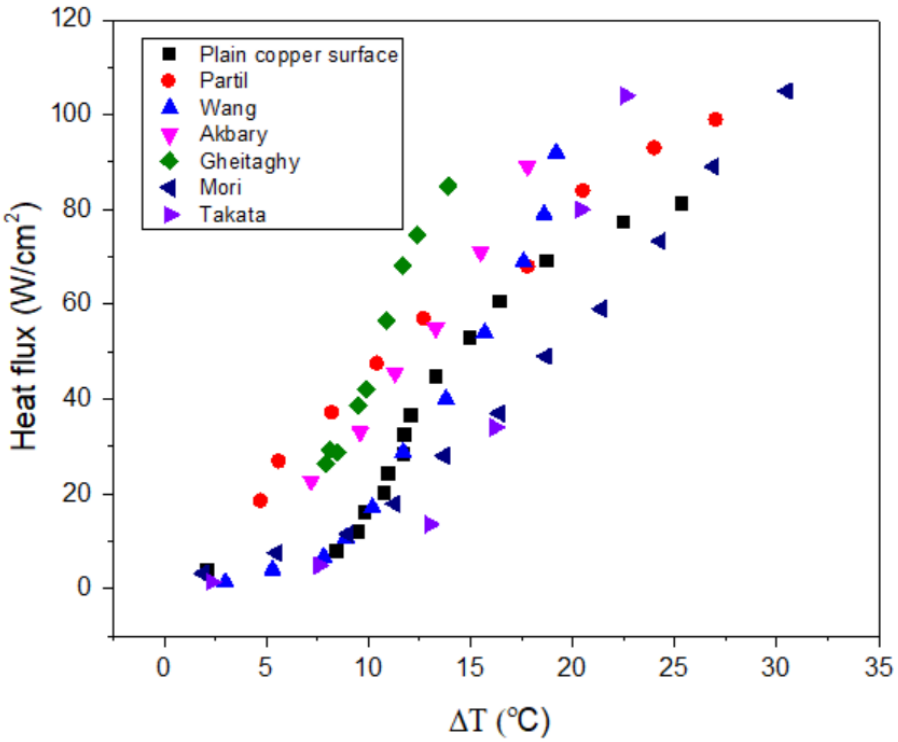

Figure 22 Comparison of experimental boiling curve and plain copper surface data in literature

3.1.5 Experimental procedures

The pool boiling experiments are carried out under 14 different heat flux conditions, from 4.1 W/cm^2 to 101.9 W/cm^2. Seven surfaces are tested. In this measurement, the visualisation system is equipped with two LED illumination sources for high speed camera. The camera is positioned to monitor on the tested surface. The camera frame rate is set at 1000 frames/s with exposure time of 260 µs. Each image acquired consisted of 800×600 pixels.

Before the experiment, the test vessel was cleaned since the amounts of dust matter could be consequential in pool boiling of rough surfaces and change the boiling behaviour. Therefore, the test vessel was thoroughly rinsed in distilled deionised water prior to each test. Next, two thermocouples were embedded in

the tested chip to measure the accurate surface temperature. To ensure the tested chips are precisely tightened to the heating surface and minimise the thermal contact resistance between test chip and copper heating block, the thermal grease is introduced in conjunction with compression screws applying the same amount of pressure to the chips. After that, the distilled deionised water was poured into the vessel and top cover flange with auxiliary heater and condenser attached was fixed with the test vessel. The heating power was then applied to the cartridge heaters and auxiliary heater. After the temperature of working fluid was increased to the saturation temperature, the heating power was maintained for 1 hour to degas the working fluid. During the degassing process, the attached condenser was opened and the chilled water was kept at 20 °C to condense the vapour flowing back by gravity into the test vessel. At the end of an hour degassing process, the cartridge heater and the auxiliary heater were turn off and the valve on condenser was closed. The inner pressure was checked to ensure that it corresponded to the saturation temperature.

To start the test, power supply was applied to condenser, heater, data taker and PID controller. The heating power was applied to the cartridge heaters from 4.1 W/cm^2 to 101.9 W/cm^2. The temperature measured by thermocouples attached to the heater and tested surface were monitored every 10 seconds. After the difference between consecutive averages was below 0.1 ˚C, it is assumed as steady state, and the temperature and applied heating power were recorded. Then the heating power was incremented to the next value. The temperature and power were recorded again until it reached the next steady state. All devices were turned off and all data including temperature, power and video was saved when the experiment was completed.

3.2 Results and discussions

3.2.1 Enhanced pool boiling heat transfer mechanism by controlled wettability patterns

3.2.1.1 Nucleate boiling on hydrophilic, hydrophobic and heterogeneous surfaces

In this section, boiling experiments are conducted for bare copper chip, hydrophilic channel, hydrophobic channel chip, and heterogeneous channel chips by using deionised water as working fluid at atmospheric preesure. The boiling curves for these four surfaces are shown in Figure 23. The heat flux is increased linearly with superheat after the ONB, which indicates the presence of the nucleare boiling regime. Heterogeneous and hydrophobic wetting surfaces experience a very short convective boiling regime and low wall surperheat at ONB, which is much earlier than on a bare copper surface and hydrophilic surface[16]. This is implies that the heterogenous and hydrophobic surface can suppress the temperature excursion. For example, ONB is initiated at superheat of 0.7 ^{o}C for the hydrophobic and heterogeneous surface and 8.2 ^{o}C for bare copper. The effective heat flux of all surfaces with channel exceeds 100 W/cm^2 without reaching the critical heat flux, however bare copper surface reaches critical heat flux at heat flux of 85 W/cm^2. Compared with a bare surface without channel, the critical heat flux is delayed for the chips with channels due to increased nucleate sites and capability of suction of liquid into inside channel. Heterogeneous surface achieves a lower wall surperheat at a given heat flux; for example, the wall superheat achieved at heat flux of 77 W/cm^2 at the superheat of 10.4 ^{o}C for heterogeneous surface, 11.3 ^{o}C for the hydrophobic surface, 17.1 ^{o}C for hydrophilic surface and 22.5 ^{o}C for bare copper surface.

Heat transfer coefficient data recorded for these four surface is shown in Figure 24. The heterogeneous surface has a higher heat transfer coefficient than others at any given heat flux due to high capillary suction inside the channels and high density of nucleate sites on top of fin, which improves the bubble growth and departure and also provides sufficient liquid replenishment. Meanwhile, the fast emission bubble releasing from inside of channel can cause a disturbance near the top of pin, improving bubble departing from the top of pin. The maximum heat transfer coefficient of heterogeneous, hydrophobic and hydrophilic wetting surfaces are 81.5 kW/m^{2}K, 77.4 kW/m^{2}K, 50.4 kW/m^{2}K, respectively, which are much higher than 32.2 kW/m^{2}K of bare copper surface. This improvement can be explained by that channel structure can enhance the boiling heat transfer with its large heat transfer area, liquid capillary force and more cavities.

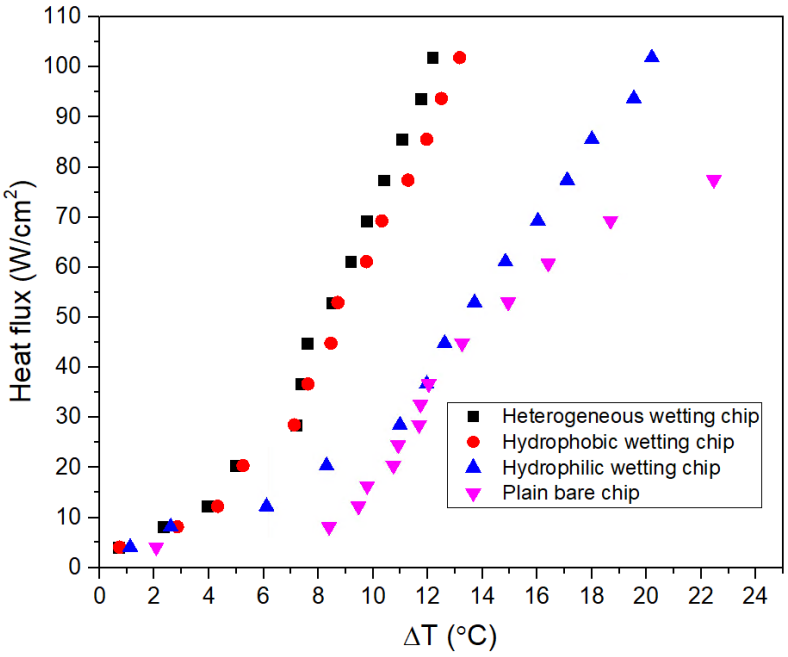

Figure 23 Boiling curves on surface wettability modified chips

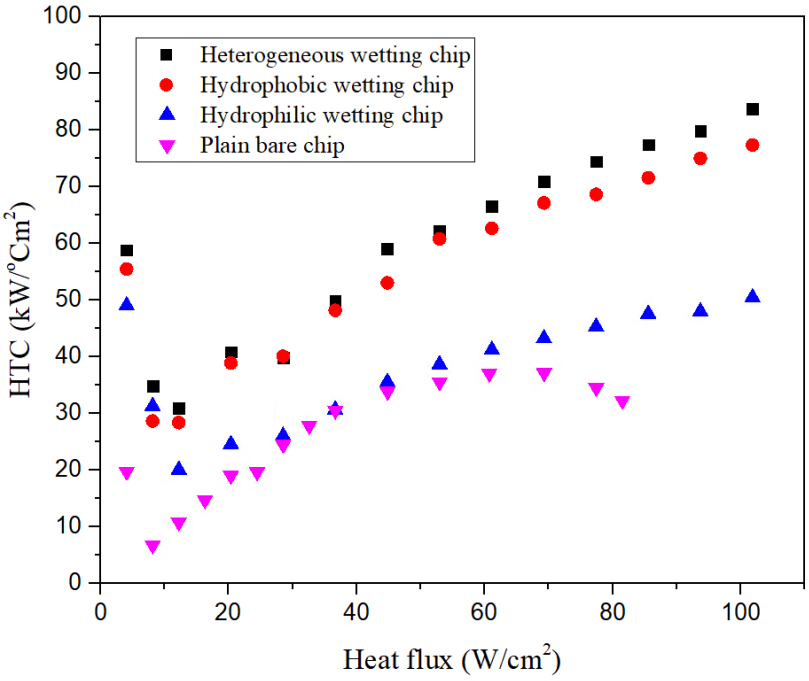

Figure 24 Boiling heat transfer coefficients on surface wettability modified chips

3.2.1.2 Bubble dynamics on heterogeneous wettability surfaces

In this study, the bubble growth process was recorded by high speed camera with speed of 1000 frames/s. In order to obtain clearly images, the side view of boiling process were recorded. Figure 25, Figure 26, Figure 27 and Figure 28 show the comparion of bubble growth process with increased heat flux. At low heat flux, discrete bubbles occur on all surfaces as shown in Figure 25. It can be found that more bubbles are formed on hydrophobic channel chip than the other two chips and bubble departure diameter is smallest for the hydrophilic channel chip. This is because large wall surperheat is required for high wettability surface to generate bubble. On the hydropilic chip, most bubbles necleate in channel due to higher temperatuire in the compared with top of fin. However, bubble distribution more evenly in the channel and on the top of fin for

hydrophobic and heterogeneous chips. This is because the hydrophobic area requires lower wall superheat to active nucleate site.

With an increase in heat flux to 20.4 W/cm^2, more nucleate sites are actived for the three chips, as illustrated in Figure 26, which leads to a great amount of heat to be dissipated by these stable and quick bubble emissions. Dhir [113] proposed empirical correlations as the following forms:

$$N_a \sim \mathrm{q}^{2\sim4} \text{ or } N_a \sim \Delta T^{4\sim6} \tag{23}$$

However, bubble density on a hydrophilic channel is still lower when compared with the hydrophobic and heterogenous channel chip, which is in agreement with Wang and Dhir's correlation[114]. They proposed an empirical correlation of N_a in terms of contact angle during pool boiling of water at atmospheric pressure. The correlation is expressed by

$$N_a = 7.81 \times 10^{-29}(1 - cos\theta)R_c^{-6} \tag{24}$$

It is found that the active nucleation site density decreases with the enhancement of the surface wetting. Based on the boiling theroy of Mikic and Rohsenhow[40], it states that heat transfer coefficient depands linearly on the density of nucleation sites as expressed in equation (25).

$$\mathrm{HTC} = 2\left(\pi \mathrm{k_l} \rho_l c_{pl}\right)^{\frac{1}{2}} N_a D_b^2 f^{\frac{1}{2}} \tag{25}$$

As heat flux continuously increases to 93.8 W/cm^2 shown in Figure 28, more bubbles merge with the adjcent bubbles before they depart from the surface and large vapour columns form. These large coalesced bubbles isolate the chip from

the surrounding liquid and impede liquid replenisment. Heat transfer on hydrophobic chip obeys the periodically-large bubble escape pattern shown in picture k. The large coalesced bubble expands and almostly cover the whole chip, which periodically escapes into the pool. In contrast to the hydrophobic chip, bubbles with small diameter merge after they depart from surface. Merged bubbles don't cover the surface which ensures sufficient liquid replenishment due to capillary suction by hydrophilic channel. However, the amount of nucleate sites are still low at high heat flux and heat can't be dissipated effectively by the bubbles, leading to the increase of wall surheat and low thermal performance. The heterogeneous channel chip combined both advantages from the hydrophilic and hydrophobic regions. On the top of fin, hydrophobic regions provide nucleate site to form more bubbles and hydrophilic area ensure sufficient liquid replenishment in vertical and horizontal direction inside the channels to maintain continiously bubble nucleation. In addition, only few vapour columns form and most bubbles diameters are relatively small. Therefore, more heat is dissipated efficiently from heterogeneous chip to liquid.

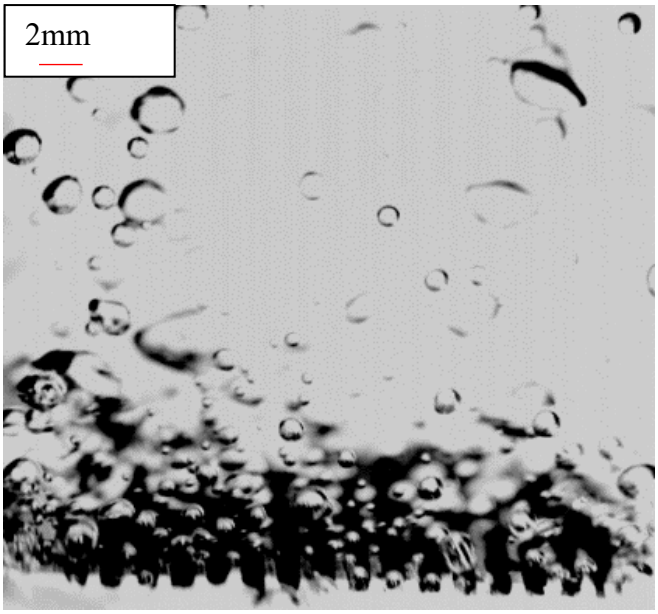

(a) Hydrophilic wetting surface

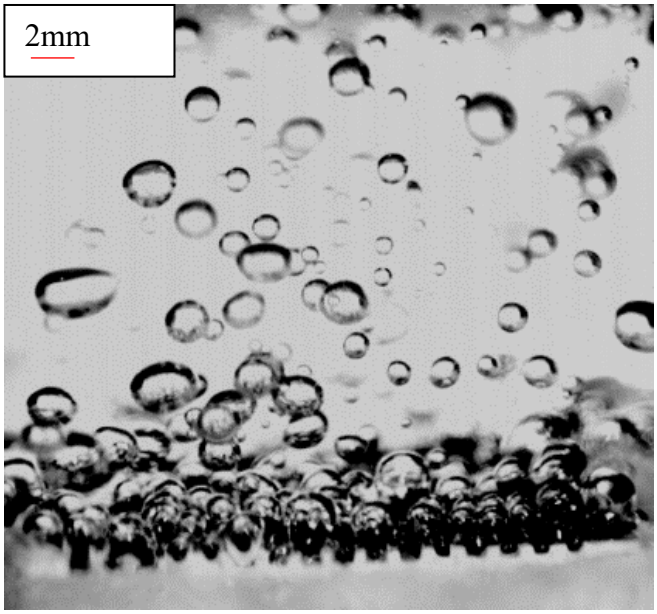

(b) Hydrophobic wetting surface

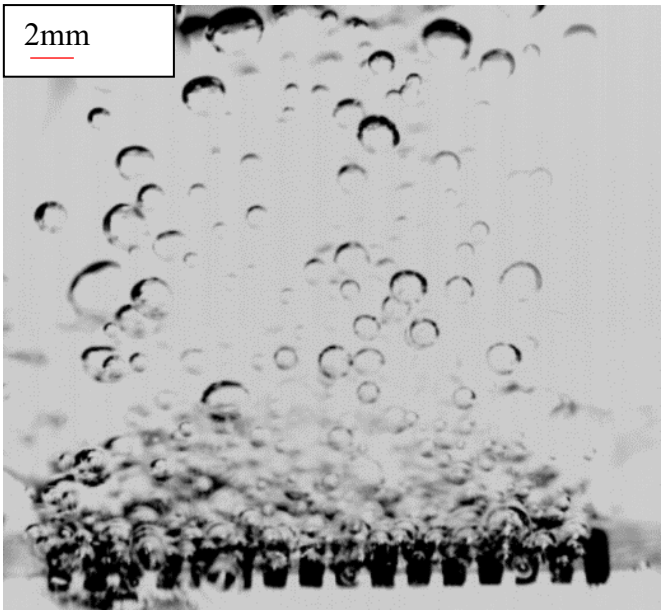

(c) Heterogeneous wetting surface

Figure 25 Recorded photographs of growing bubbles at applied heat flux of 12.2 W/cm^2

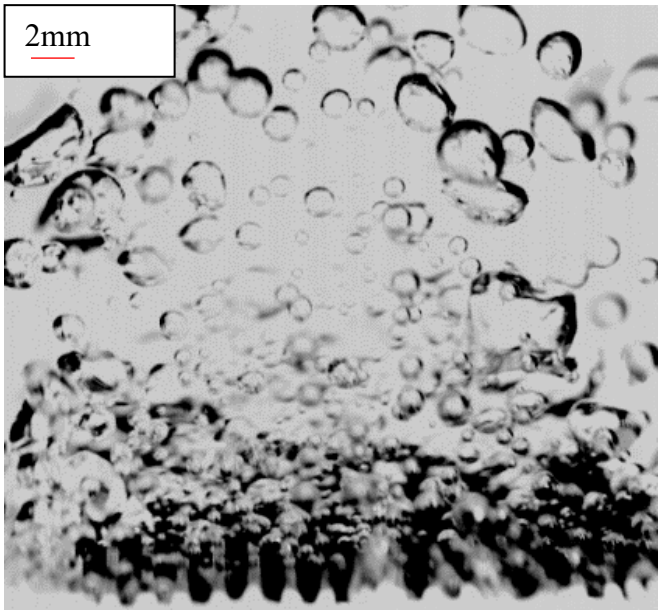

(a) Hydrophilic wetting surface

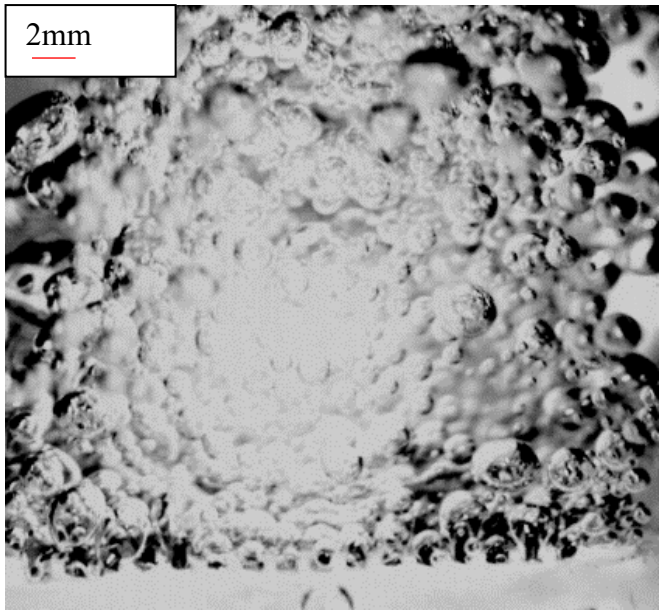

(b) Hydrophobic wetting surface

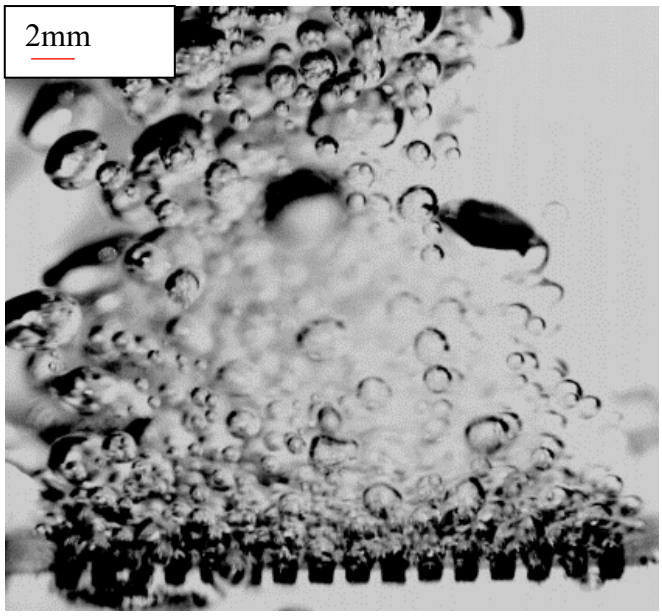

(c) Heterogeneous wetting surface

Figure 26 Recorded photographs of growing bubbles at applied heat flux of 20.4 W/cm^2

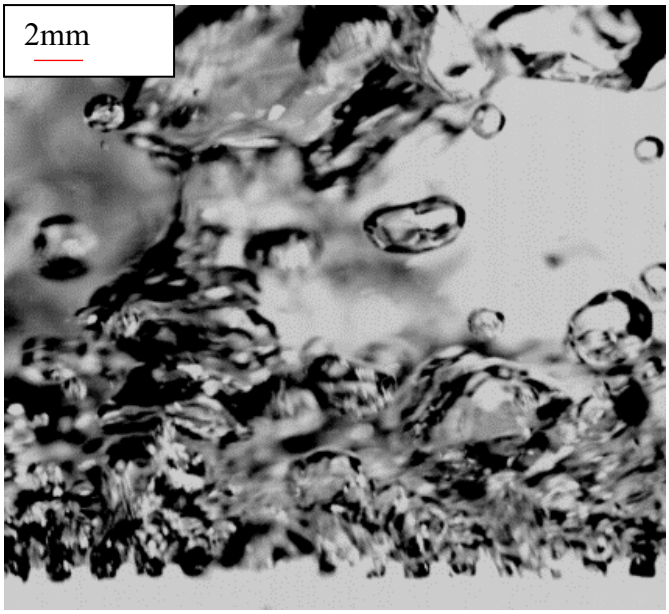

(a) Hydrophilic wetting surface

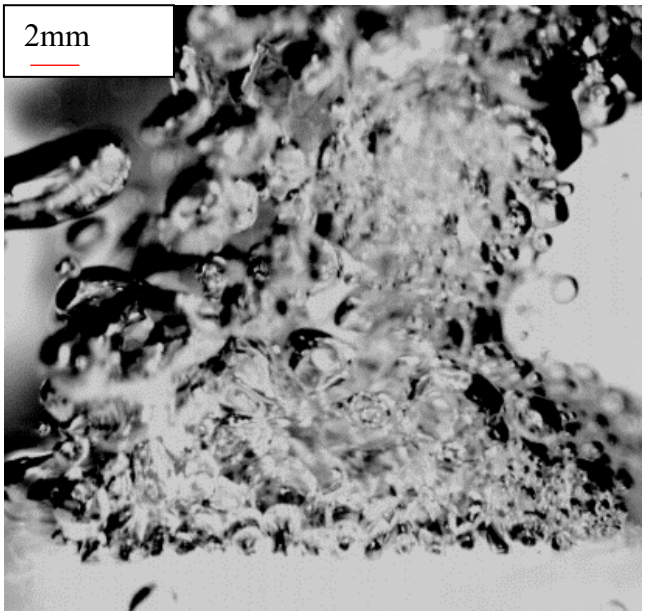

(b) Hydrophobic wetting surface

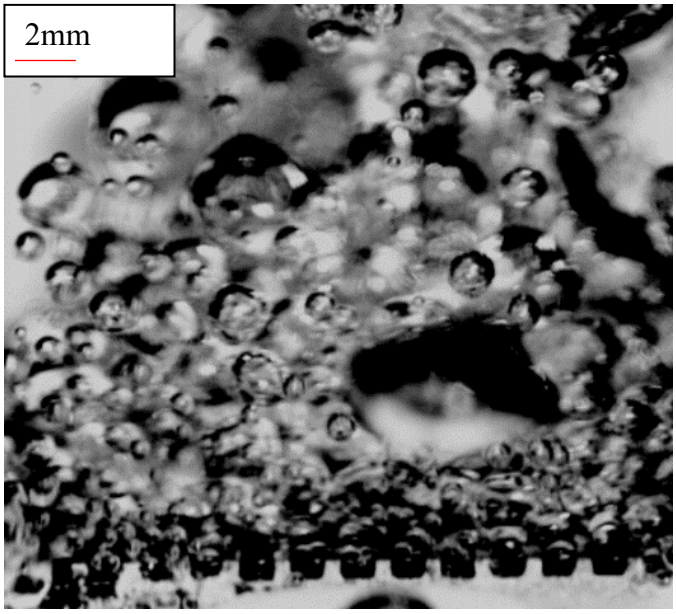

(c) Heterogeneous wetting surface

Figure 27 Recorded photographs of growing bubbles at applied heat flux of 69.3 W/cm^2

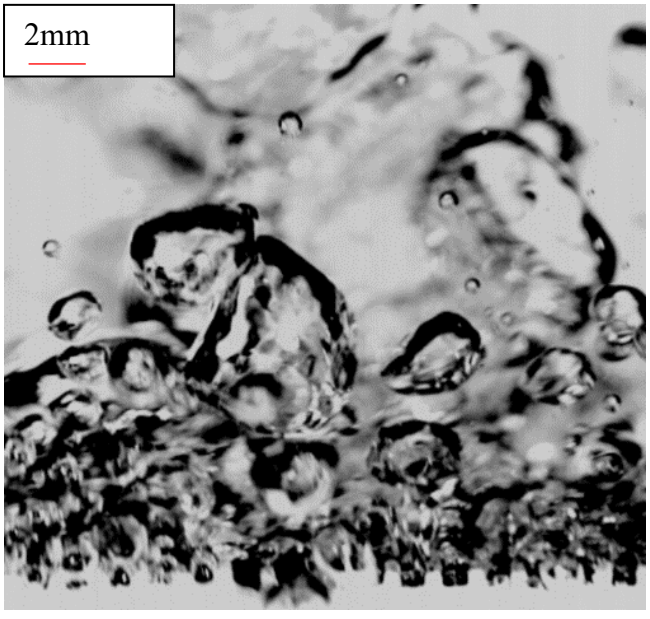

(a) Hydrophilic wetting surface

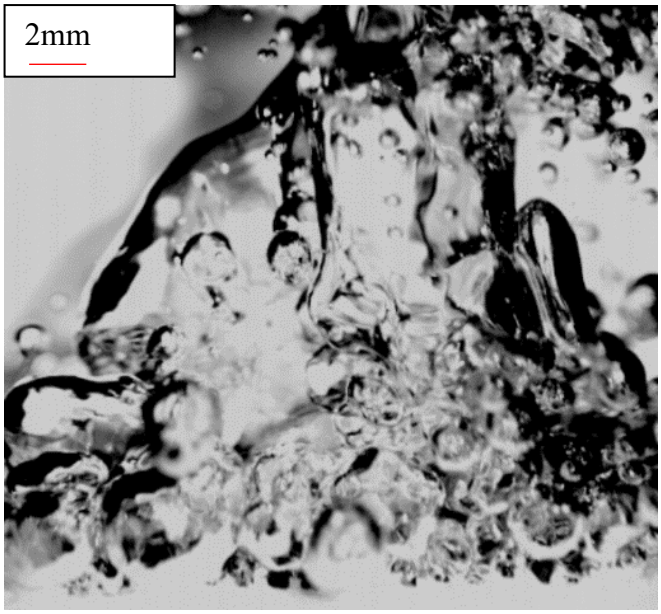

(b) Hydrophobic wetting surface

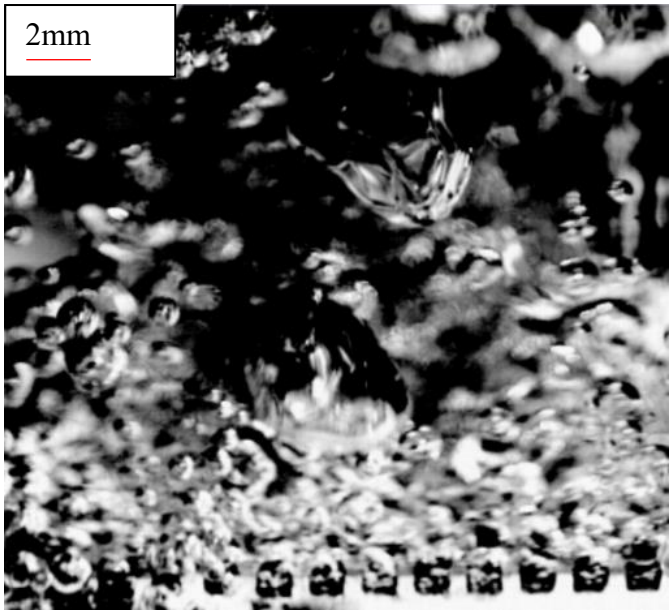

(c) Heterogeneous wetting surface

Figure 28 Recorded photographs of growing bubbles at applied heat flux of 93.8 W/cm^2

To present a better understanding of boiling enhancement mechanism of heterogeneous wetting channel surface, high speed visualisations at 1000

frame/s were used to determine the bubble diameter and bubble growth rate. Bubble formation and growth process from initation to departure at heat flux of 12.2 W/cm^2 for the three chips are illustrated in Figure 29, Figure 30, and Figure 31. The images were captured from the side view to investigate bubble dynamics which has significant effect on boiling heat transfer phenomena. Sucessor bubbles are shown in the dashed line rectangle generates inside the channel and grow to a certain critical diamater on the hydrophilic wetting channel surface. Buoyancy force becomes the main detaching force. Unlike the bubble behavious on the hydrophobic surface, the previous bubble just detaches from the hydrophilic wetting surface and no vapour part remains on the heat surface, as illustrated in Figure 30. After that, it takes 20 ms for re-nucleating to accur and allow the surface to be reheated after departed bubble takes heat away. Griffith and Wallis[50] reported that the required wall superheat to re-nucleate is related to surface wettability. This explains why the hydrophilic chip requires the highest superheat and longest waiting time to initiate next nucleation compared with the other two surfaces. Consequently, longer the waiting time directly affects heat transfer as natural convection heat transfer during the waiting period has a much lower heat transfer coefficient than boiling heat transfer.

$$\Delta T = \frac{2\sigma T_s (v_g - v_l)}{\Delta \mathrm{H}_{\mathrm{vap}} r_c} \tag{26}$$

Once the bubbles grow beyond the the fin on the hydrophobic wetting surface, they grow into the shape of a Taylor bubble shown in Figure 29 (b). Taylor bubbles are described as elongated bubbles and they are commonly found in buoyancy driven processes[115]. As shown in Figure 29 (c), the adjcent two bubbles merge into a bigger bubble with large bubble size and base diameter.

The large base diameter can result in increased downward surface tension force. Consequently, a large volume of bubble is required to increase buoyancy force and then bubble can depart from the surface. This can explain why the bubble generated on the hydrophobic surface has a large departure diameter and a long bubble growth period. Further more, the force changes its direction and it opposes the shrinking of the bubble base if the contact angle is larger than 90^{o}[51]. Therefore, the bubble can maintain its large diameter for a long time and extend the bubble growth period. As shown in Figure 29 (f), the bubble experiences a short necking period before it departs from the surface, and then the remaining part can form a chain of bubble generation without bubble waiting time as shown in a and f, which provides for a better boiling heat transfer.

Figure 31 shows the bubble growth period for a heterogeneous wetting surface. These visuralised results will help investigate boiling heat transfer difference on a heterogeneous surface compared to the hydrophobic and hydrophilic surface. The heterogeneous chip can generate strong capillary suction inside the channels due to the hydrophilic nanoparticle coating, which makes interface between the liquid and bubble unstable. Meanwhile, the fast bubble emission in the channel leads to more chaotic flow induced under the bubbles generated on the top of the fin. Furthermore, the bubbles with fast emission inside the channel enhance the continuous growth of the large bubble and raise the large bubble to a higher position. Therefore, the bubbles more easily depart from the top of fin. The bubble growth cycle is only 69 ms which is shorter than bubble growth cycle of 157 ms for the hydrophobic wetting surface. The bubble departure diamater on the heterogeneous chip is smaller than hydrophobic surface. This is attributed to restriction of bubble base diameter by the area of fin. The surface tension force

stays constant and a large volume of bubble with large buoyancy force is not required to depart from the top of fin. As for bubble emission frequency, the commonly used correlation of bubble generation frequency is proposed by Zuber[43]:

$$fD_d = 0.59\left[\frac{\sigma g(\rho_l - \rho_v)}{\rho_l^2}\right]^{1/4} \tag{27}$$

Equation (27) describes the bubble generation frequency increases with decreasing bubble departure diameter. Therefore, due to the reduced departure diameter, the bubble generation frequency for the heterogenous surface is 2.4 times higher than for the hydrophbic surface. Compared with the hydrophilic surface, the bubbles are continuously generated with no waiting time on the top of the fin with hydrophobic PDMS coating, which means that there is no natural convection heat during this period. In general, the heterogeneous wetting chip combines advantages from both the hydrophilic and hydrophobic area. The hydrophobic area mainly provides large quantity of nucleation sites and low heat flux on ONB, and the hydrophilic area can release the problem of local thermal barrier due to the fast emission, small departure diameter and always being filled with large liquid volume in the channel.

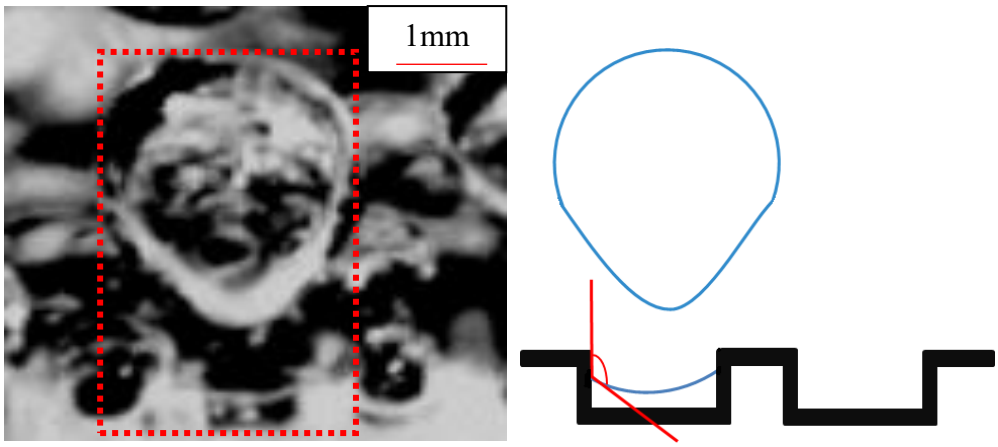

(a) 0ms

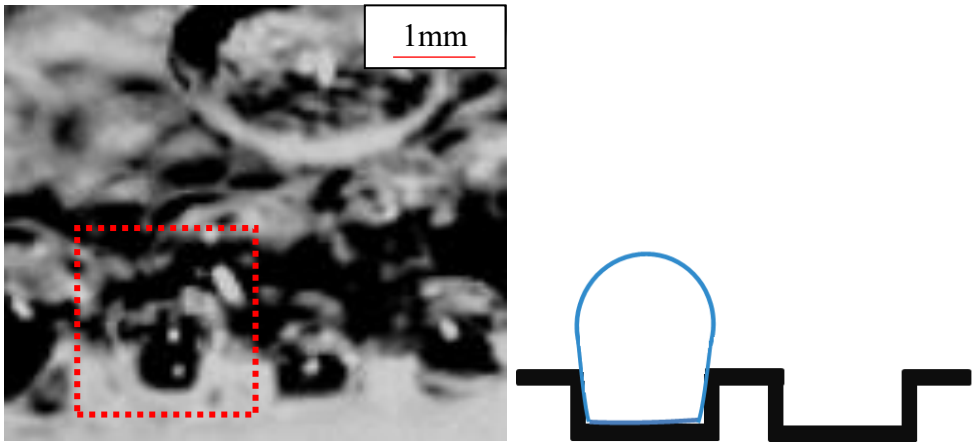

(b) 10ms

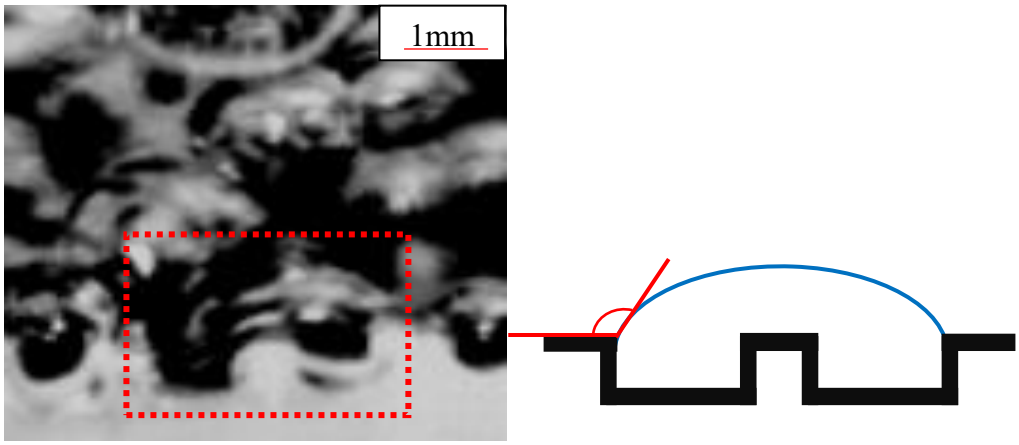

(c) 15ms

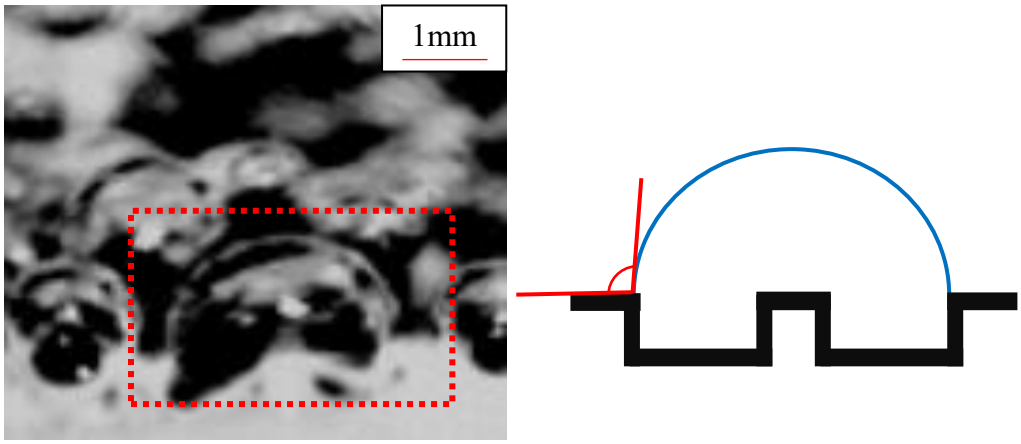

(d) 37ms

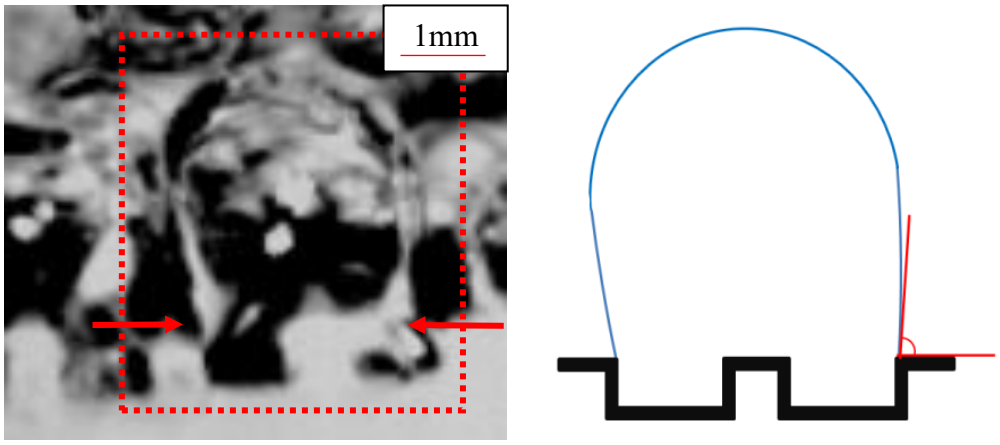

(e) 137ms

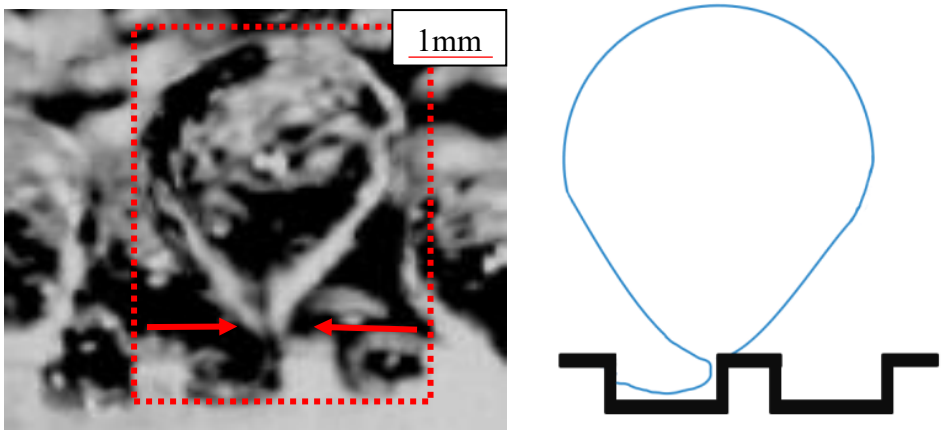

(f) 157ms

Figure 29 Bubble dynamics on the hydrophobic groove surface at 12.2 W/cm^2

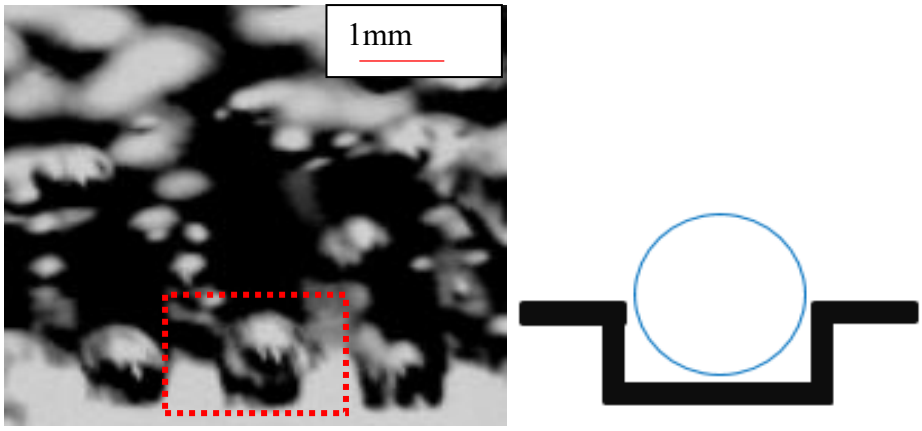

(a) 0ms

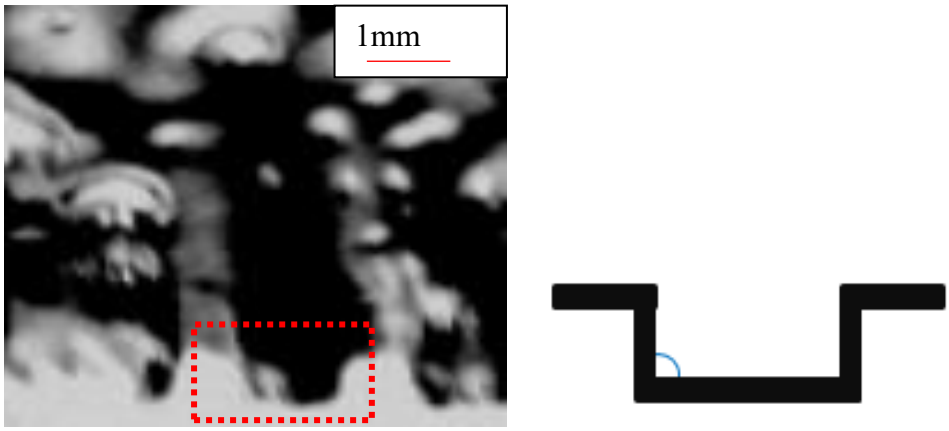

(b) 10ms

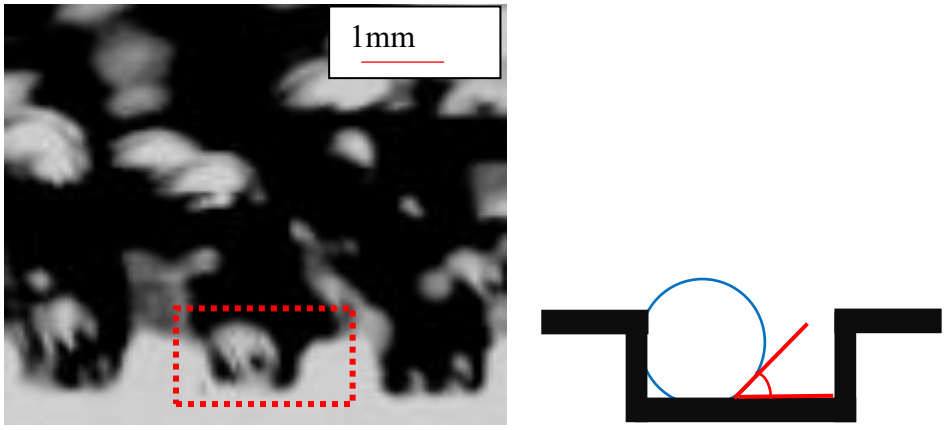

(c) 19ms

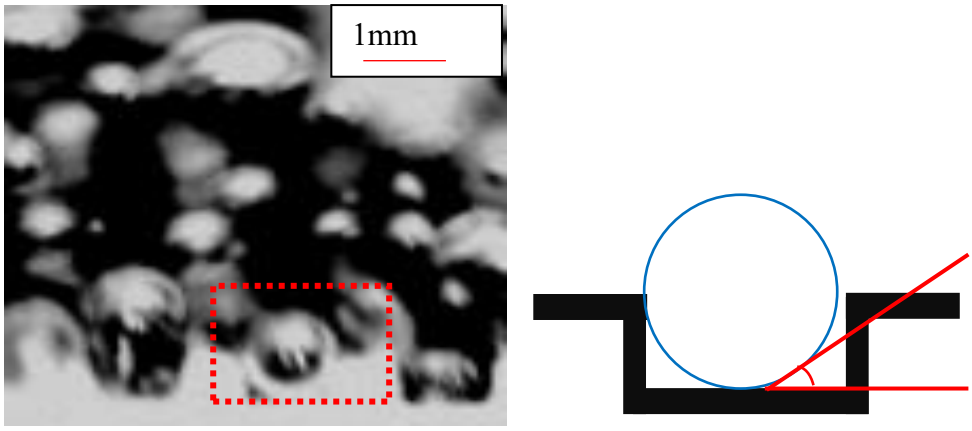

(d) 25ms

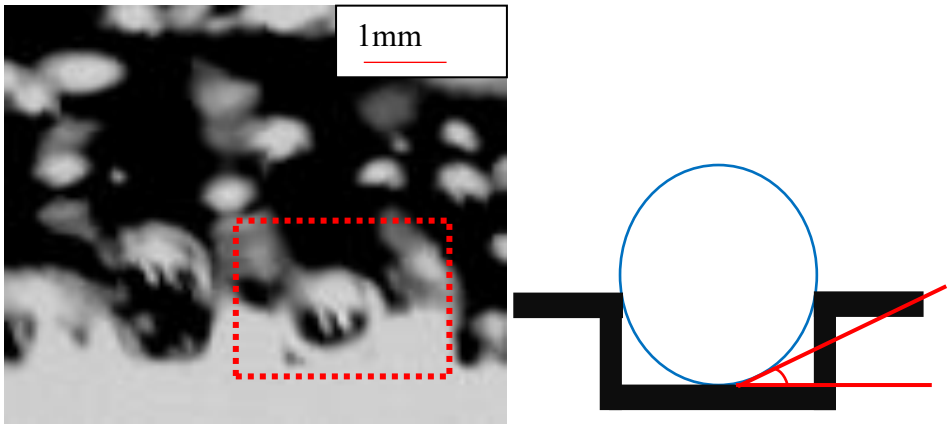

(e) 26ms

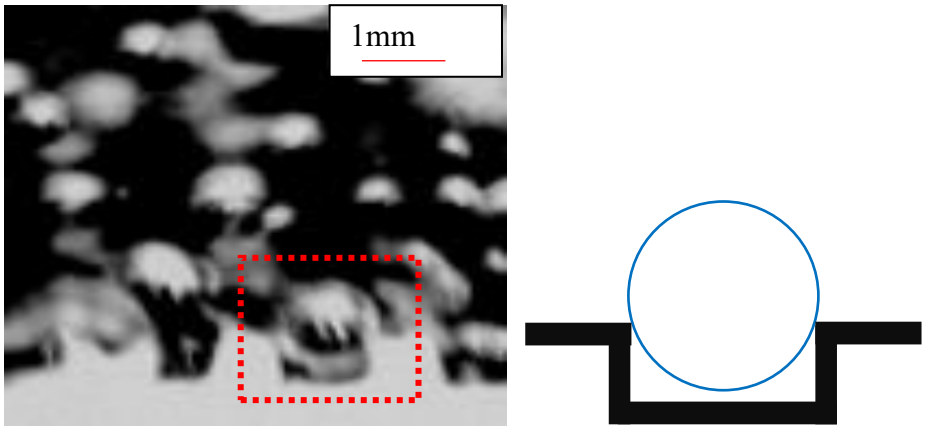

(f) 41ms

Figure 30 Bubble dynamics on the hydrophilic groove surface at 12.2 W/cm^2

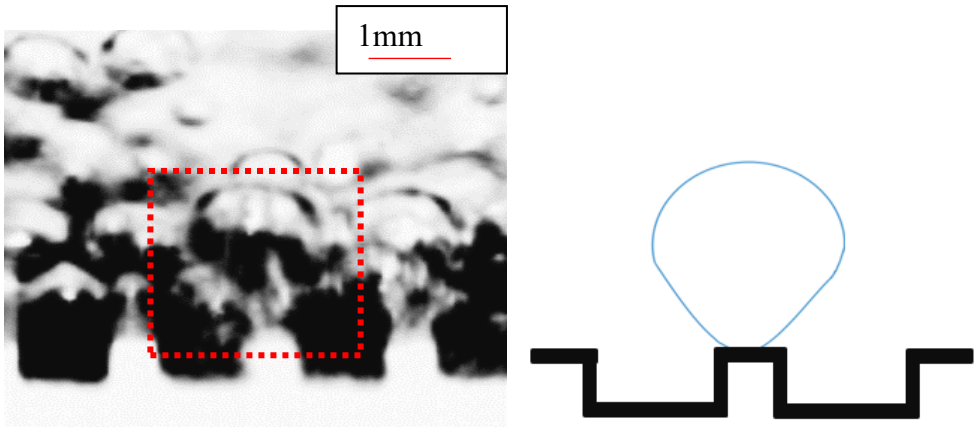

(a) 0mm

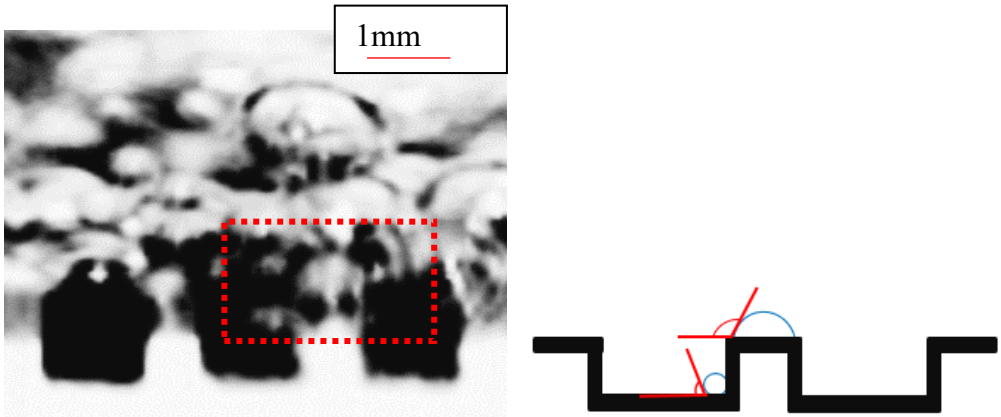

(b) 32ms

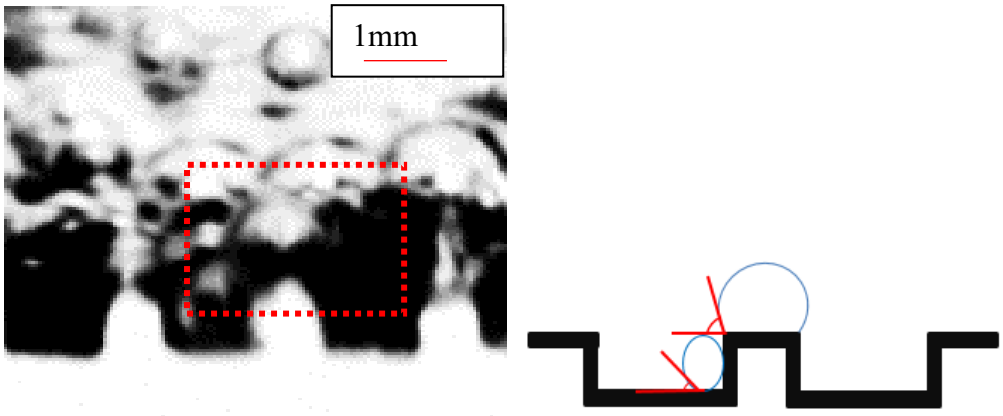

(c) 45ms

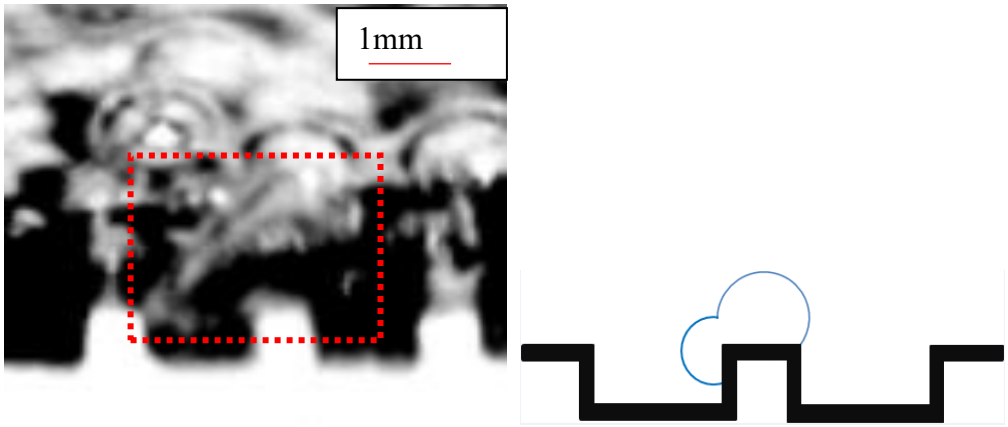

(d) 55ms

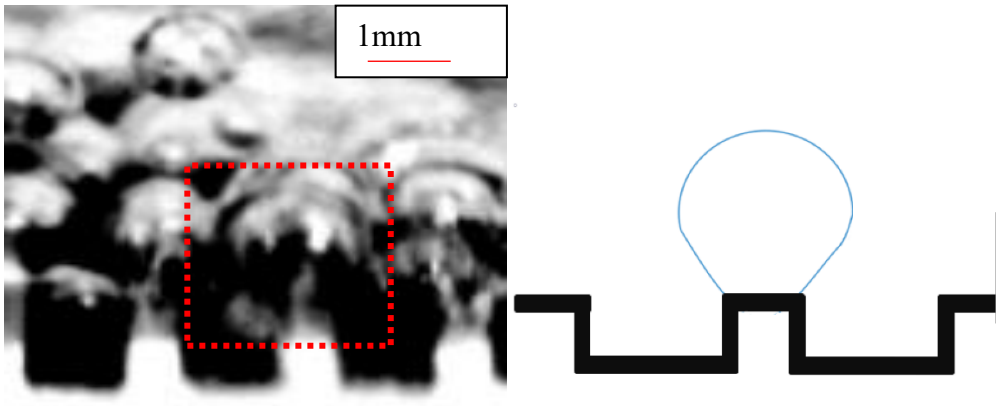

(e) 64ms

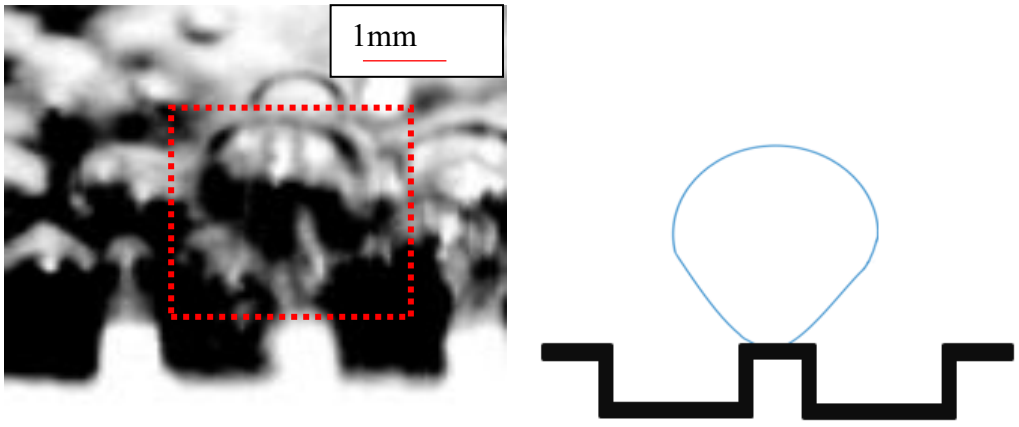

(f) 69ms

Figure 31 Bubble dynamics on the heterogeneous groove surface at 12.2 W/cm^2

3.2.1.3 Bubble departure diameter and emission frequency

For the same nucleation site, bubble departure diameter and growth period are generally uniform. However, it is sometimes found that a bubble with regular size departs and it is immediately followed by several smaller size bubbles. This is because the smaller size bubbles were drawn by the wake behind the previous bubble. Furthermore, a growing bubble may coalesce with an adjcent bubble and depart as a bubble with large diameter. In this section, in order to investigate the bubble diameter and the emission frequency insolated from coalescence, they are based on the count of departing bubbles without coalescence.

Table 12 summarises the average bubble emission frequency and diameter for three surfaces. It can be found that the bubble emission frequency increases as the heat flux increases for all the three surface because the vapour is generated inside the channel at a higher rate, For the same nucleate site, the bubble departure diameters generally keep constant at the same heat flux. As heat flux increase, the bubble departure diameter decrease. Zuber[116] states that the bubble departure is only related to surface tension and buoyancy force at a low heat flux. With increased heat flux, the surface tension of water reduces, which would lead to a reduced bubble departure diameter.

Table 12 Summarised bubble departure diameter and bubble emission

		Hydrophobic chip	Hydrophilic chip	Heterogeneous chip
8.2 W/cm^2	Bubble Departure diameter	3.16 mm	1.16 mm	1.80 mm
	Bubble emission rate	355 ms	40 ms	175 ms
	Bubble emission frequency	2.8 Hz	25 Hz	5.7 Hz
12.2 W/cm^2	Bubble Departure diameter	3.15 mm	1.04 mm	1.37 mm
	Bubble emission rate	194 ms	31 ms	85 ms
	Bubble emission frequency	5.2 Hz	32.3 Hz	12 Hz
20.4 W/cm^2	Bubble Departure diameter	2.69mm	0.93 mm	0.88 mm
	Bubble emission rate	152 ms	24ms	16 ms
	Bubble emission frequency	6.5 Hz	41.7 Hz	60 Hz

Figure 32, Figure 33 and Figure 34 show the bubble growth on the hydrophilic wetting surface at low heat flux of 8.2 W/cm^2, 12.2 W/cm^2, and 20.4 W/cm^2, respectively. It can be found that the bubbles grow faster on the hydrophilic

wetting surface. The bubble growth time reduces from 41 ms to 17 ms as heat flux increases from 8.2 W/cm^2 to 20.4 W/cm^2. Bubble diameter d_i changes nearly linearly with time, which indicates inertia forces govern the entire period. Generally, the bubble is mainly governed by inertia control stage when it grows rapidly following the bubble embryo formation and grows in a hemispherical shape[117]. After the bubble departs from the surface, there is a waiting period for re-nucleating and allowing the surface to be reheated after departed bubble takes heat away. The waiting period reduced from 10 ms to 2 ms as the heat flux increases from 8.2 W/cm^2 to 20.4 W/cm^2, which is attributed to high vapour generate rate at high heat flux. Therefore, the vapour pressure inside the channel requires a shorter waiting time to build up after the previous bubble departs from the nucleate site [118].

Figure 35, Figure 36 and Figure 37 illustrate the change of bubble diameters during bubble growth period and departure period on the hydrophobic wetting surface. During the bubble growth period, the bubble diameter increases quickly after bubble nucleation and then the bubble diameter increase rate slows down until it departs from the surface. At the same heat flux on a same nucleation site, the bubble growth period keeps almostl constant with bubble departure diameter and growth time. After bubble departs from the hyfrophobic wetting surface a short necking forms above the fin surface, and then it leaves behind a nucleus inside the channel, which can form a chain of bubble generation without bubble waiting time. As shown in Figure 36, bubble growth is govened by the inertia control stage before 130 ms due to fast growth, after that the growth speed slows down and the bubble is governed by heat transfer controlled growth. Normally, a surface with moderate and high contact angle yields a slower bubble growth

with diminished inertia effect and the main governing factor is the heat transfer across the liquid vapour interface.

Compared with bubbles on the hydrophobic surface, bubbles on heterogeneous surfaces have smaller departure diameter and shorter bubble growth period as shown in Figure 38, Figure 39 and Figure 40. With heat flux increased to 20.4 W/cm^2, the growth rate is much higher due to increased heat transfer at liquid interface and the whole bubble growth period is fully govened by inertia force, which is refering to Ivey [46] that the growth is govened by inertia force and departure size becomes insensitive to gravity at high heat fluxes for rapid growth bubbles.

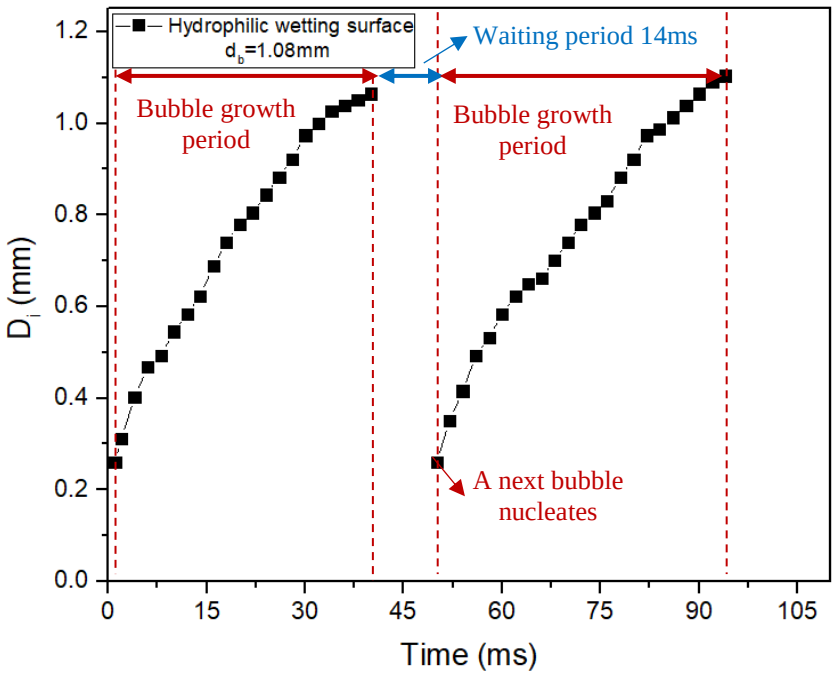

Figure 32 Instantaneous bubble diameter on hydrophilic surface at heat flux of 8.2 W/cm^2

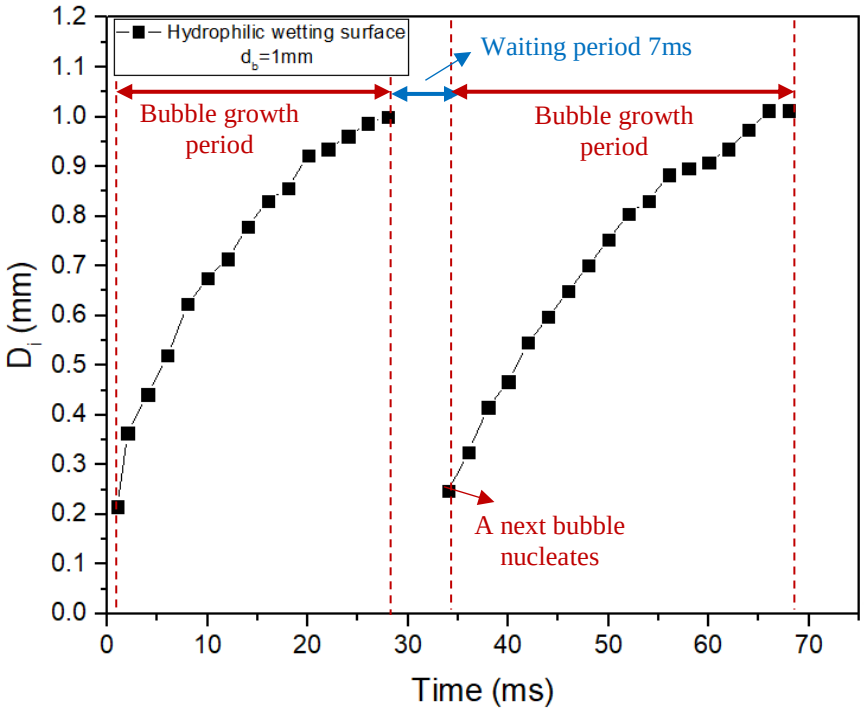

Figure 33 Instantaneous bubble diameter on hydrophilic surface at heat flux of 12.2 W/cm^2

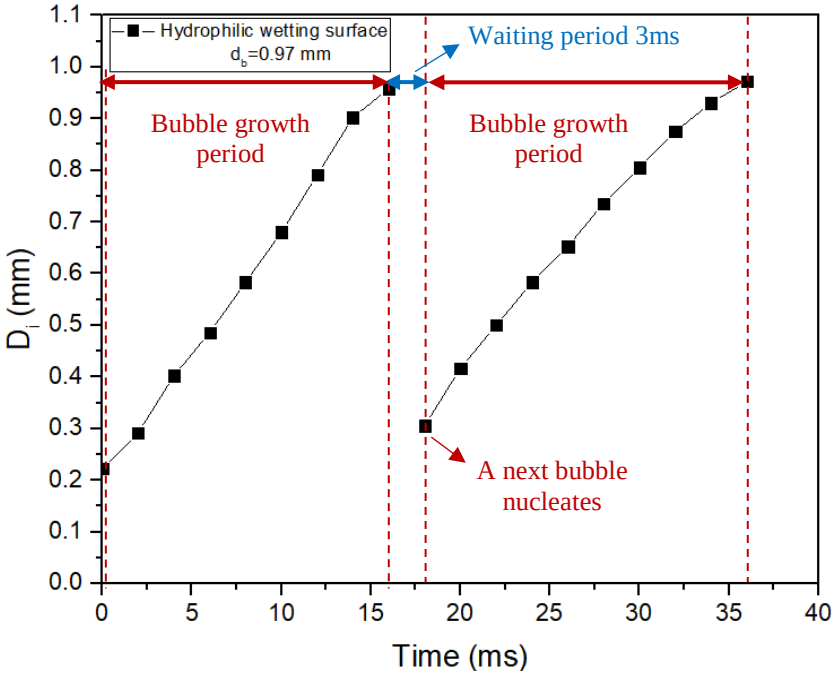

Figure 34 Instantaneous bubble diameter on hydrophilic surface at heat flux of 20.4 W/cm^2

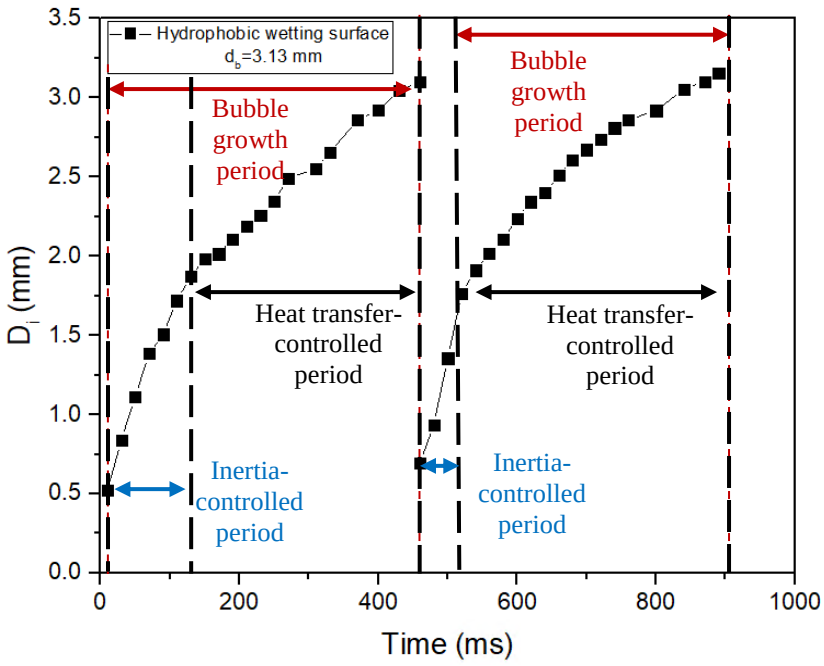

Figure 35 Instantaneous bubble diameter on hydrophobic surface at heat flux of 8.2 W/cm^2

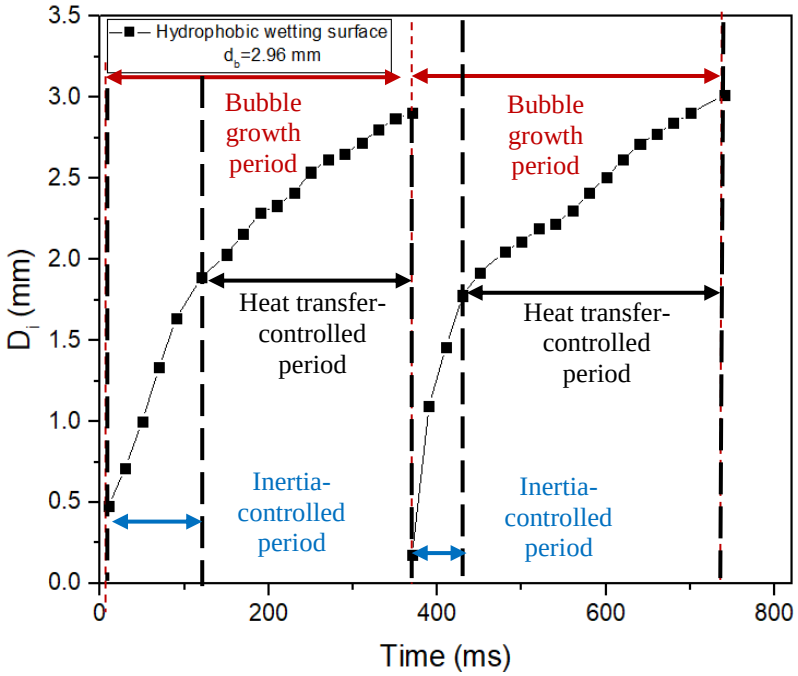

Figure 36 Instantaneous bubble diameter on hydrophobic surface at heat flux of 12.2 W/cm^2

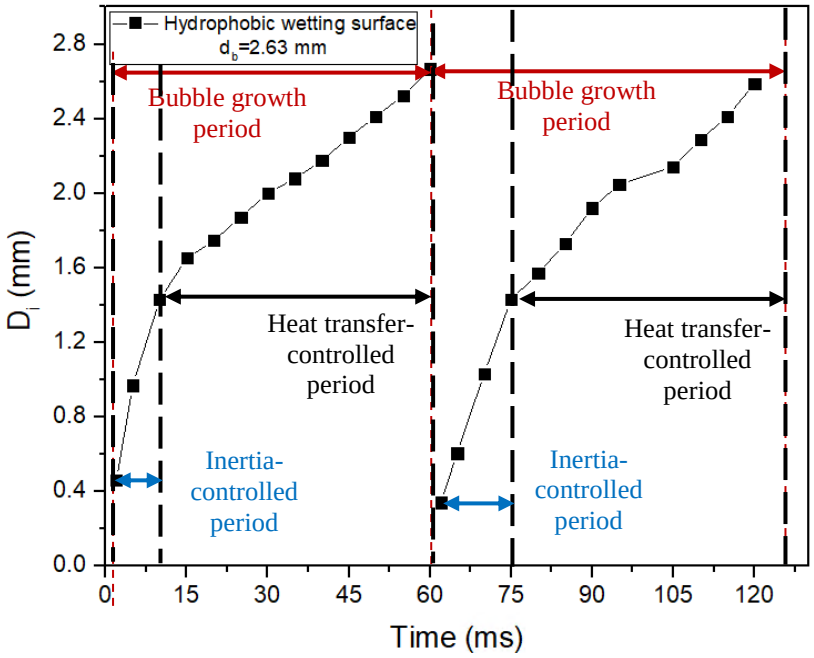

Figure 37 Instantaneous bubble diameter on hydrophobic surface at heat flux of 20.4 W/cm^2

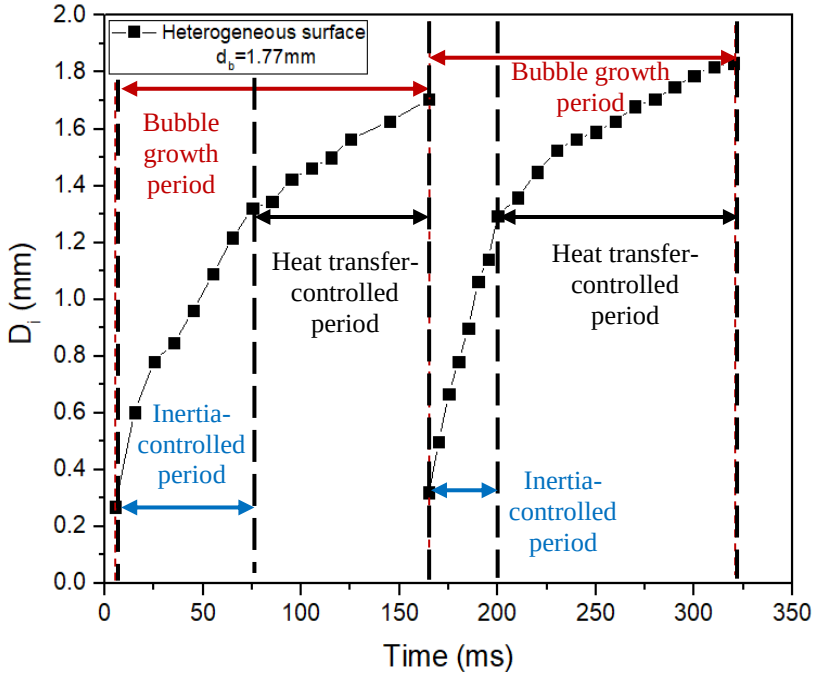

Figure 38 Instantaneous bubble diameter on Heterogeneous surface at heat flux of 8.2 W/cm^2

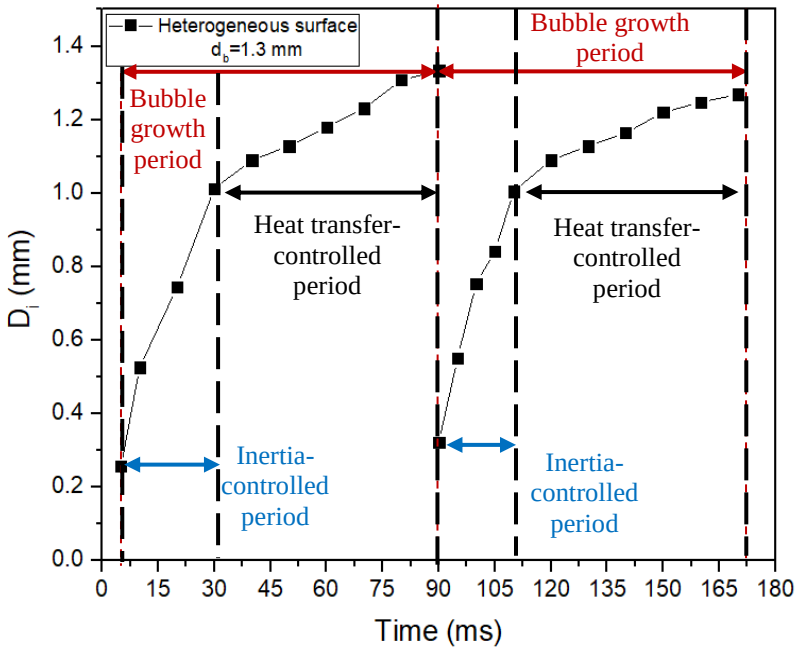

Figure 39 Instantaneous bubble diameter on Heterogeneous surface at heat flux of 12.2 W/cm^2

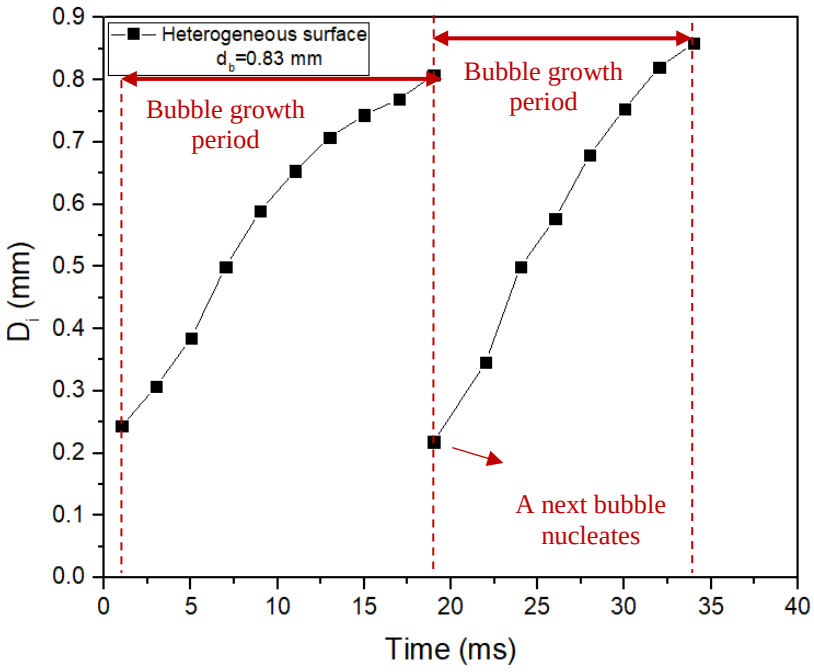

Figure 40 Instantaneous bubble diameter on Heterogeneous surface at heat flux of 20.4 W/cm^2

Figure 41, Figure 42 and Figure 43 show the comparison of the measured bubble departure frequency and corresponding measured bubble departure diameter with theoretical models of MCFadden & Grassman, Zuber, Cole and Fritz & Jakob. The experimental curves are closer to the predicted curve from McFadden and Grassmann's correlation than others. However, McFadden and Grassmann made an assumption that $f^2 D_d$ is linear with the acceleration of a departure bubble and analysis of waiting time is ignored to consider. Waiting time plays an important role in bubble emission frequency especially for hydrophilic surfaces. Therefore, a more complete study is needed.

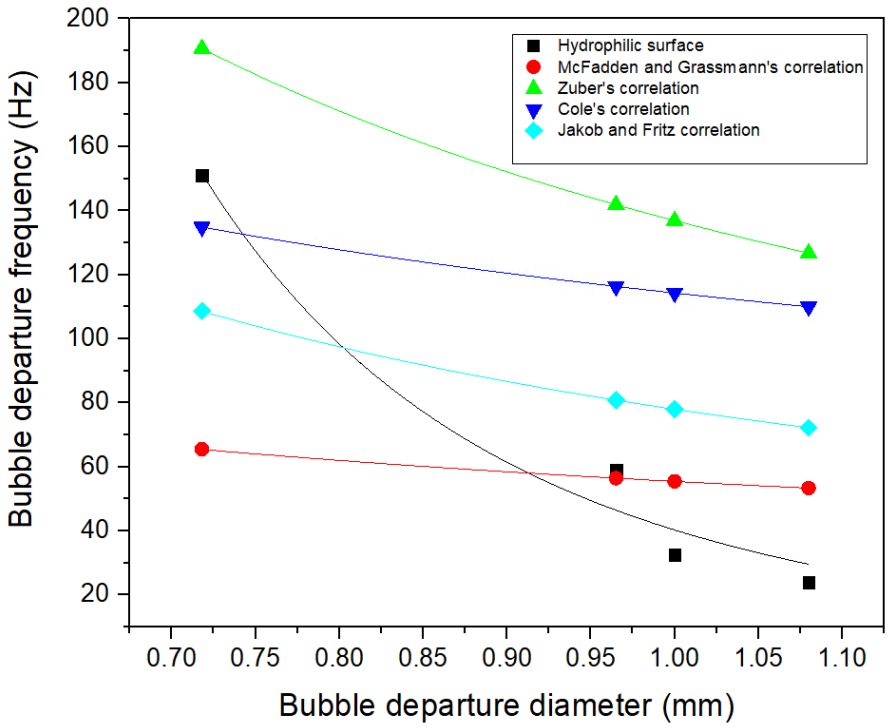

Figure 41 Measured bubble departure frequency vs measured bubble departure diameter for hydrophilic surface compared with theoretical models

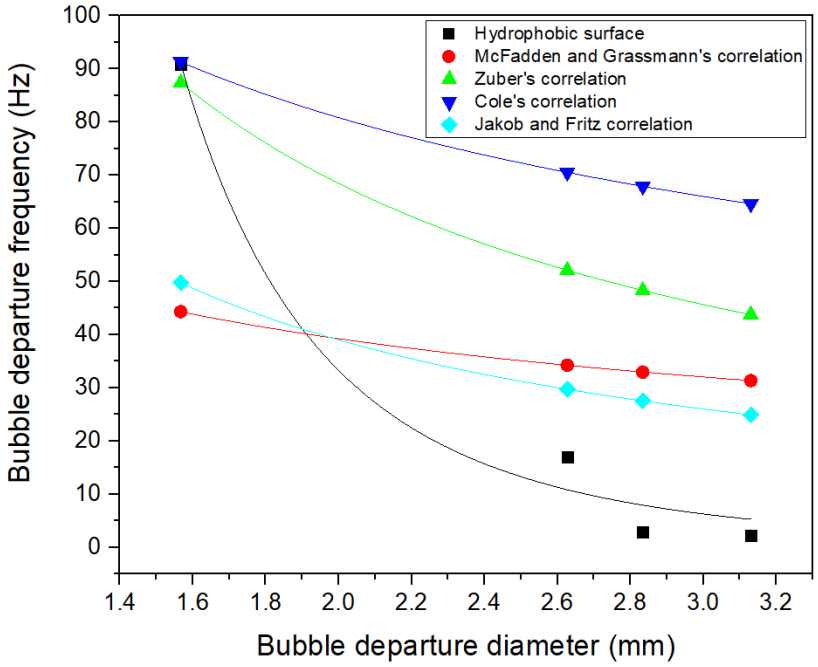

Figure 42 Measured bubble departure frequency vs measured bubble departure diameter for hydrophobic surface compared with theoretical models

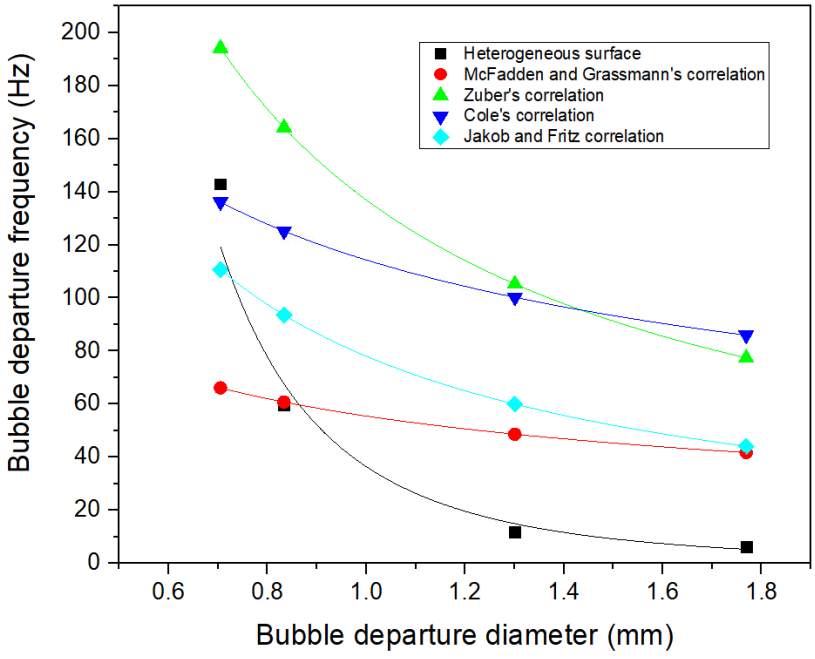

Figure 43 Measured bubble departure frequency vs measured bubble departure diameter for heterogenous surface compared with theoretical models

Figure 44 shows the relationship between bubble frequency and bubble departure diameter. The mean value of bubble departure diameter and bubble departure frequency were calculated by measuring at least 10 bubbles to ensure acurancy. In order to investigate the relationship between bubble departure diameter D_b and bubble emission frequencyf_d, many researchers have tried to use equation (28) to correlate them.

$$f_d \times D_d^n = \text{Constant} \tag{28}$$

Where n is an exponent depending on the different experimental condition[119]

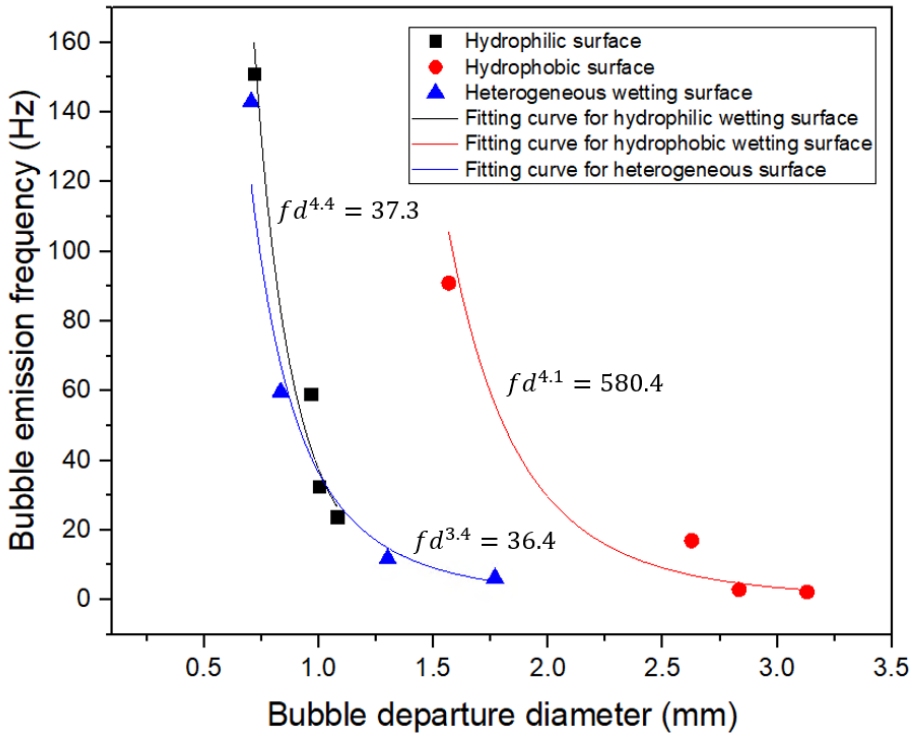

Figure 44 Average bubble departure diameter vs. bubble emission frequency

3.2.2 Enhanced pool boiling heat transfer on heterogeneous channel surface by modifying channel width

3.2.2.1 Nucleate boiling on channels with various width

The boiling curves for heterogeneous chips with various widths under saturated condition are presented in Figure 45. Four channel widths of 600 μm, 1000 μm, 2000 μm and 2500 μm were tested. The thermal performance trend shows that a chip with narrow channels has better performance than a chip with wider channels. As shown in Figure 46, maximum heat transfer coefficient of 110.3 kW/m^2K, 81.5 kW/m^2K, 79 kW/m^2K and 76 kW/m^2K were obtained for test chips with channel width of 600 μm, 1000 μm, 2000 μm, and 2500 μm, respectively. For all heterogeneous chips, bubbles mainly nucleated on the top surface of the fin with liquid replenishment inside the channel. Compared with heterogenous chips with different width of channels, the heat transfer enhancement is mainly attributed to the increase surface area, capillary-assisted suction ability and hydrophobic area percentage. It is obvious that the narrow channel chip has large actual surface area with which to provide more nucleation sites and heat transfer area. Based on the results from previous chapter, the heat transfer coefficient on the hydrophobic surface is higher than on the hydrophilic surface.

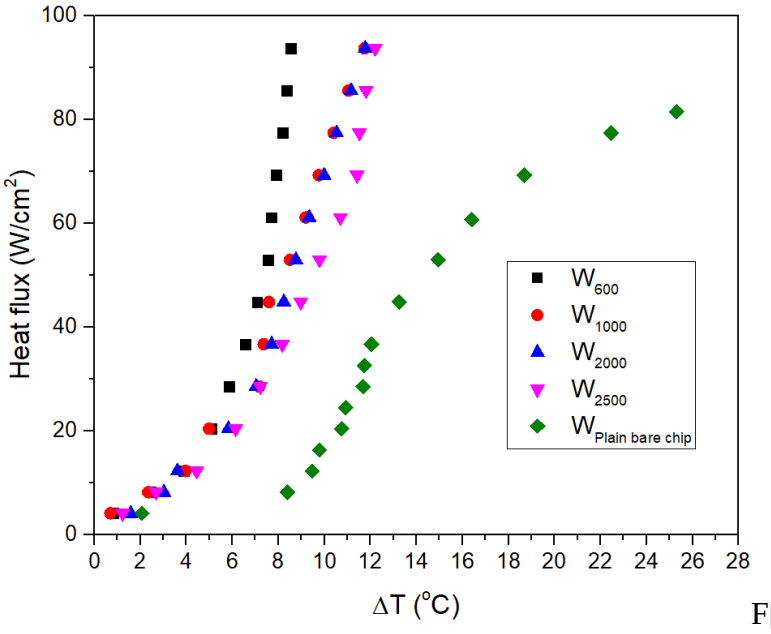

F[

Figure 45 Boiling curves on heterogenous wetting surface with various channel width

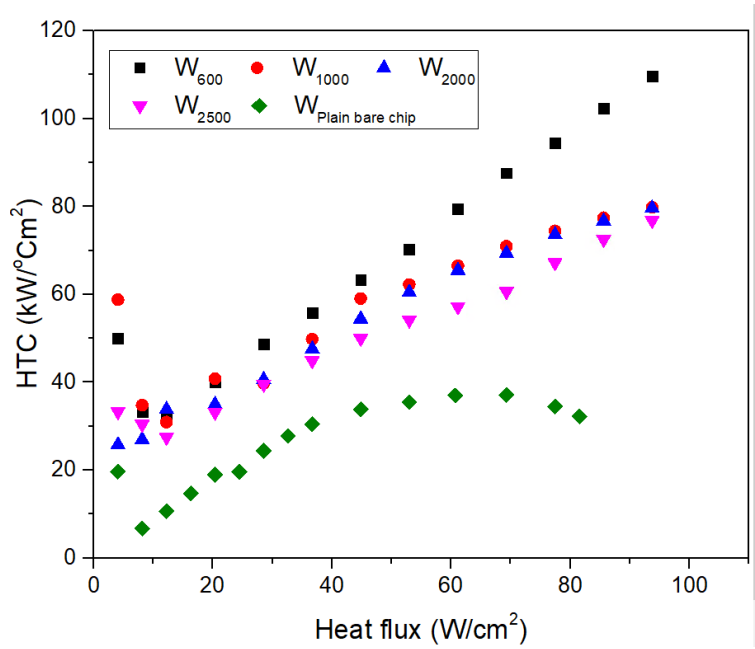

Figure 46 Boiling heat transfer coefficients on heterogenous wetting surface with various channel width

As Figure 47 has shown, a wider channel has a longer liquid supply pathway when liquid is unable to overcome the resistance of the sidewalls of channels to feed the nucleate sites. As for a narrow channel, after bubbles depart from the channels, liquid can quickly replenish from sidewalls or the surrounding of the channels to enhance heat transfer due to high capillary effect. In addition, the liquid entrance length of wider channel is larger than a narrower channels, which causes a decreased liquid flow velocity and slowing liquid flowing toward the fin tops. Therefore, the liquid replenishment is improved by narrow channels as the liquid can impinge on the base and feed the nucleate sites more quickly. Area enhancement is another factor. The surface with a narrow channel provides more nucleation sites and heat transfer area.

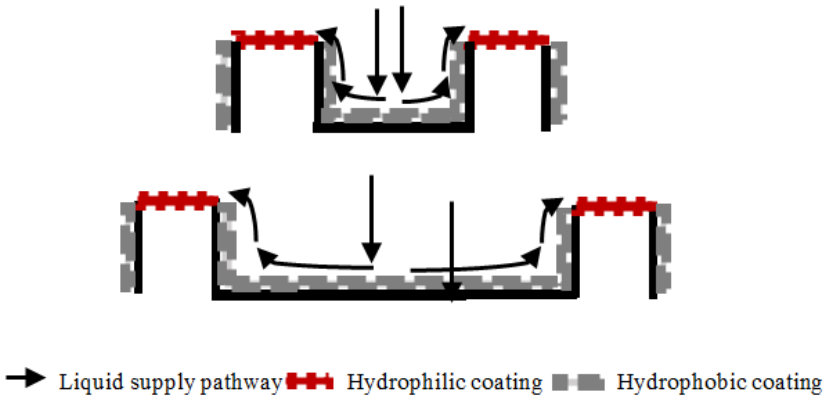

Figure 47 Liquid supply pathways inside narrow and wide channel

3.2.2.2 Forces analysis for a detaching bubble

As shown in equation (29), these individual forces act on a bubble before it departs from a surface. In this model, only vector of resultant forces acting on a bubble is considered in vertical direction.

$$F_d + F_s = F_b + F_p + F_i \tag{29}$$

In this equation, buoyancy force F_b, pressure difference forces F_p, and inertia force F_i act as detaching force whereas drag force F_d, and surface tension F_s impede bubble departure. Figure 49 shows the dynamic model of forces on growing bubble on a bare surface.

Inertial force resists a change in bubble growth velocity. It can be defined as

$$F_i = \frac{11}{6}\pi R^3 \rho_l \frac{d^2R}{dt^2} \tag{30}$$

In the nucleate boiling process, large inertial force acts on a bubble when it grows fast. However, it is negligible in the later detaching process due to slow growth. For example, bubble departing from a hydrophobic surface is governed by inertia force at the early stage. In the later detaching process with slow bubble growth rate, the inertia effect is diminished and the main governing factor is the heat transfer across the liquid vapour interface.

In the equations (31) and (32), surface tension force and drag force (negligible for inviscid liquid) increase with bubble base diameter

$$F_d = C_d \frac{\rho_l}{2}\left(\frac{dR}{dt}\right)^2 \frac{\pi D_b^2}{4} \tag{31}$$

$$F_s = \pi\sigma D_b sin\theta \tag{32}$$

where C_d is the resistance coefficient and θ is the contact angle. The base diameter is restricted by the channel width when the bubble grows inside the channel, which means that bubbles on the narrower channel width could receive

an addition force from wall of channel Kong X. et al[120] .Consequently, for the narrow channel, bubbles with small base diameter require low buoyancy force to depart from surface, leading to a reduced bubble departure diameter and bubble growth period, and improved heat and mass transfer processes. Kurose et.al[121] defined the reduced force in impeding bubbles departure as an additional force; contact pressure force F_{cp}, which contributes to the detaching resultant force. The modified model of forces acting on growing bubble inside a channel is depicted in Figure 49. Apart from the sufficient liquid provided from the hydrophilic area, the channel pressure is another force improving the bubble departure. This additional contact pressure force accounts for the pressure acting on the solid surface, which can be described as

$$F_{cp} = \frac{\pi d_w^2}{4}\frac{2\sigma}{R_r} \tag{33}$$

where R is the curvature radius. The value of curvature radius can be taken up to 5 times the radius of bubble. In consideration of channel pressureF_{cp}, the dynamic model of bubble departure can be modified as

$$F_d + F_s = F_b + F_p + F_i + F_{cp} \tag{34}$$

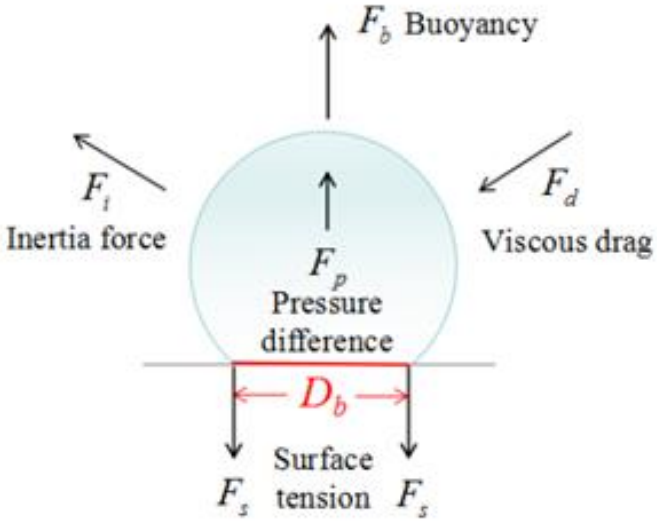

Figure 48 Forces acting on a growing vapour bubble on a bare surface [120]

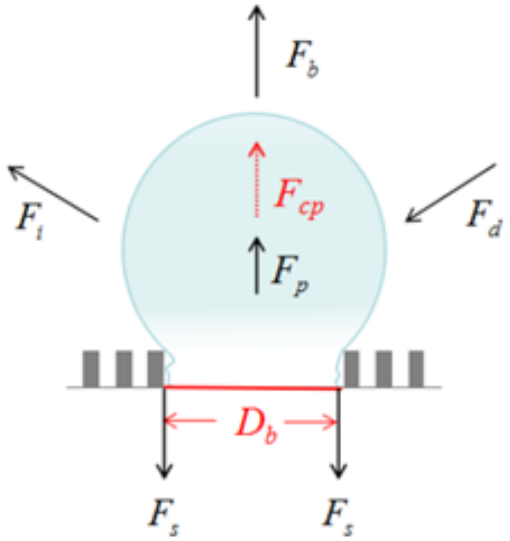

Figure 49 Forces acting on a growing vapour bubble inside channel

Experimental study of pool boiling heat transfer on novel bistructured surfaces based on micro-pin-finned structure [120]

3.2.2.3 Comparison of results in non-dimensional form

Bond number describes the relationship between surface tension and buoyancy force acting on a bubble. It is defined as the ratio hydraulic diameter d_h to capillary length Lc, as shown in equation (35).

$$\mathrm{Bo} = \left(\frac{\mathrm{d_h}}{\mathrm{L_c}}\right)^2 \tag{35}$$

Where L_c characterises the potential for bubble departure and coalescence and it is defined as,

$$\mathrm{L_c} = \sqrt{\frac{\sigma}{g(\rho_l - \rho_v)}} \tag{36}$$

For water, the capillary length Lc is 2.5mm. The range of the Bo number is between 0.24 (dp=600µm) and 1 (dp=2.5mm) in this experiment.

The calculated data collected helped to generalise the results in the form of an equation. This equation is defined as the dependence of the ratio between the selected surface heat transfer coefficient and the bare copper chip coefficient on the Bond number.

$$\frac{\mathrm{h}}{\mathrm{h_{bare}}} = f(Bo_d) \tag{37}$$

The relevant figure is presented in Figure 50. The boiling heat transfer coefficients were determined on the basis of the power law measurement data approximation. It is described in the form of heat transfer coefficient dependence for the heat flux:

For W_{600}:$h = 6.26q^{0.63}$

For $W_{1000:}$ $h = 9.03q^{0.48}$

For W_{2000}: $h = 9.01q^{0.47}$

For W_{2500}: $h = 7.4q^{0.51}$

For plain bare chip: $h = 1.67q^{0.78}$

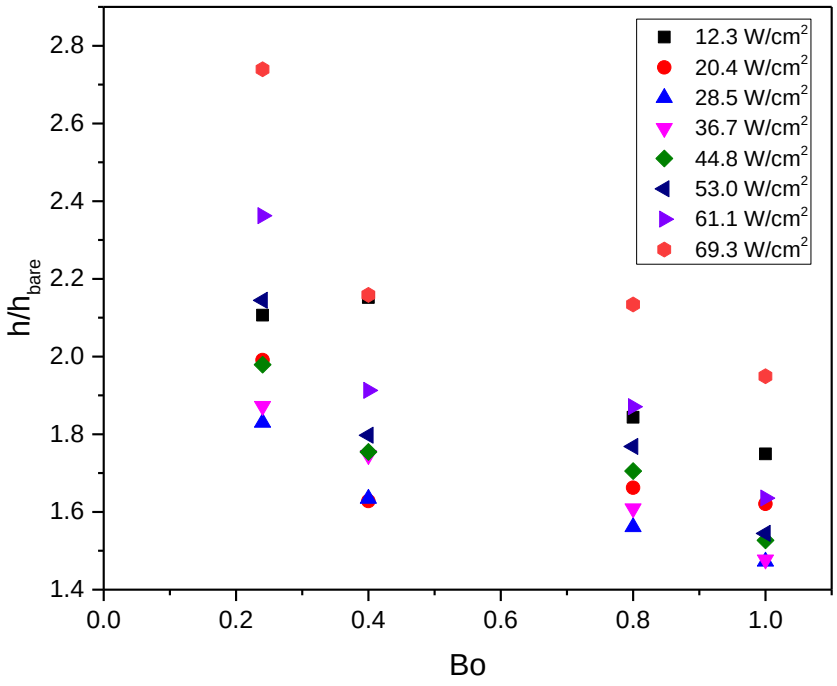

Figure 50 Relationship between heat transfer enhancement on Bond number

It is found that the highest heat transfer coefficients were obtained when Bo number is 0.24, which indicates that the optimum heat transfer improvements of heat transfer coefficient are obtained when the channel chip with width of 600 μm is used. The heat transfer coefficient improvement reduced as the Bo number increases from 0.24 to 1.

3.3 Summary

In this chapter, a systematic experimental study of pool boiling heat transfer was designed and conducted. The effect of wettability and channel width on pool

boiling heat transfer has been investigated. The mechanisms for boiling heat transfer enhancement were discussed. The results lead to the following conclusions:

1. The heterogeneous wetting surface with microchannels could improve boiling heat transfer by affecting bubble nucleation and bubble dynamics. The maximum heat transfer coefficient for heterogeneous wetting surface was 81.53 kW/m^2K at heat flux of 102 W/cm^2, which was higher than 77.4 kW/m^2K, 50.4 kW/m^2K and 32.2 kW/m^2K for hydrophobic, hydrophilic wetting surfaces and bare copper surface, respectively. A lower ΔT_{ONB} of 0.7 $^{\circ}C$ was obtained from both hydrophobic and heterogeneous surfaces compared with 6.1 $^{\circ}C$ for hydrophilic wetting surface and 8.2 $^{\circ}C$ for bare surface.
2. The observation of bubble growth and departure provided deep insights into synergistic effects of heterogeneous wettability and microstructure on pool boiling heat transfer enhancement. the top of fins were deposited with hydrophobic nanoparticles, which provide more nucleation sites, large bubble departure diameter, and short bubble waiting time. The inner channel surface coated with hydrophilic nanoparticles ensures sufficient liquid replenishment inside the channel and fast bubble emission.
3. In addition, it was found that highest heat transfer coefficient was obtained from the heterogeneous wetting surface with 600 μm of channel width. For a grown bubble, the width of channel may restrict bubble growth, which generates an addition upwards force to promote bubble departure. Also, the smaller channel width has the higher capillary

pumping ability to draw the liquid back to inside channel. Therefore, the narrower channel width presented better in pool boiling heat transfer than larger channel surfaces.

4. Study of thermal and thermo-mechanical performances of IGBT power electronics integrated with vapour chamber

In this study, a phase change cooling strategy is applied in IGBT power module. Vapour chamber with high thermal conductivity and good temperature uniformity replaces original copper substrate and is integrated with IGBT Power module. Thermal grease and additional cooling plate are removed, leading to significant reduction in thermal resistance. To evaluate the IGBT power module integrated with vapour chamber, a thermal test rig is built to analyse temperature distribution, junction temperature, temperature uniformity and thermal resistance. Furthermore, a coupled thermo-mechanical and a thermal fatigue models are built to evaluate thermal stress, energy dissipation density and lifetime.

4.1 Novel design of IGBT thermal management integrated with vapour chamber

Vapour chambers/heat pipes, as phase change cooling components, are a super heat conductive device and now represent an appealing option for efficiently cooling electric components. Vapour chamber is vacuum metallic container with wick structure lining the internal walls saturated with the working fluid. It utilises the cyclic phase change heat transfer process which can absorb much more heat than a single- phase heat transfer process does. Generally, the effective thermal conductivity of a vapour chamber is in range of 1,000 W/cm^2 to 50,000 W/cm^2 [6]. Figure 51 illustrates operational principle of a vapour chamber. In this case, when the heat is dissipated by the IGBT chips and diodes are applied to the vapour chamber, the working fluid will immediately be vaporised to fill the vacuum. Then, the vapour releases its latent heat of vaporisation and condenses when it contacts with a cooler wall surface. After that, condensed fluid returns to the heat sources due to capillary action in sintered copper wick structure lined inside wall, ready to be vaporized again and repeat the cycle. A such cyclic phase change heat transfer process makes the vapour chamber capable of being used in any orientation with respect to the gravity.

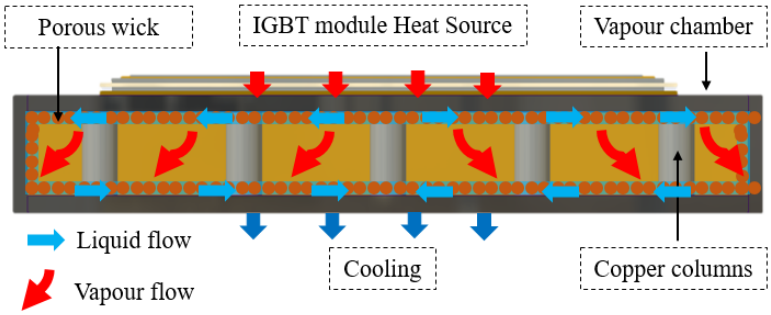

Figure 51 Schematic of working principal of vapour chamber

Table 13 lists parameters of vapour chamber heat sink in this study. The size of vapour chamber is compact and the same as the area of IGBT module. The most common envelope/wick and working fluid combinations are copper/water for electronics cooling. The wick structure is made up of copper foam with porosity of 69.8%. Filling weight of 4.1g was used for this study. 36 copper solid columns with diameter of 3 mm were used to prevent deformation. Figure 52 and Figure 53display the interior structure and wick structure.

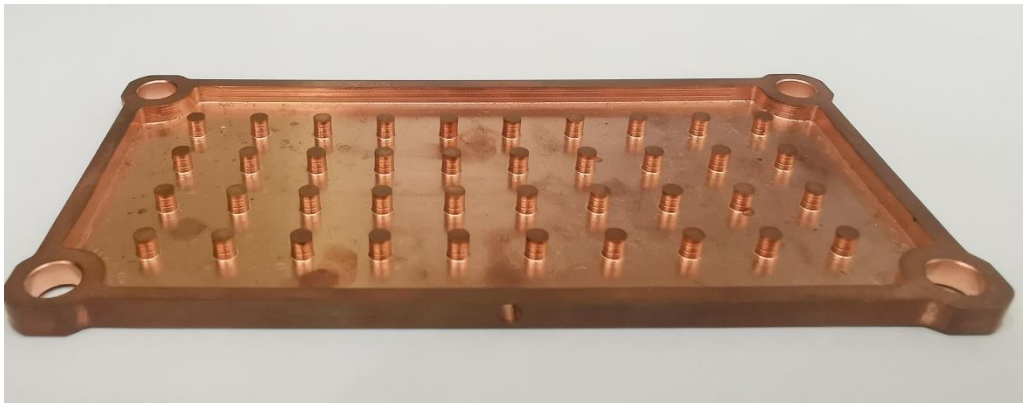

Figure 52 Interior structure of vapour chamber without wick structure

Figure 53 Copper foam wick of the vapour chamber

Typically, they operate below about 150℃, which is suitable for a semiconductor power module. Compared with the copper baseplate, the vapour chamber has a much higher thermal conductivity, more uniform temperature distribution, more durability, and lower weight. Moreover, the vapour chamber can be integrated with many kinds of heat sinks such as a pin-fin structure. Li et al. [122-124] did many researches to study the vapour chambers with respect to wick structures and ultra-thin flattened heat pipes. Avenas et al. [125] developed a power module with vapour chamber heat spread. With the same dimension, it is found that the thermal resistance of vapour chamber is 40% lower than that of an original plane silicon wafer. Ivanova et al. [126] proposed a heat pipe directly integrated in DCB for cooling of power semiconductor module packaging. As a result, it reduced the high heat flux to a lower and manageable level that the heat flux can be dissipated though a traditional cooling solution. Bose et al. [127] experimentally and numerically investigated the thermal performance of a vapour chamber for electronics cooling applications. The maximum temperature reduced by 26% and the mean deviation in temperature distribution decreased from 12.5% to 9% compared to a processor without a vapour chamber. Shwin-Chung Wong et al.[128] made a vapour chamber with parallel grooves and found that it has a low thermal resistance and large thermal limit under different orientations.

Table 13 Vapour chamber parameters

Parameter	Value
Vapour chamber size	122 mm×62mm×3 mm
Vapour chamber casing material	Copper
Vapour chamber working fluid	Water
Vapour chamber filling weight	4.1g
Type of wick structure	Copper foam
Porosity of wick structure	69.8%

Figure 54 shows the cross sections of three different thermal management structures designed for cooling an IGBT semiconductor power module. Figure 2a represents the conventional indirect cooling solution. An IGBT module with a copper baseplate is bolted to a heat sink using thermal grease based thermal interface material (TIM). The TIM layer contributes the most to the contributors to total thermal resistance. Figure 55 shows the thermal resistance of each part and the overall IGBT power module.

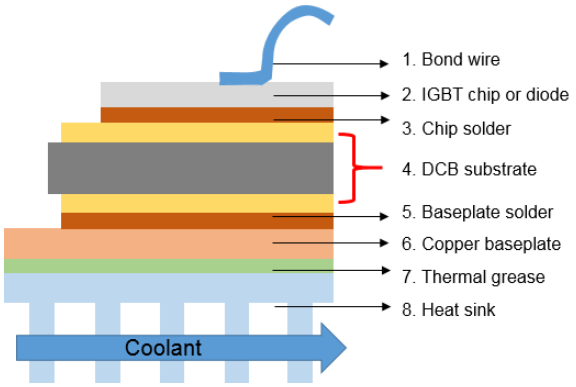

2a

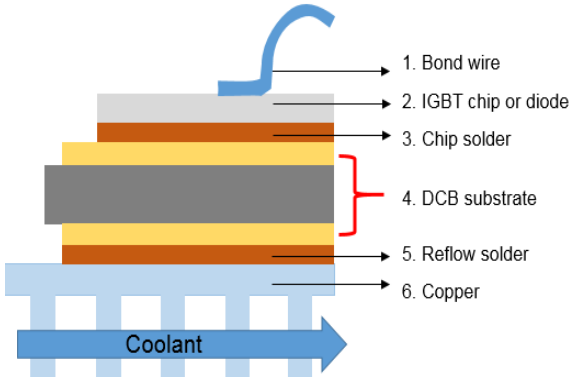

2b

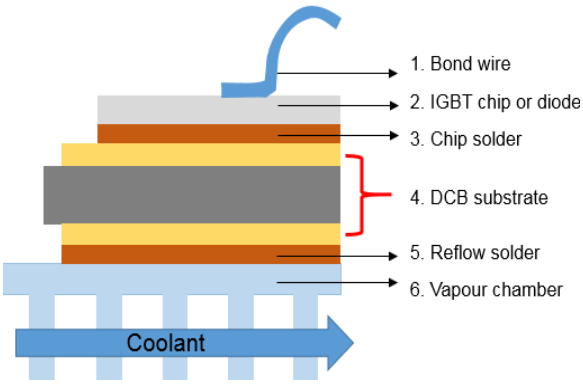

2c

Figure 54 Structure of IGBT (a) Case A: with traditional indirect cooling (b) Case B: with direct cooling attached with copper baseplate IGBT module (c) Case C: with direct cooling attached with vapour chamber baseplate

A comparison of overall thermal resistance of IGBT power modules are shown in Figure 55. It is obvious that the direct cooling structures don't have thermal grease and the additional heat sink. The thermal resistance of Fig. 2b shows the cross section of an assembly using direct attach method. DCB layer is directly soldered on a copper baseplate. Currently, this direct cooling of power semiconductor module is most- adopted due to its compact structure. thermal grease and additional aluminium heat sink account for 25.8 % of overall thermal resistance of case A, so they are removed in case C. To further reduce the thermal resistance, the copper baseplate is replaced by a vapour chamber which is integrated with the substrate as shown in Fig. 2c. The overall thermal resistance can be reduced by 32.2% comparing to the structure of case A.

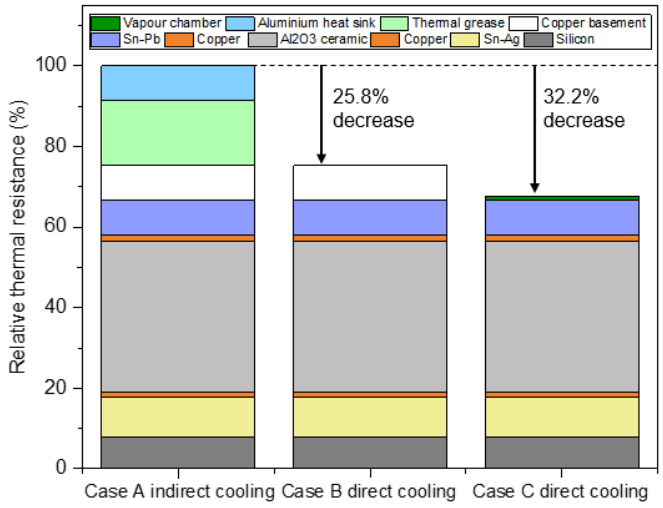

Figure 55 Comparison in thermal resistance between convectional structures and novel structure

4.2 Methodology

Based on the structure of case 2b and case 2c, a coupling thermo-mechanical model and a thermal fatigue model were established with finite element method to investigate the failure mechanism of solder layer under power cycling and

estimate lifetime. Also, an experimental test rig was built to test thermal performances of vapour chamber direct cooling and conventional copper direct cooling of an IGBT power module at different operating power loss conditions. The experiment mainly investigated the temperature field and thermal resistance. These results were compared with the results obtained from the thermal model.

4.2.1 Finite element method (FEM) model to analyse thermo-mechanical performance and thermal fatigue

4.2.1.1 Module description

A schematic of the IGBT power module is given by Figure 56. The module is composed of six pairs of IGBT chip and diode, direct Copper Bond (DCB), solder, copper, or vapour chamber. The DBC layer is made of two copper layers bonded on an aluminium oxidation Al_2O_3 layer. The Al_2O_3 functions as heat conductor and electrical insulator due to its good thermal conductivity and electrical insulation. The chip solder has the same size with that of IGBT chips and diodes. Table 14 shows the material physical properties of each layers and Table 14 summarises sizes of main components.

Figure 56 Schematic of the analysed power module

Table 14 IGBT component sizes

Component	Dimensions
Silicon chips	9.718mm×3.342mm×0.02mm
Silicon diode	11.146mm×7.746mm×0.02mm
DCB copper layer	47.14mm×44.35mm×0.3mm
DCB Aluminium oxidation	48.74mm×46.48mm×0.635mm

Table 15 Material thermal property

	Thermal capacity J/kgK	Thermal conductivity W/mK	Coefficient of thermal expansion 10^{-6}/K
Al_2O_3	730	35	6.5
Cu	320	413	17
Vapour	385	5000	17
Al	904	237	23.1
Silicon	678	71	2.1
Sn-3.5Ag	240	52	25
Sn-Pb	242	57	19

4.2.1.2 Thermal and thermo-mechanical models

Finite element simulations have been used extensively to investigate solder thermal performance and the reliability. The main challenge for the electronic packaging industry is to predict the solder fatigue life. In a power cycle simulation, energy-based and strain-based approaches are widely applied, and strain range and energy density are used as the failure parameters, and the energy-based model uses energy density to investigate crack initiation and propagation through solder from fracture mechanics approach.

The FEM simulation method was used to simulate the conjugate heat transfer, thermo-mechanical behaviours and fatigue of IGBT power module. The electro-thermal modelling includes a calculated power loss, which mimics the one heating up each component in a real case. With this strategy, it is possible to identify the potential hot spots, maximum junction temperature, and temperature gradient on the IGBT power module. The thermal simulation was validated against analytical results and compared with experiment results. In thermal modelling, the diffusion-convection governing energy equation is used to solve temperature field problem as expressed in equation (38). This equation neglects mass transport part.

$$\rho C_p \frac{\partial T}{\partial t} - \nabla(k\nabla T) = q_s \tag{38}$$

where ρ, C_p k and q_s are the density kg/m^3, heat capacity J/K, thermal conductivity W/mK and volumetric heat generation W/m^{-3} respectively. In the thermal boundary setup, the convective heat transfer coefficient of a water heat sink which cools the bottom of baseplate are set as 800 W/m^{2}K and 1200 W/m^{2}K, according to copper baseplate case and VC baseplate case based on our experimental data.

In solid mechanical modelling, the thermo-mechanical performance depends heavily on the electro-thermal parameters, plastic and creep properties, coefficient of thermal expansion, yield strength. Equation (39) is the Hooke's law, where σ is stress tensor, ε is strain tensor, C is the fourth order elasticity tensor and ":" stands for the double-dot tensor product[129].

$$\sigma - \sigma_0 = C: (\varepsilon - \varepsilon_0 - \alpha\theta) \tag{39}$$

Semiconductor silicon and aluminium oxide in the DCB substrate were assumed to be a linear-elastic material. Copper was assumed to be also elastic plastic because the stress within the DCB substrate easily exceeds its yield stress. The Sn-3.5Ag solder layer was assume to be viscoplastic with properties of hardening plasticity and implicit creep as it is widely agreed that the rate of dependent plasticity creep occurs in the solder over time[130]. In order to exhibit such effect, Garofalo hyperbolic sine law was applied to the solder layer.

$$\frac{d\varepsilon_C}{dt} = A(\sinh B\sigma)^n e^{(-\frac{\Delta Q}{RT})} \tag{40}$$

The ε^{cr} is the equivalent uniaxial creep strain, σ is the equivalent tensile stress, T is absolute temperature, R_g is the gas constant; A, B, n, ΔQ are creep rate coefficient, 1/effective stress, Garofalo n parameter and activation energy respectively[131].

Also, the creep analysis applies an implicit time integration method which includes temperature-dependent constants together with modelling of creep and kinematics hardening plasticity. In this case, the total strain can be expressed as equation:

$$\varepsilon_{in} = \varepsilon_{el} + \varepsilon_p + \varepsilon_{cr} \tag{41}$$

$$\varepsilon_p = \lambda \frac{\partial q}{\partial s} \tag{42}$$

Kinematics hardening plastics model is given in equation (43) and (44):

$$\sigma_{ys} = \sigma_{ys0} \tag{43}$$

$$\sigma_{Shift} = \frac{E_{Tkin}}{1 - \frac{E_{Tkin}}{E}} \left(\frac{2}{3} \varepsilon_p \right) \tag{44}$$

E_{Tkin} is kinematic tangent modulus. Both kinematic and mixed hardening result in a so-called back stress or shift stress, which is a new stress level that is equally far from yielding in tension and compression.

Mechanical properties of packaging material and chip solder material are listed in Table 16.

Table 16 Viscoplastic properties of Sn-Ag solder

A(1/s)	B(MPa)	n	ΔQ(J/mol)	R(J/molK)	$\mathbf{E_{Tkin}}$(MPa)
44100	0.005	4.2	44995	8.314	4.9×10^{9}

The thermal fatigue lifetime modules for prediction of lifetime of solder include stress, strain, energy, and damaged based models. Energy-based models are the most convenient and accurate method due to the ability to obtain test conditions more precisely[132, 133]. Therefore, the energy-based model and Morrow model are used to address the lifetime of Sn-3.5Ag solder layer under power cycle in this study. Fatigue damage parameters such as inelastic strain and inelastic strain energy density and energy-based model are expressed as follow.

$$\Delta W_{in} = \Delta W_{pl} + \Delta W_{cr} \tag{45}$$

$$\Delta W_{in} = W'(2N_f)^m \tag{46}$$

ΔW_{in}, ΔW_{pl} and ΔW_c are inelastic, plastic and creep strain energy density respectively. ε_{in}, ε_{pl} and ε_{cr} are inelastic, plastic and creep strain respectively. W_f' is fatigue energy coefficient, N_f is fatigue cycles and m is fatigue energy exponent with value of -0.69.

4.2.1.3 Boundary condition

The simulation is conducted by Comsol Multiphysics software [22]. It is found that the simulation results of temperature distribution remain almost unchanged after the density exceeds 222,646. Therefore, mesh with an element count of 222,646 is selected for this study. Figure 57 shows the detail of final mesh of the module. The size of mesh ranged between 2 mm and 0.5 mm. Thin and weak components such as solder layers, chips and DBC are finely meshed whereas the baseplate are coarsely meshed.

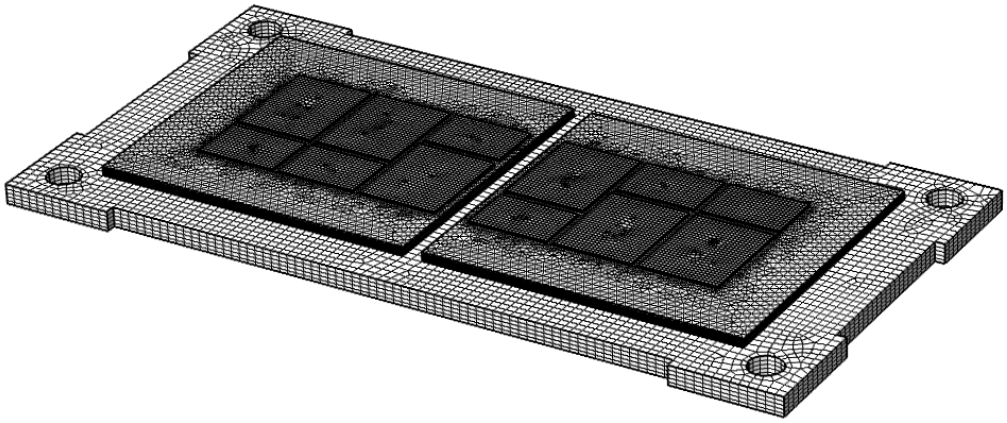

Figure 57 Finite element mesh of the module

In this thermal-mechanical coupling model, heat sources are generated from IGBTs and FRD (fast-recovery diodes), which are estimated by power loss of these two components. The power applied to the IGBT chips and diodes was 97.83W (high state) and 25.17W (low state) per power cycle. As suggested by Z. Xu[134] IGBT cycle is six times longer than diode power cycle in hybrid

electrical vehicle applications. Figure 58 shows power cycle applied to the IGBT module. Also, convection heat transfer was considered in this model. The ambient temperature is initially set to 20℃ and natural convection heat transfer coefficient of air is 5 W/m^2K. To analyse thermal performance of each module, the heat transfer coefficient of cooling solutions is set to 1000 W/m^2K based on the experiment. Table 17 summarises basic thermal parameters used in modelling. Solid mechanics are applied to the model to evaluate displacement caused by thermal expansion and thermal stress. Only the copper base plate of IGBT module and four bolt holes were fixed in all directions while others displace freely.

Table 17 Boundary condition in IGBT modelling

Initial module temperature	20℃
Heat source from diode	26.17 W/per diode
Heat source from IGBT	96.83 W/per IGBT
Air temperature	20℃
Coolant temperature	75℃
Heat transfer coefficient of air	5 W/m^2K

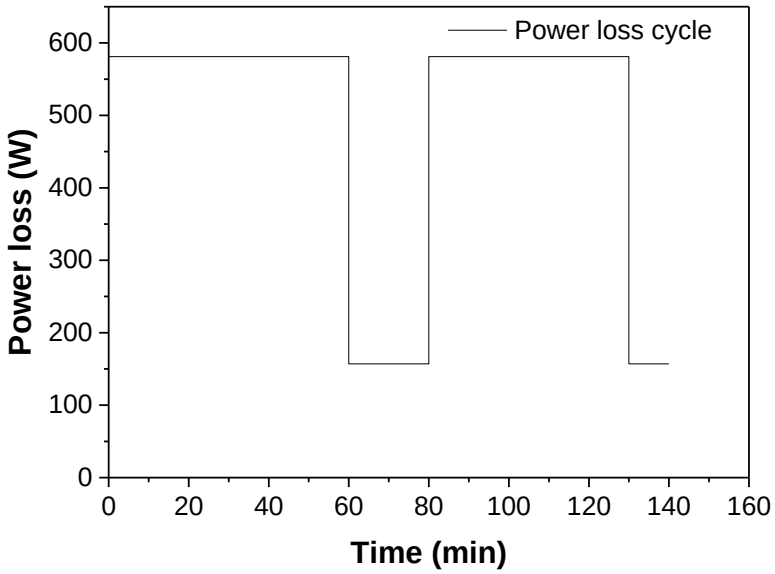

Figure 58 IGBT power loss cycle

4.2.2 Experimental study of thermal performance of direct phase change cooling of vapour chamber integrated with IGBT power module.

4.2.2.1 Fabrication process of an IGBT with vapour chamber

Figure 59 shows the manufacturing process of the IGBT power module integrated with a vapour chamber. After finishing the IGBT/diodes soldering on substrate and wiring bonding process, the substrate is soldered onto the VC baseplate by using a reflow soldering. At this stage, the working fluid is not injected into VC since high temperature can lead to vaporisation of working fluid and large deformation of VC during the solder process. After soldering process, water is injected through a tube and then the chamber is vacuumed. Next, non-condensable gases are removed by heating the VC. At last, the tube is removed and sealed. Figure 60 shows the prototype of IGBT integrated with vapour chamber.

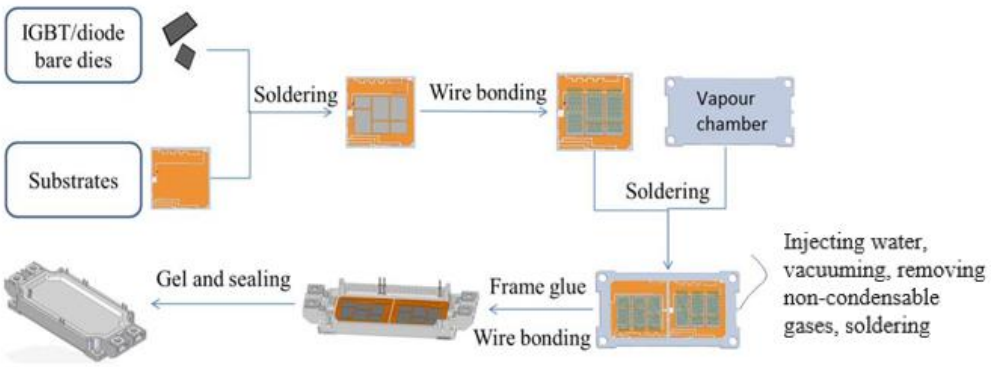

Figure 59 Fabrication process of IGBT semiconductor integrated with VC

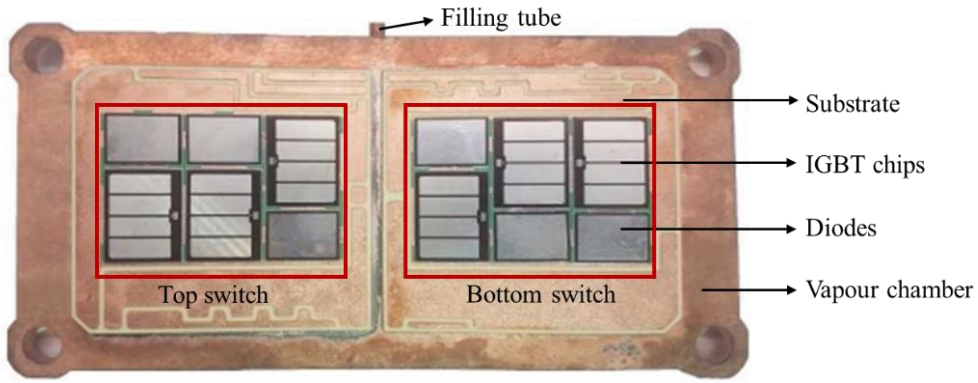

Figure 60 Schematic of the analysed power module prototype

4.2.2.2 Power loss calculation

When a semiconductor device such as an IGBT or a diode operates, there exist three categories of power losses as shown in equation (47). The first one is the conduction loss which consists of the heat dissipation from IGBT P_{SS} and diode P_{DC}. The second one is the switching losses P_{SW} caused by the energy lost when the device is switching ON or OFF. The third one is named recovery loss of diodes P_{rec} and regards the losses when the device is fully OFF.

$$P = P_{SS} + P_{SW} + P_{DC} + P_{rr} \tag{47}$$

where conduction losses from IGBT PSS and diode P_{DC} are defined, respectively, as

$$\mathrm{P_{SS}} = I_{CP} \times V_{CE(SAT)} \times \left(\frac{1}{8} + \frac{D}{3\pi} cos\varphi\right) \tag{48}$$

And

$$\mathrm{P_{DC}} = I_{CP} \times V_f \times (\frac{1}{8} - \frac{D}{3\pi} cos\varphi) \tag{49}$$

where I_{CP}, $V_{CE(SAT)}$, D, $cos\varphi$, V_f are peak value of output current, forward voltage drop in IGBT, duty ratio, power factor, forward voltage drop in the diode.

Switching losses $\mathrm{P_{SW}}$ of each IGBT typically contribute massively to the total system losses. It can be described as

$$\mathrm{P_{SW}} = (E_{SW(ON)} + E_{SW(OFF)}) \times \frac{f_s}{\pi} \tag{50}$$

where $E_{SW(ON)}, E_{SW(OFF)}$ is the switching on loss of IGBT and switching off loss of IGBT, f_s is the switching frequency.

During the switching from the conduction to block state, a diode stored charge which must be discharged. The power loss in this stage is called recovery loss of diodes $\mathrm{P_{rec}}$ described by equation (51).

$$\mathrm{P_{rec}} = E_{rec} \times \frac{f_s}{\pi} \tag{51}$$

where E_{rec} is the recovery loss of diode.

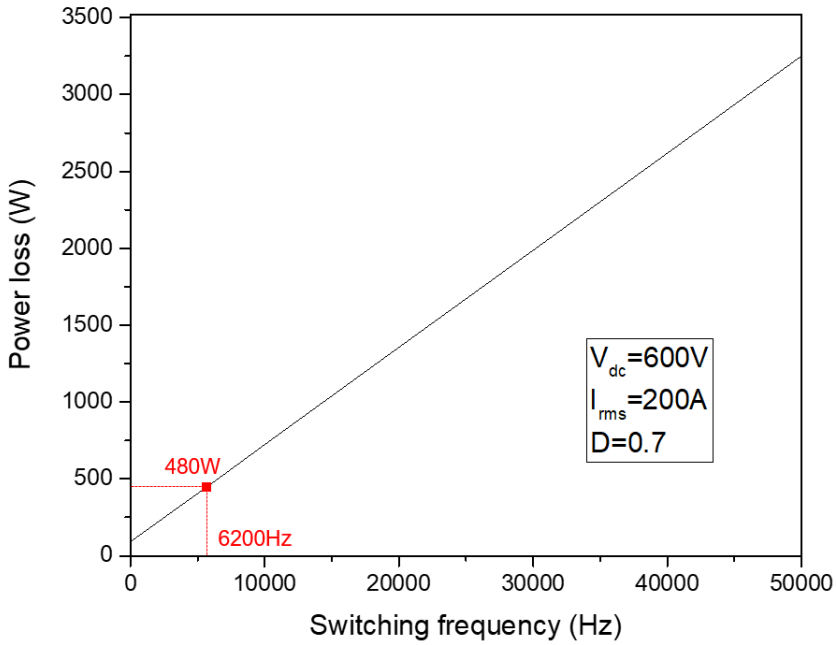

Figure 61 Power loss versus switching frequency for the IGBT module

Figure 61 demonstrates the IGBT heat generated by the power loss in terms of switching frequency with consideration of the turn-on and turn-off curves. In this study, we focus on the operation condition at frequency of 6200 Hz. Therefore, based on the calculation, power loss applied to each IGBT chip and diode was 61 W (high state) and 19 W (low state) per cycle at switch frequency of 6200 Hz. As shown in Figure 62, the top switch and bottom switch operate alternatively. At the top switch power loss stage, three top switch IGBTs and diodes firstly start to work and dissipate 183 W heat in total during 0 μs -56 μs, and then top diode generates totally 57 W during 56 μs-80 μs.

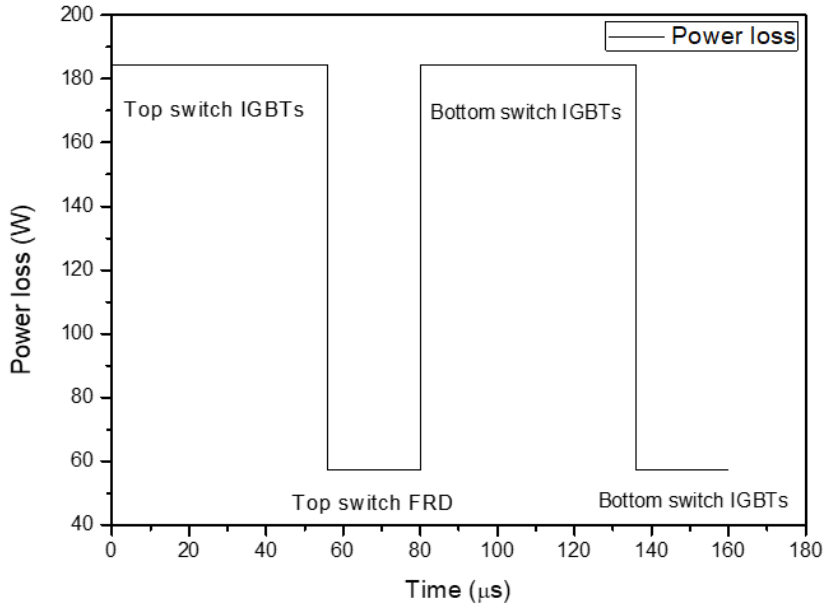

Figure 62 IGBT power loss in one cycle

4.2.2.3 Experiment setup

An experimental apparatus is built to investigate the thermal behaviour of the IGBT semiconductor module with both copper and vapour chamber baseplates, which are evaluated by the junction temperature and thermal resistance of the IGBT semiconductor module. The junction temperature is a very important factor for monitoring the reliability of the power module, and the latter is a good indicator for evaluating the cooling capacity of the cooling device. Figure 63 and Figure 64 display the entire schematic diagram of the experiment apparatus and the structure of the IGBT semiconductor module integrated with the vapour chamber.

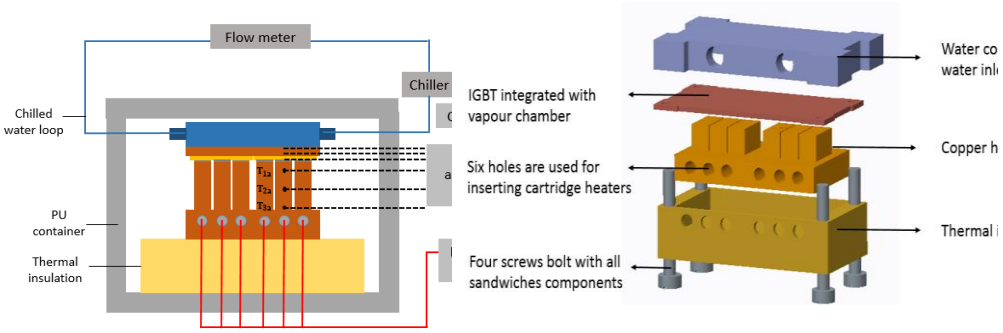

(a) (b)

Figure 63 (a) Schematic diagram of the experiment apparatus (b) Schematic diagram of the IGBT power model with the heat sink and heat source

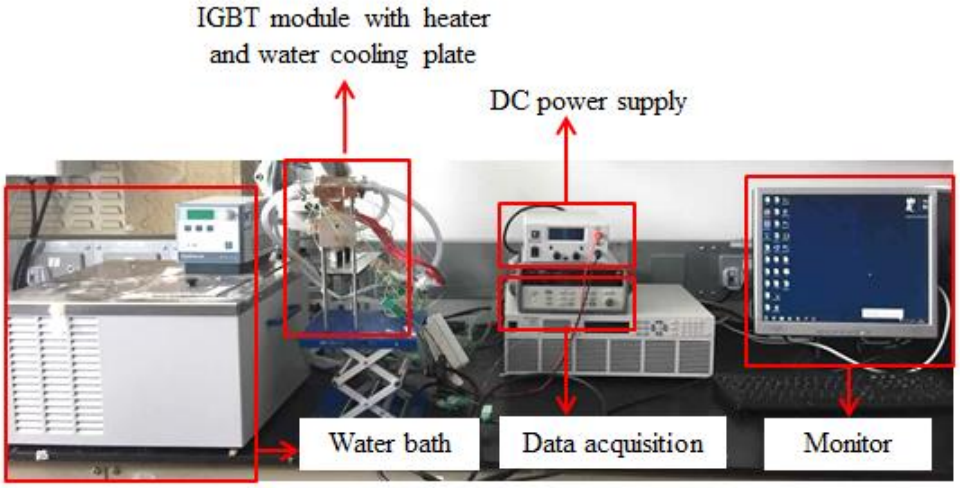

Figure 64 Experimental apparatus of IGBT module

The vapour chamber is directly soldered on a DCB substrate using Sn-Pb solder material and then it is bolted to a water-cooled plate. A constant heat load is directly given to each diode and IGBT chip by the copper heating blocks containing six cartridge heaters (RS PRO). The effective heating areas are the same as those of IGBT chips and diodes. The IGBT chips and diodes are directly attached to the copper heating block, and the whole module is sandwiched between heating block and copper water cooling plate installations. A heat

power with range of 30 W to 240 W is fed into the 6 cartridge heaters equally by increments of 30 W. A chiller (Polyscience) continuously generates cold water with temperature of 20 °C and the water flow rate is set to 40 L/h. A thermal grease, TIG780-38 (thermal conductivity 3.8 W/mK) is used between the heater and the IGBT chips and diodes to minimise the thermal contact loss. Type-T thermocouples are used to measure the temperature of the water inlet, outlet, and IGBT semiconductor module as shown in Figure 65. The uncertainty of temperature measured by the thermocouples is ±0.1 °C. A mineral wool insulation with thermal conductivity of 0.044 W/mK covers the whole test section and the test rig is placed in a polyurethane enclosed container whose thermal conductivity is 0.02 W/mK to reduce thermal loss.

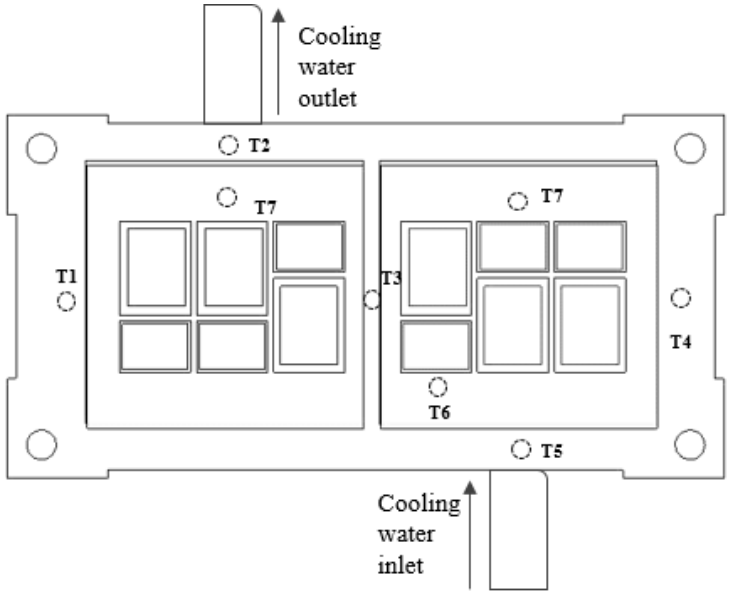

(a)

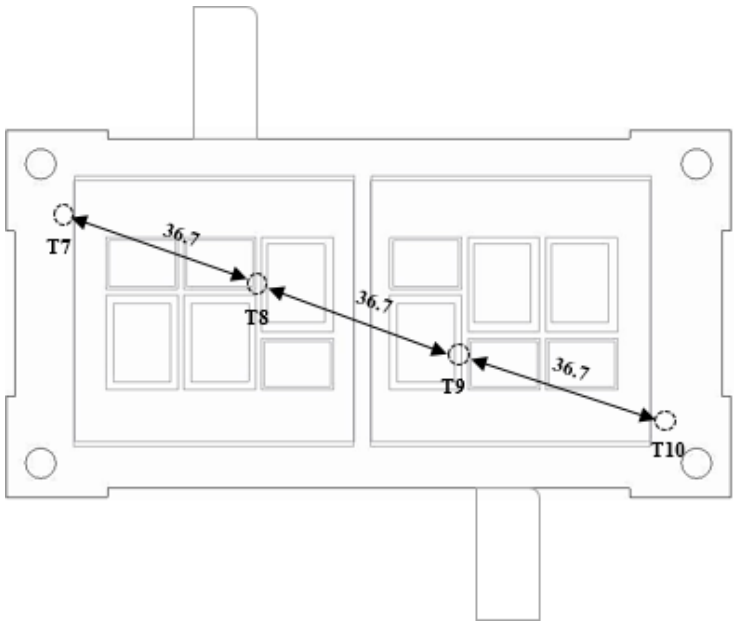

(b)

Figure 65 Position of the thermocouple on (a) top and (b) bottom surface

4.2.2.4 Data acquisition and uncertainty analysis

In this study, we managed to measure thermal resistance of the vapour chamber and the whole IGBT semiconductor module integrated with the vapour chamber module. One-dimensional resistance, R_{VP} is derived by

$$R_{VC} = \frac{\overline{T_t} - \overline{T_b}}{Q} = \frac{\frac{1}{5}\sum_1^5 T_i - \frac{1}{4}\sum_7^{10} T_i}{Q} \quad (52)$$

where $\overline{T_h}$ is the average bulk temperature of heater, $\overline{T_b}$ and $\overline{T_t}$ are average temperatures of bottom evaporator surface and condenser top surface of vapour chamber respectively, and q is the heat transfer rate through copper heater surface. Those average temperatures were the arithmetic means of the results of the related probes after the system achieved the steady state.

Figure 66 shows the thermal resistances of IGBT semiconductor module with vapour chamber thermal management system in the heat path from junction to ambient. The total thermal resistance between chip and cooling media $R_{th(j\text{-}a)}$ is the total thermal resistance, which includes thermal resistance between chip and baseplate$R_{th(j-c)}$, and heat sink and cooling media $R_{th(c-a)}$, which is expressed as

$$R_{th(j-a)} = R_{th(j-b)} + R_{th(b-a)} \quad (53)$$

$$R_{th(j-b)=} \frac{\overline{T_j} - \overline{T_b}}{Q} = \frac{T_6 - \frac{1}{4}\sum_7^{10} T_i}{Q} \quad (54)$$

$$R_{th(b-a)=} \frac{\overline{T_b} - \overline{T_a}}{Q} = \frac{\frac{1}{4}\sum_7^{10} T_i - T_{inlet}}{Q} \quad (55)$$

where T_a and T_j represent cooling media temperature and junction temperature respectively. It is impractical to directly measure the junction temperature T_j of the semiconductor module[135]. In this study, the thermocouple was placed as close as possible to the IGBT chip to measure the junction temperature.

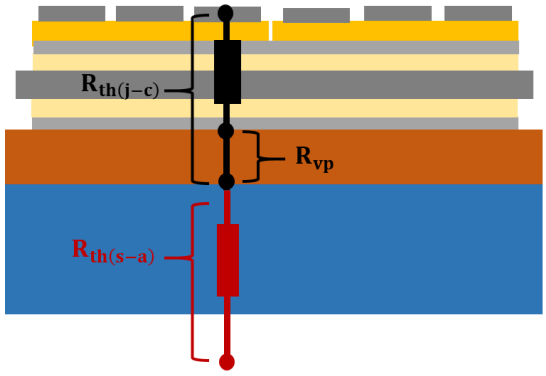

Figure 66 Fractions of calculated thermal resistance in the IGBT semiconductor module integrated with vapour chamber

The uncertainty analysis of thermal resistance is carried out by using method proposed by Kline and McClintock [107] as shown below

$$\mathrm{U_R} = f(U, I, T) \tag{56}$$

$$\frac{\Delta \mathrm{R_{j-a}}}{\mathrm{R}} = \sqrt{\left(\frac{\Delta \mathrm{U}}{\mathrm{U}}\right)^2 + \left(\frac{\Delta \mathrm{I}}{\mathrm{I}}\right)^2 \left(\frac{\Delta \mathrm{T}}{\mathrm{T}}\right)^2} \tag{57}$$

where U_q and $U_{\Delta T}$ represent uncertainties of the heat transfer rate and the difference of temperature respectively. The uncertainty of this experiment was 6.8%.

4.3 Results and discussion

4.3.1 Junction temperature

The junction temperature is the crucial factor which affects the reliability of IGBT semiconductor significantly. As shown in Figure 67, the temperature distributions of IGBT integrated with copper and VC are obtained by simulations. The results are same in the stages of top and bottom switch power

loss, therefore, only the results in the stage of top switch power loss are presented here. Hot spots mainly locate on IGBT and diodes and the maximum temperature is much higher at IGBT power loss stage than at diodes stage. The vapour chamber can reduce the junction temperature and improve the temperature uniformity. In the stages of IGBT power loss and diodes power loss, the junction temperature decreases from 85.6 °C to 54.6 ºC and from 41.1 ºC to 31.8 ºC respectively, in comparison to the IGBT semiconductor with copper baseplate.

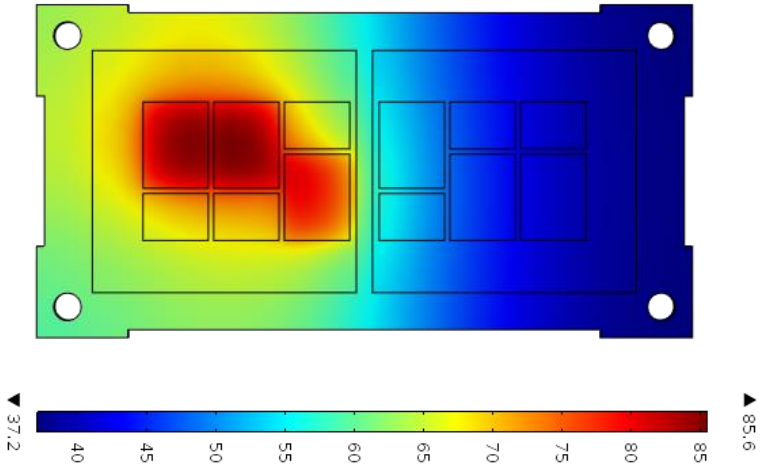

(a)

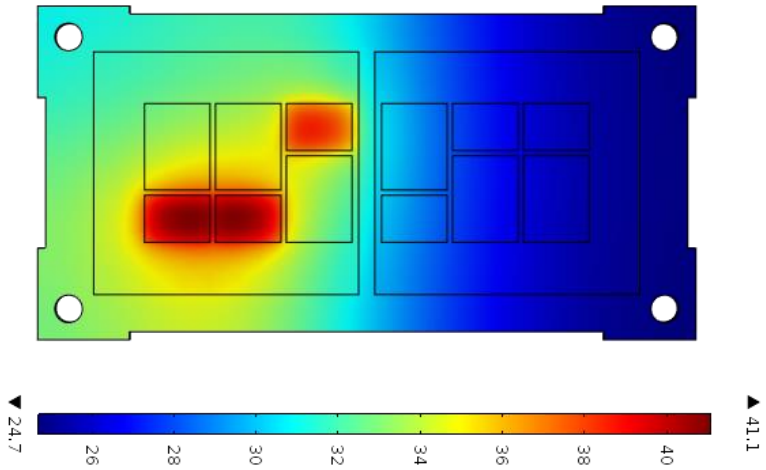

(b)

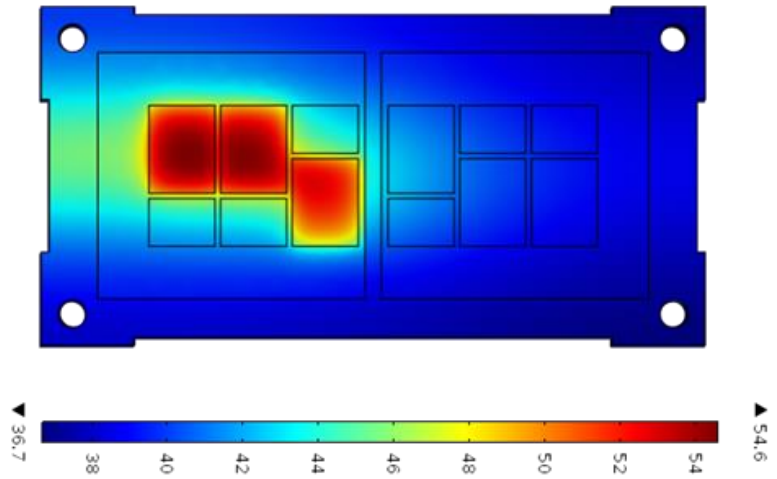

(c)

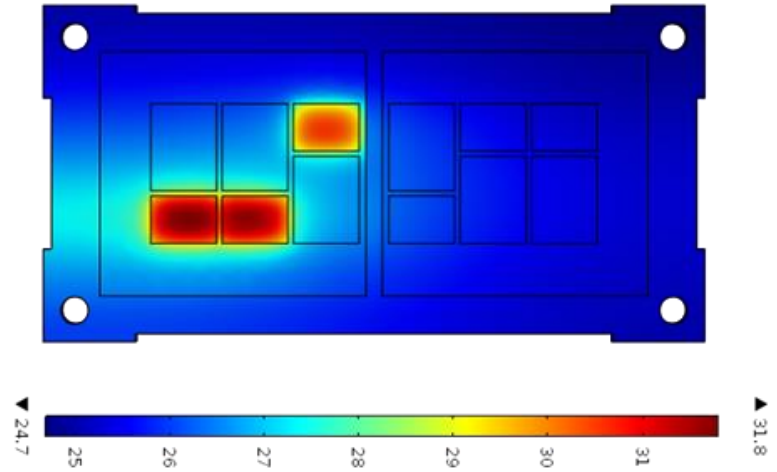

(d)

Figure 67 Temperature distribution (a) IGBT semiconductor with copper baseplate at stage of top switch igbt power loss(b) IGBT semiconductor with copper baseplate at stage of top switch diodes power loss (c) IGBT semiconductor with VC baseplate during top switch IGBT at stage of top switch igbt power loss (d) IGBT semiconductor with VC baseplate during top switch diodes at stage of top switch diodes power loss

In the simulation, the heat generated by power loss changes based on the power loss cycle. The top and bottom IGBT and diodes also don’t operate at the same

time. However, it is difficult to simulate the power loss cycle in this experiment since the switch frequency is as high as 6200 Hz. According to the experimental method developed by Parker[136], one half of total power loss of IGBT semiconductor can be used as the equivalent constant heat input in experiment. In this experiment, the simulation results are verified by the experiment results at a stationary heat input of 240 W which is one half of actual power loss.

Figure 68 shows the temperature at the junction, DCB layer, evaporation surface of vapour chamber/copper, and the condensation surface of vapour chamber/copper under different heat fluxes. In this experiment, the heat power input applied in the copper and VC cases varied from 30 W to 240 W. DCB temperature T_{DCB} is close to junction temperature T_j for both cases, since thermal resistance of chip and chip solder layer have low thermal resistances. At the applied power of 240W, the highest junction temperature for the vapour chamber case is 53 °C, which is 34.6 % lower than that for the copper case. The junction temperature for copper and VC cases obtained by the simulations are 85.6 °C and 54.6 °C respectively which are in good agreements with the experimental data. Furthermore, the vapour chamber module has a smaller temperature difference between junction and condenser surface than copper baseplate module. These results demonstrate that VC is more effective at cooling than copper baseplate.

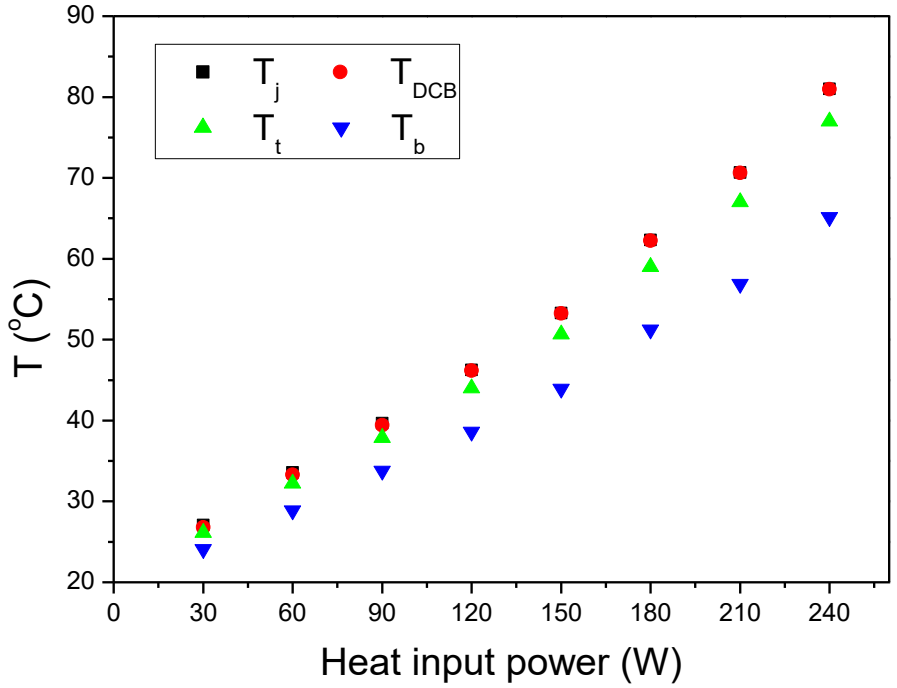

(a)

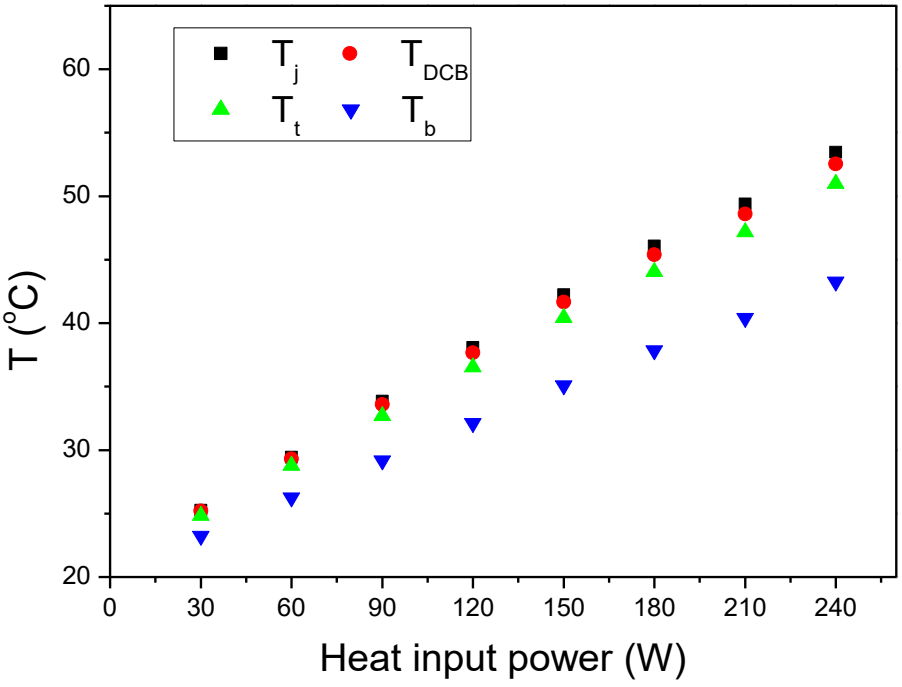

(b)

Figure 68 Temperatures measured on IGBT module under different heat input power (a) Copper baseplate (b) VC baseplate

4.3.2 Temperature uniformity

A high temperature uniformity is important for thermal management of a power modules. If a cooling device generates a non-uniform cooling performance, a large temperature variation in packaging components with different properties and size, this can cause forces at the interfaces between adjacent materials. Thus, a high temperature non-uniformity within material layers is responsible for considered to contribute to the high stresses experienced by the packaging. This will damage the reliability and efficiency of the IGBT module. Therefore, it is required to achieve uniform cooling to reduce the temperature difference to a few degrees among whole range of IGBT components in the module.

Table 18 and Table 19 show the temperature distributions on the evaporator surface of the VC and copper baseplate under different heat inputs. In general, the use of the VC leads to a much better temperature uniformity than that of copper. The temperature difference of copper and VC baseplate are 5.5 ºC and 1.3 ºC at heat power input of 240 W. Table VI gives that the temperature difference on the VC evaporator surface can be controlled within 2 ºC. The maximum temperature difference is found between T_3 and T_5. The temperature of T_3 is highest since it is in place at the centre of the vapour chamber and closest to the heat source. With increase in power input, the temperature difference increases quicker than that of VC.

The non-uniformity of temperature is mainly attributed to water cooling systems and heater. Based on heat transfer mechanism, the temperature should be the same if the measured points are located the same distance from heater. However, the experiment results show T_1 and T_2 are higher than T_4 and T_5 respectively for both VC and copper cases, which can be explained by the fact that T_1 and T_2 are

placed near the outlet of the water and T_4 and T_5 are located near inlet of the water. The temperature of the area near the water inlet is definitely lower than that of the area close to the water outlet, so more heat can be transfer to the heat sink and the area near water inlet has lower temperature. This temperature different will become larger when heat input increases.

Table 18 Temperature distributions on the copper baseplate under different heat load (Temperature accuracy= ±0.1)

	30W	60W	90W	120W	150W	180W	210W	240W
T_1 (ºC)	26.4	32.6	38.4	44.7	51.5	60.1	68.3	78.8
T_2 (ºC)	26.6	33.1	39.3	45.8	53	61.8	70.1	80.6
T_3 (ºC)	26.6	33	39.1	45.6	52.9	61.8	70.3	80.8
T_4 (ºC)	26.1	32.2	37.8	43.7	50.1	58.1	65.8	75.4
T_5 (ºC)	25.7	31.3	36.7	42.7	49	56.8	65.2	75.3

Table 19 Temperature distributions on the copper baseplate under different heat load (Temperature accuracy= ±0.1)

	30W	60W	90W	120W	150W	180W	210W	240W
T_1 (ºC)	25.4	29.4	33.2	36.9	40.6	44.1	47.1	50.9
T_2 (ºC)	25.2	29.3	33.2	37.0	40.7	44.3	47.3	51.0
T_3 (ºC)	24.0	28.8	32.7	36.9	40.8	44.6	47.8	51.5
T_4 (ºC)	24.5	28.1	31.9	35.8	39.7	43.5	46.6	50.4
T_5 (ºC)	25.2	29.1	32.9	36.6	40.3	43.7	46.7	50.4

4.3.3 Thermal resistance and heat transfer coefficient

Figure 69 shows the plots of the thermal resistance of VC (R_{VC}), the thermal resistance between chip and baseplate ($R_{th(j-c)}$), heat sink and cooling media ($R_{th(c-a)}$) and the total thermal resistance between chip and cooling media ($R_{th(j-a))}$ as a function of heat power input. The thermal resistance of copper baseplate is reduced from 0.068 K/W to 0.055 K/W with heat input power ranging between 30 W and 60 W and then it is kept between 0.045 K/W and 0.049 K/W with heat input increase from 90 W to 240 W. The thermal resistance of VC continuously decreases from 0.053 K/W to 0.027K/W when heat input ranges between 30W and 300W, which is attributed to water film recession with increase in heat input. When the heat input is low, the water film in the VC should be thick the due to the limited phase change, which leads to high evaporation and condensation thermal resistances. With an increasing the heat input, the boiling process is enhanced. More water turns into vapour by absorbing heat from the evaporator wall of the vapour chamber. Consequently, the water film becomes thinner and the evaporation and condensation thermal resistance reduces[137]. The total resistance $R_{th(j-a)}$, thermal resistance between chip and baseplate $R_{th(j-b)}$, baseplate and cooling media $R_{th(b-a)}$ also decrease with the increase in the heat input in the vapour chamber module. At the heat flux of 240W, the thermal performance of the VC is still good. Compared with the copper module, the VC module causes a 34.9%, 35.8%, 49.2% and 45.1% reduction in the thermal resistance of baseplate, $R_{th(j-b),}$ $R_{th(b-a)}$ and total thermal resistance $R_{th(j-a)}$ respectively.

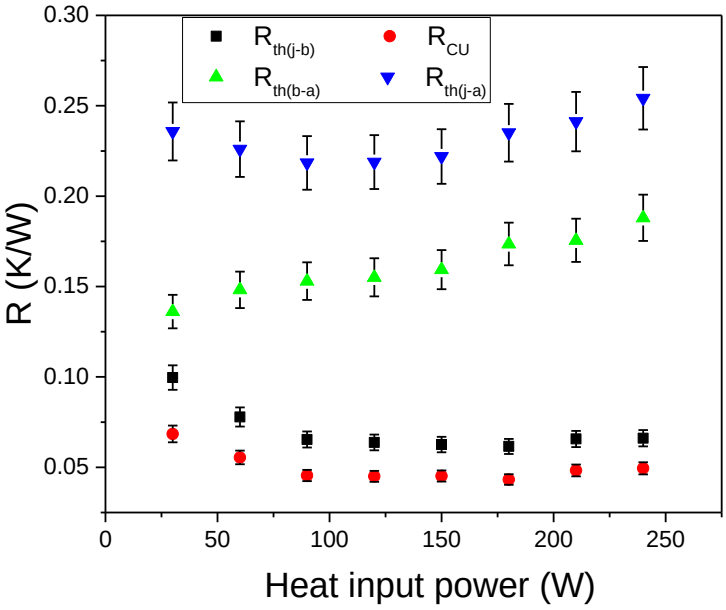

(a)

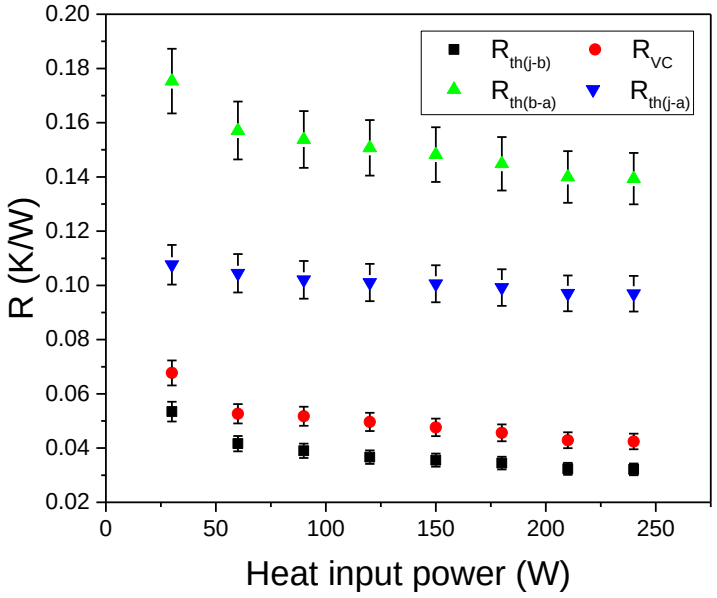

(b)

Figure 69 Thermal resistance of IGBT power module under different heat loads (a) Copper baseplate (b) VC baseplate

To evaluate the thermal performance of the baseplate heat sink, the heat transfer coefficients for the cases of the vapour chamber and copper baseplate are shown

in Table 20. The results demonstrate that the phase change heat transfer coefficient for the vapour chamber case is much higher than single phase heat transfer coefficient for copper baseplate heat sink, especially at high heat flux. The heat transfer coefficient of the vapour chamber heat sink increases with heat flux since more nucleation sites are activated.

Table 20 Baseplate heat sink transfer coefficient for copper and vapour chamber baseplate module

Heat input	30W	60W	90W	120W	150W	180W	210W	240W
CU	1333	1360	1305	1311	1296	1187	1206	1140
VC	1416	1843	1900	1884	1920	1862	1923	2069

4.3.4 Thermal stress

In general, the mismatch between two adjacent layers of a module is not uniform due to the difference of the coefficient of thermal expansions and the mismatch of the length of each layer. These generate thermal stress which leads to deformation, solder delamination, and bond wire lift off. In this case, to identify the region with highest mechanical load, Von Mises stress is used for evaluating the thermal stress distribution of the IGBT module. Figure 70 shows the von Mises stress distribution of the IGBT power module at heat transfer coefficient of 1000W/m^2K. In order to have a clear sight of thermal stress distribution in DCB, the left switch IGBT chips, diodes and solder layer are hided. The DCB layer is subjected to the highest Von Mises stress as shown in Figure 70. This is because the thermal expansion coefficient of copper is around 3 times higher than that of Al_2O_3, which is at the origin of thermal fatigue. The IGBT with

copper and vapour chamber substrates experience maximal stress of 298 MPa and 233 MPa respectively, which both occurs at the edge of ceramic layer due to the distance to neutral point (DNP) effect and geometrical singularity. This shows that there is a 20.1% reduction in thermal stress. The central region of DCB layers also suffer high stress and this is attributed to a mismatch in the length of the DCB layer and chips, and higher temperature at the centre. Also, the stress is higher at the interface between DCB and IGBT chips than at the interface between diodes and DCB because of a higher temperature gradient across IGBT chips. In particular, the highest thermal stress occurs at the edge of upper ceramic/copper interface. This indicates that the crack or peeling starts from the edge of ceramic layer and finally bifurcates and breaks the ceramic layer, which is in agreement with other studies [97, 138-140]

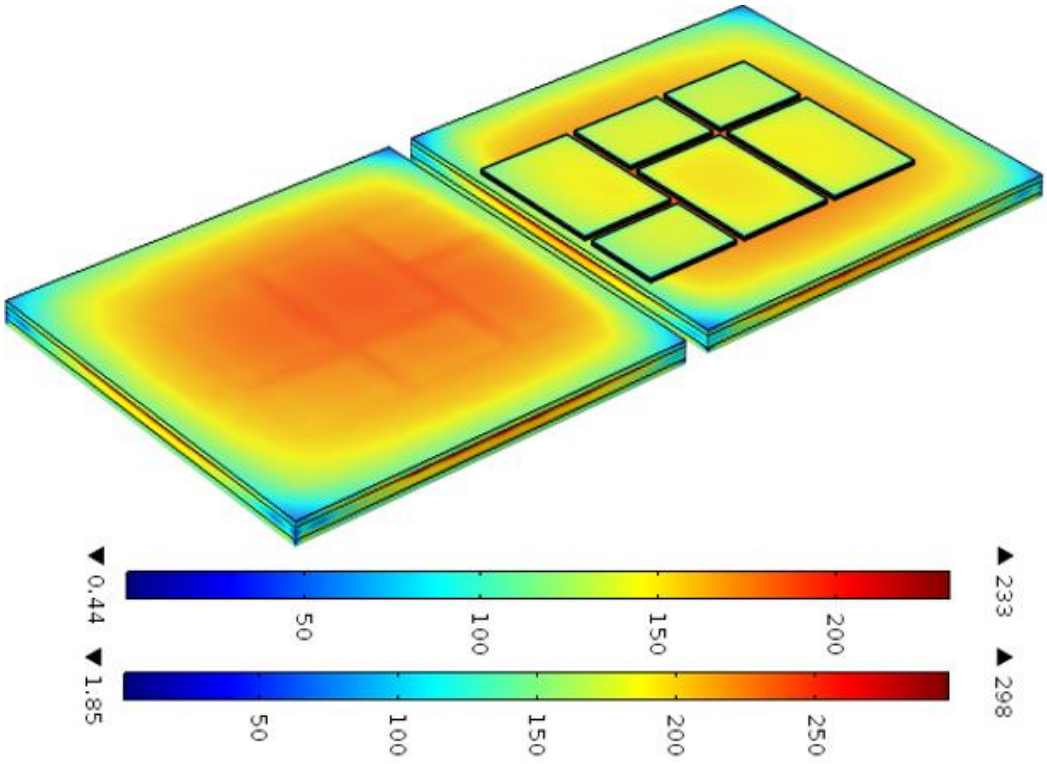

Figure 70 Von mises stress distribution. Bottom bar: IGBT with copper substrate. Top Bar: IGBT with vapour chamber substrate

Sn-3.5Ag solder has a lower melting temperature, thus yielding larger stress and higher coefficient of thermal expansion compared with other packaging layers, therefore it is more easily damaged. Figure 71 shows the peaks of component stress in Y direction (SY, also referred as peeling stress). The first principal stress (S1) is quite close to chip solder layer. This indicates that the peeling stress is the dominant factor in inducing crack initiation or failure at solder interface[141]. There is an apparent increase in the peeling stress and first principal stress at 70 minutes because of temperature variation. For the IGBTIGBTs with vapour chamber, the maximum principal stress, 47MPa, is not larger than the fracture strength of solder layer, which was 57.6MPa reported by Hwang and Vargas[142] .

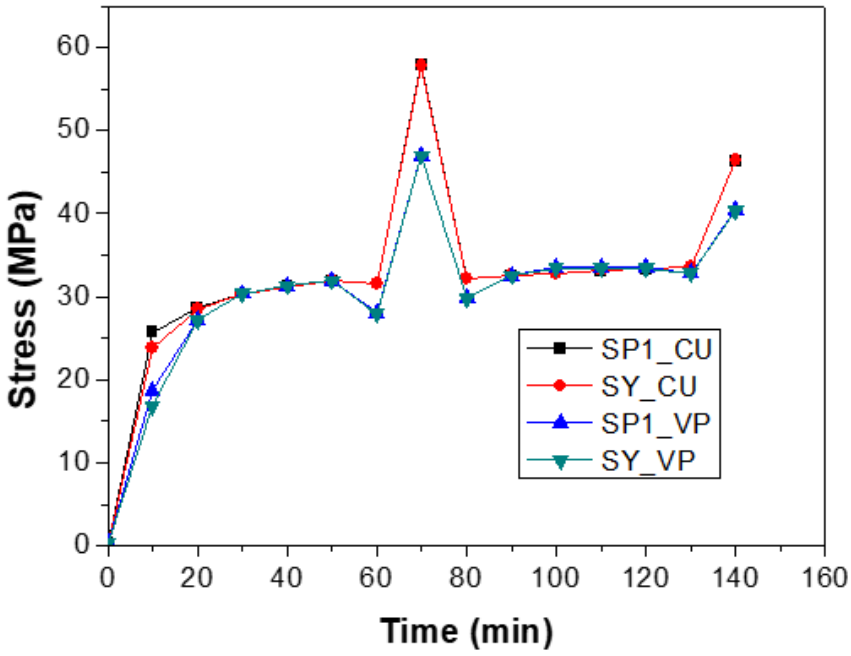

Figure 71 Peek peel (SY) and first principal (S1) stresses of Sn-3.5Ag

Under the thermal stresses, each component of IGBT power module with copper or vapour chamber substrate have a specific amount of deformation and displacement with respect to their original shape and position. Figure 72 shows

total displacement and deformation of chip solder layer. The Sn-3.5Ag solder undergoes a displacement toward the edge of the IGBT power module and bends into a convex shape under the tensile force generated by thermal stress. This is attributed to that the top surface of the solder layer is hotter than bottom surface, which forces the chip solder layers to deform in that way. The maximum displacement of 8.21 μm and 10.6 μm occur at the solder which is located at the centre for both the vapour chamber case and the copper case respectively.

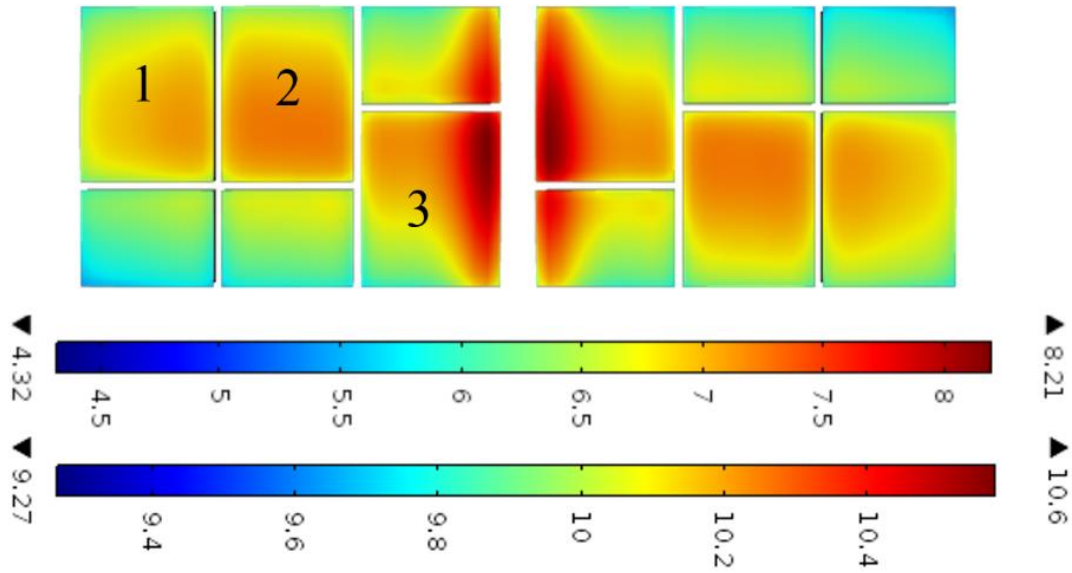

(a)

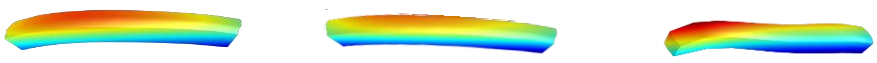

(b) First solder layer (c) Second solder layer (d) Third solder layer

Figure 72 Total displacement of solder layer [μm]

4.3.5 Energy disspation density

Generally, Sn-3.5ag chip solder layers are subjected to creep and plastic, deformation which play an important role in thermo-mechanical fatigue of materials. As shown in Figure 73, ΔW_{cr} continuiously increases from 0 MJ/m^3 to 0.194 MJ/m^3 and from 0 MJ/m^3 to 0.171 MJ/m^3 for the copper case and the vapour chamber case respectivily. It indicates that creep dissipation density drops around 11.9% when vapour chamber is integrated. As predicted by Morrow's life prediction model described in equation (46), the fatigue lifetime decreases with increasing the inelastic dissipation energy density increases. The ΔW_{cr} is about 2.6 and 3.7 times larger than ΔW_{pl} for both vapour chamber and copper cases respectively. It is found that creep is principal damage in power cycling. density

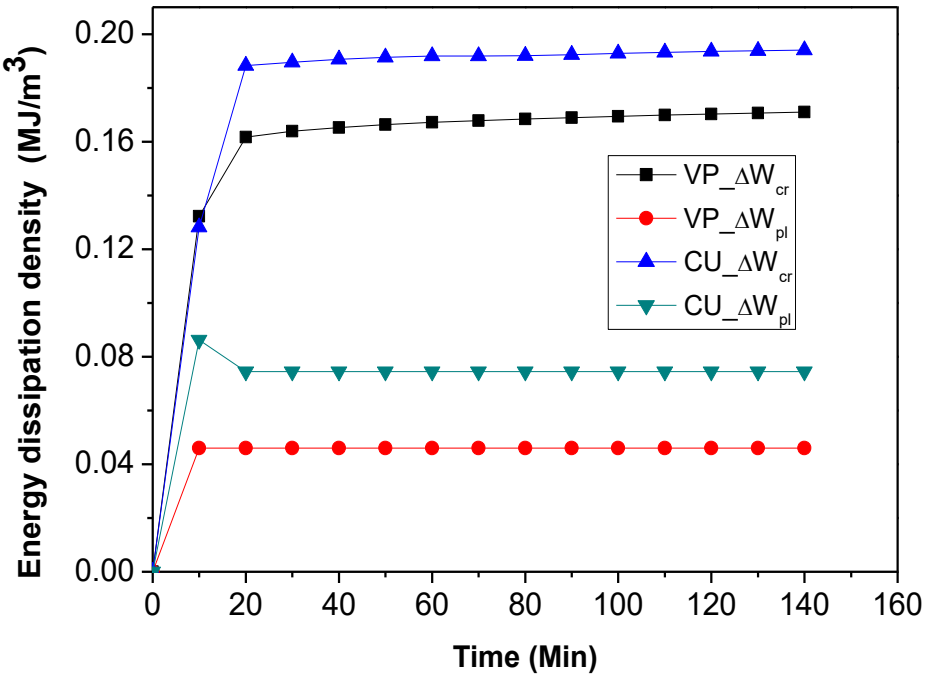

Figure 73 Energy dissipation during two thermal cycles

4.3.6 Fatigue

The lifetime of the Sn-3.5Ag solder layer is predicted. There are several models for fatigue life prediction, such as strain, stress and energy-based fatigue models. Strain distribution is more complex because each location has different strain and energy dissipation. It is difficult to obtain a representative position [143]. Moreover, the stress or strain is not sufficient to identify the fatigue properties for some cases. To improve the accuracy, the cycle to failure is estimated by using the energy-based model considering the effects of stress and strain. In some researches [129, 144-146], only creep or plastic alone was considered. Based on the analysis of the energy dissipation density, plastic, and creep are important for energy dissipation. Therefore, in this simulation, inelastic energy dissipation including creep and plastic energy is used to predict the life time. Figure 74 shows the cycles to failure of the solder layer. The minimum simulated number of cycles to failure of the vapour chamber case is 2640 which is 9% longer than the lifetime of the copper case with value of 2402.

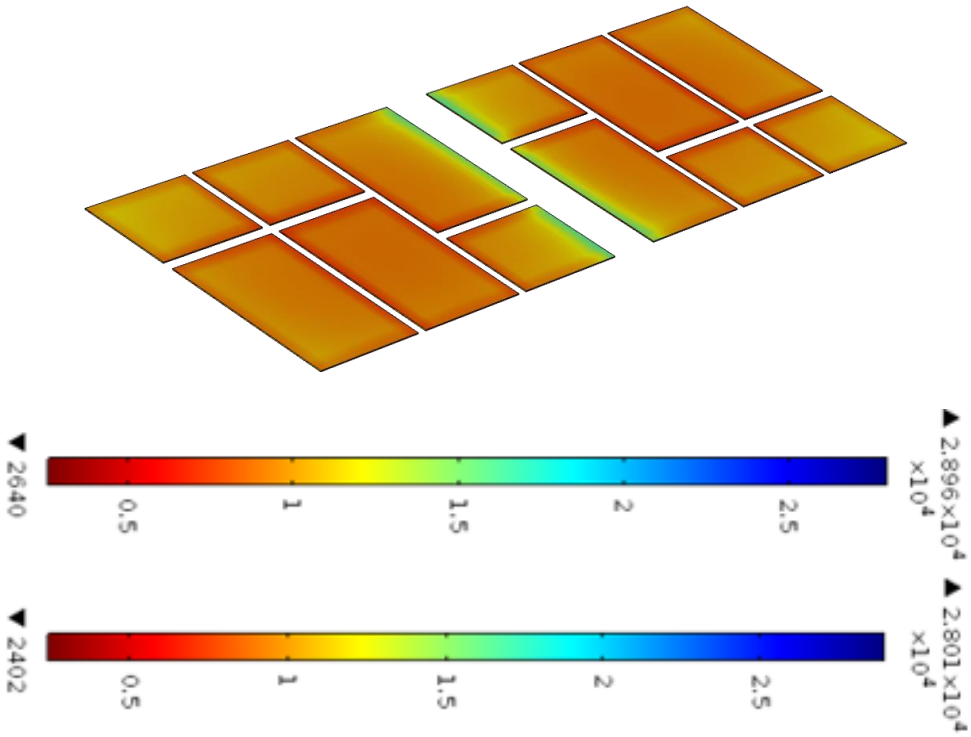

Figure 74 Cycle to failure of solder layer

4.4 Summary

In this chapter, a new IGBT power module with phase-change direct cooling is developed. This cooling strategy mainly focused on mitigating the effect of hot spots, reducing thermal resistance, increasing temperature uniformity, and improving the lifetime. In our design, the origin copper baseplate is replaced with a vapour chamber with a phase change inside of chamber original and the chamber is directly soldered onto the DBC layer. Chilled water directly cools the bottom side of the vapour chamber and removes heat away. This novel cooling strategy with compact structure and highly efficient heat transfer provides the opportunity of an individual cooling method of power electronic modules, such as MOSFETs or IGBTs.

Experiments are conducted to investigate thermal performances of the IGBT modules IGBTs integrated with a vapour chamber and original copper baseplate.

Furthermore, a computational heat transfer model is built to predict the junction temperature. Based on the results, the new IGBT power module with VC provided a higher heat dissipation efficiency and a better temperature uniformity comparing with traditional IGBT power module with a copper baseplate. At stationary heat load of 240 W, the junction temperature of IGBT with copper baseplate is up to 81.00 ˚C compared with 53.55 ˚C of vapour chamber case. High temperature uniformity is also an important for power modules since a large a temperature difference can lead to a great thermal stress, which brings many thermal reliability problems. It is demonstrated that the use of the vapour chamber can significantly enhance the uniformity of cooling. The experimental results show the temperature differences on the hotter surface of copper and VC baseplate are 5.52 ˚C and 1.29 ˚C. This indicates the vapour chamber has better temperature uniformity than a copper baseplate. It is found that the VC module reduces 34.9%, 35.8%, 44.9% and 41.6% of the thermal resistance of baseplate, Rth(j-b), Rth(b-a) and total thermal resistance Rth(j-a) respectively compared with a copper module.

The simulation of the thermo-mechanical performance under power cycling was presented. To evaluate the performance, a thermo-mechanical coupling cyclic model including creep and plastic constitutive equation was established. Based on simulation results, it helps us to have a good understanding of failure mechanisms in such an operating mode. The maximum thermal stress decreases by 20.1% compared with copper baseplate case. The highest thermal stress appears at the outermost solder layer due to its distance from neutral point and mismatch in length between solder and DBC substrate. It indicated that the cracks induced by power loading are expected to initiate at the edge. The lifetime

of the solder joint is predicted with the Morrow's life prediction model. The use of the vapour chamber can be expected to elongate the lifetime of the IGBT module under the power cycling. The simulation results suggest that the minimum number of cycles to induce the failure for the vapour chamber case is 9% larger than that for the copper baseplate case.

5. Conclusion and future work

Experimental studies characterising a novel application of phase change in thermal management of power electronics module were presented. This work was inspired by the practical application of IGBT power electronics with high heat dissipation density. It required a novel cooling strategy which has compact size and ability in the fast removal of heat whilst improving temperature uniformity in the module. This work was divided into two parts. The first part was aimed to enhance phase change heat transfer performance. The enhancement of boiling process was performed through high-speed imaging for observations of bubble nucleation and bubble dynamics and heat transfer characteristics were obtained by using boiling curves. Secondly, a novel cooling device with phase change was designed, fabricated, and tested. Heat transfer characteristics of the IGBT electronics module with cooling system were determined by measuring bulk fluid, module and cooling plate temperature.

The results related to enhanced pool boiling heat transfer on nanoparticles-coated heterogeneous wetting micro-channel surfaces lead to the following conclusions:

1. This study was conducted to investigate the heat transfer mechanisms in channel surface with three various wetting patterns. The configurations were identified as hydrophilic wetting channel surface, hydrophobic wetting surface, and heterogeneous wetting channel surface. To obtain different surface wettability, Fe_3O_4 nanoparticles with high wettability, and PDMS-silica nanoparticles with low wettability were used to deposit on the surfaces without a large change in surface roughness. The

experimental results indicated that the heterogeneous wetting channel surface improved pool boiling by affecting bubble nucleation and bubble dynamics.

2. At heat flux of 102 W/cm^2, the heat transfer coefficient for the heterogeneous wetting surface was 81.5 kW/m^{2}K, which was higher than 77.4 kW/m^{2}K, 50.4 kW/m^{2}K and 32.2 kW/m^{2}K for hydrophobic, hydrophilic wetting surfaces and bare copper surface, respectively. In addition, the hydrophobic area on the top of the fin can initiate bubble nucleation at an early stage. A lower ΔT_{ONB} of 0.7 ^oC was obtained from the heterogeneous surface compared with 6.1 ^oC for the hydrophilic wetting surface and 8.2 ^oC for a plain copper surface.
3. Based on the images captured by high speed boiling, more nucleation sites and larger bubble departure diameter were found on the top of the fin where hydrophobic nanoparticles were deposited. The inner channel surface coated with hydrophilic nanoparticles coating ensures sufficient liquid replenishment inside the channel and fast bubble departure rate.
4. The departure diameter of the bubble over the hydrophobic surface was large and it takes a long time to grow and depart. The bubble was mainly affected by necking and stretching. After the bubble departed from the surface, it left behind a small vapour remnant of the surface, indicated no waiting period for the hydrophobic time. Unlike for the hydrophobic surface, the bubble growth period was shorter and the waiting period was longer.
5. The bubble generating inside the channel had a fast bubble emission rate in the channel, which leads to more chaotic flow induced under the

bubbles generated on the top of fin. Therefore, the chaotic flow sped up bubble departure from the top fins with hydrophobic nanoparticles coating.

6. The heterogeneous wetting surfaces with various channel width of 600 µm, 1000 µm, 2000 µm, and 2500 µm were investigated. The highest heat transfer coefficient was obtained from the heterogeneous wetting surface with the 600 µm of channel width. The enhancement ratio reached up to 45 % compared with other channel surfaces. Forces for a detaching bubble were analysed. For a grown bubble, the width of channel restrict bubble growth and generated an addition upwards force to promote bubble departure.

The results related to thermal and thermo-mechanical performances of IGBT integrated with vapour chamber lead to the following conclusions:

1. A novel structure of an IGBT power module integrated with vapour chamber baseplate was designed and fabricated. The substrate of the IGBT module was integrated with a vapour chamber based heat sink and the thermal grease between the baseplate and the cooling plate was removed to reduce thermal resistance and improve temperature uniformity significantly.
2. Based on experimental results, the junction temperature of IGBT with integrated vapour chamber baseplate reduced from 81 $^{\circ}$C to 53 $^{\circ}$C compared with copper baseplate module.
3. High temperature uniformity is also an important requirement for power modules since large temperature difference increases thermal stress, which leads to many severe thermal reliability problems. Temperature

differences on the hotter surface of copper and VC baseplate are 5.5 °C and 1.3 °C. This indicates that the vapour chamber has higher temperature uniformity than copper baseplate. Besides the lower thermal resistance, the vapour chamber could also increase the heat removal rates of cooling water. IGBTs with vapour chamber modules reduced 45.1% of junction to ambient thermal resistance.

4. To evaluate the performance of the whole IGBT module integrated with a vapour chamber, a thermo-mechanical coupling power cycling model including creep and plastic constitutive equation was established. This helps us to have a good understanding of failure mechanisms in such an operating mode.
5. Simulation results show the maximum thermal stress was decreased by 20.1% compared with the copper baseplate case due to lower module temperature and uniformity temperature distribution.
6. The outermost solder layer always suffered the highest thermal stress due to its distance from neutral point effect and mismatch in length between solder and DCB substrate. Cracks induced by thermal loading are expected to initiate at the edge.
7. The failure mechanism was also investigated by comparing with creep and plastic strain energy dissipation density. Creep is the principle damage mode in the thermal cycling.
8. The lifetime of the solder joint was predicted. The minimum simulated number of cycles to failure of vapour chamber case is 9 % longer than the lifetime of copper case. An experiment was carried out to measure

the thermal performance of an IGBT integrated with a vapour chamber heat sink.

An outlook to ongoing and the future research related to this work are listed below.

1. Based on the results from chapter 3, the wick structure of vapour chambers can be improved by modification of surface wettability. The wick structure with mixed wettability could enhance the evaporation/boiling process inside the vapour chamber. The heterogeneous wetting structure could be used to benefit the IGBT thermal management system.
2. A thermography system would be considered to observe the local temperature and heat flux distribution, which can give us a better understanding on the wettability effects on boiling process.
3. In this study, only the thermal and thermo-mechanical performances were considered. The future work, however, would be to extend to test the electrical performance of IGBT integrated with a vapour chamber module.

6. Appendix

The following pictures show the experimental apparatus for pool boiling test rig and IGBT power module test rig.

The direct water cooling plate used in IGBT power module test is made by copper shown in Figure 75. It is attached to IGBT module by bolt connection and O-ring groove is designed for sealing purpose.

Figure 75 Water cooling plate for IGBT module

In IGBT test rig, IGBT module is heated by a copper heating block as shown in Figure 76. Six cartridge heaters with each power rating of 75W. The heating

block is embedded in the PEEK insulation block with low thermal conductivity of 0.25 W/mK to prevent from heat loss.

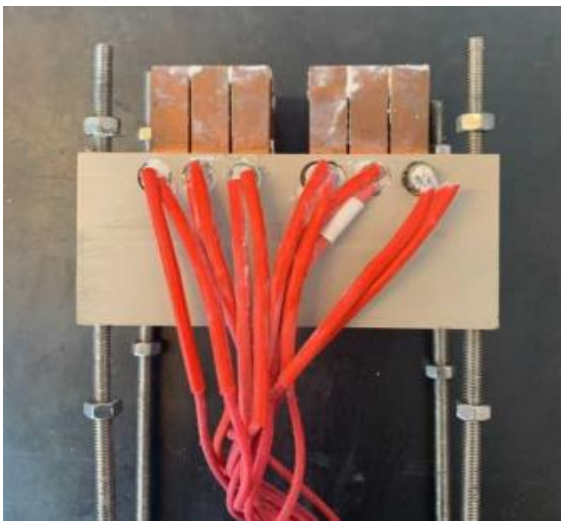

Figure 76 Copper heater with PEEK insolation cover

The rod copper heater with diameter of 25 mm and length of 100 mm is inserted into a PEEK insulation block to prevent from heat loss as shown in Figure 77 and Figure 78. Five cartridge heaters with each power rating of 175 W (H1/4X2X175, Acim Jouanin) provides heat to the boiling surface.

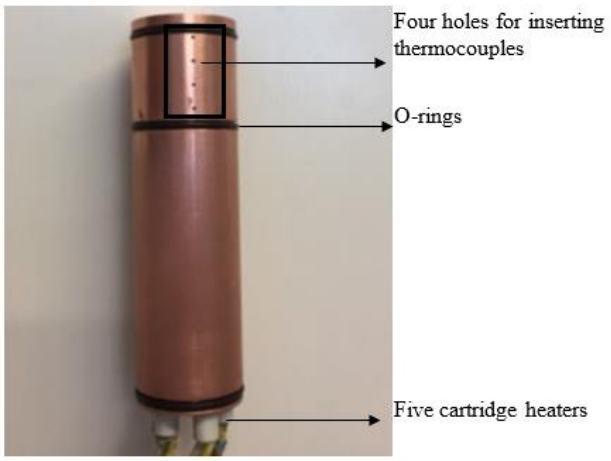

Figure 77 Heater of the pool boiling test rig

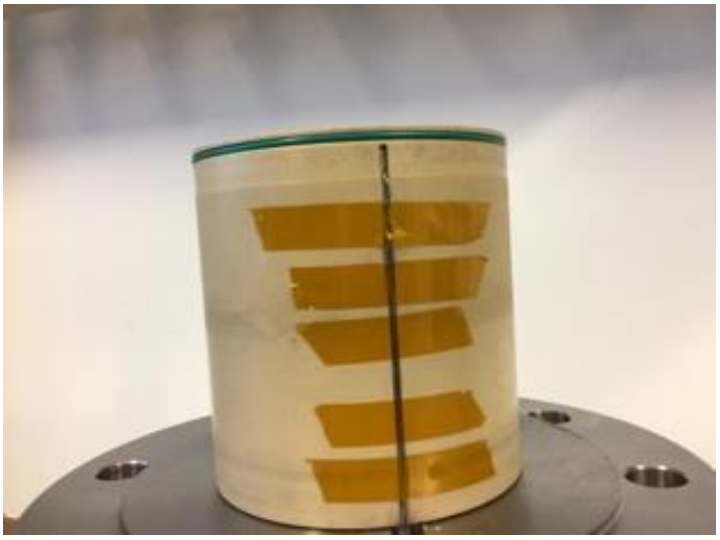

Figure 78 PEEK insulation

Figure 79 shows the main visualization boiling vessel with two view windows is shown. The main body made with steel stainless. The dimensions are 260 mm in total height and 100 mm in diameter of clear view window.

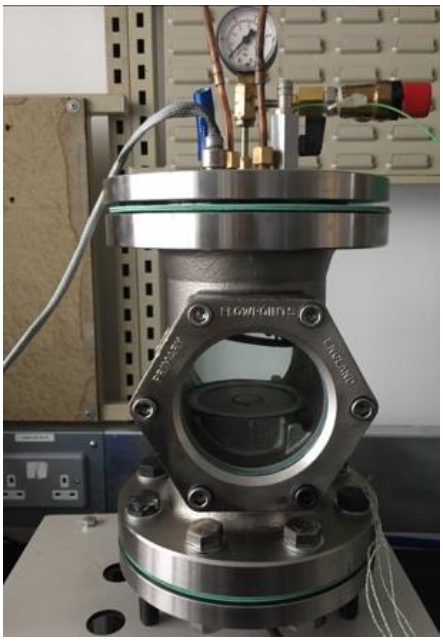

Figure 79 Steel stainless container

Figure 80 shows the reflux condenser with diameter of 75 mm and the immersion pre-heater with diameter of 100 mm and they are placed at the top of boiling surface.

Figure 80 Condenser coil and immersion pre-heater

Five copper chips with various channel width are machined by electrical discharge machining (EDM) as shown in Figure 81.

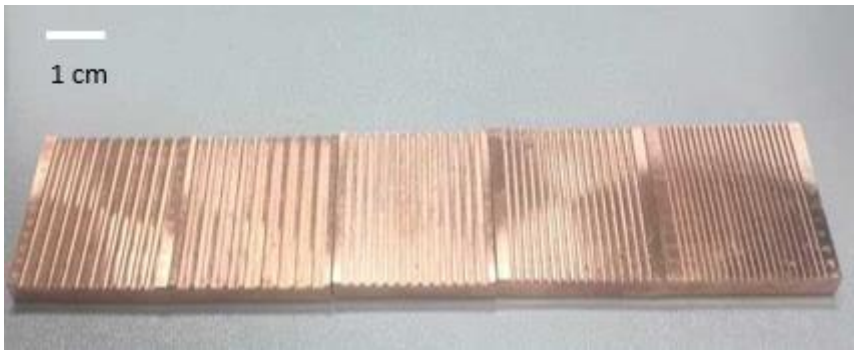

Figure 81 Tested boiling surfaces

7. Reference

1. Bergman, T.L., et al., *Fundamentals of heat and mass transfer*. 2011: John Wiley & Sons.
2. Incropera, F.P., et al., *Fundamentals of heat and mass transfer*. 2007: Wiley.
3. Jiang, L., et al., *Thermal performance of a novel porous crack composite wick heat pipe.* Energy Conversion and Management, 2014. 81: p. 10-18.
4. Li, C., G.P. Peterson, and Y. Wang, *Evaporation/Boiling in Thin Capillary Wicks (l)—Wick Thickness Effects.* Journal of Heat Transfer, 2006. 128(12): p. 1312-1319.
5. Li, C. and G.P. Peterson, *Evaporation/Boiling in Thin Capillary Wicks (II)—Effects of Volumetric Porosity and Mesh Size.* Journal of Heat Transfer, 2006. 128(12): p. 1320-1328.
6. Lefevre, F., et al., <*Experimental investigations of flat plate heat pipes with.pdf*>. Applied Thermal Engineering, 2012. 37: p. 95-102.
7. Weibel, J.A. and S.V. Garimella, *Recent Advances in Vapor Chamber Transport Characterization for High-Heat-Flux Applications.* 2013. 45: p. 209-301.
8. Gerardi, C., et al., *Experimental observation of the dynamic micro- and macro-layer during pool boiling.* Ht2008: Proceedings of the Asme Summer Heat Transfer Conference - 2008, Vol 2, 2009: p. 185-191.
9. Tong, L.S. and Y.S. Tang, *Boiling Heat Transfer And Two-Phase Flow*. 1997: Taylor & Francis.
10. *Bubble Dynamics during Capillary-Fed Nucleate Boiling in Porous Media.*
11. Jo, H., et al., *Boiling on spatially controlled heterogeneous surfaces: Wettability patterns on microstructures.* Applied Physics Letters, 2015. 106(18): p. 181602.
12. Wen, D.S. and B.X. Wang, *Effects of surface wettability on nucleate pool boiling heat transfer for surfactant solutions.* International Journal of Heat and Mass Transfer, 2002. 45(8): p. 1739-1747.
13. Takata, Y., et al., *Effect of surface wettability on boiling and evaporation.* Energy, 2005. 30(2-4): p. 209-220.
14. Zupančič, M., et al., *Enhanced pool-boiling heat transfer on laser-made hydrophobic/superhydrophilic polydimethylsiloxane-silica patterned surfaces.* Applied Thermal Engineering, 2015. 91: p. 288-297.
15. Suroto, B.J., et al., *Effects of Hydrophobic-Spot Periphery and Subcooling on Nucleate Pool Boiling from a Mixed-Wettability Surface.* Journal of Thermal Science and Technology, 2013. 8(1): p. 294-308.
16. Jo, H., et al., *A study of nucleate boiling heat transfer on hydrophilic, hydrophobic and heterogeneous wetting surfaces.* International Journal of Heat and Mass Transfer, 2011. 54(25-26): p. 5643-5652.
17. Chen, Y., et al., *Pool boiling on the superhydrophilic surface with TiO2 nanotube arrays.* Science in China Series E: Technological Sciences, 2009. 52(6): p. 1596-1600.
18. Betz, A.R., *Boiling Heat Transfer on Superhydrophilic, Superhydrophobic, and Superbiphilic Surfaces.*

19. Shen, B., et al., *Bubble activation from a hydrophobic spot at "negative" surface superheats in subcooled boiling.* Applied Thermal Engineering, 2015. 88: p. 230-236.
20. Takata, Y., S. Hidaka, and M. Kohno, *Effect of surface wettability on pool boiling: enhancement by hydrophobic coating.* International Journal of Air-Conditioning and Refrigeration, 2012. 20(01): p. 1150003.
21. Mitsutake, T., et al., *Boiling heat transfer characteristics with highly wettable heated surface under forced convection conditions.* JSME International Journal Series B Fluids and Thermal Engineering, 2004. 47(2): p. 168-172.
22. Sun, R.-D., et al., *Photoinduced surface wettability conversion of ZnO and TiO2 thin films.* The Journal of Physical Chemistry B, 2001. 105(10): p. 1984-1990.
23. Phan, H.T., et al., *Surface wettability control by nanocoating: The effects on pool boiling heat transfer and nucleation mechanism.* International Journal of Heat and Mass Transfer, 2009. 52(23-24): p. 5459-5471.
24. Kumar, C.S., Y.W. Chang, and P.-H. Chen, *Effect of heterogeneous wettable structures on pool boiling performance of cylindrical copper surfaces.* Applied Thermal Engineering, 2017. 127: p. 1184-1193.
25. Fritz, W., *Berechnung des maximalvolumes von dampfblasen.* Physik. Zeitschr, 1935. 36: p. 379-384.
26. Son, G., V.K. Dhir, and N. Ramanujapu, *Dynamics and Heat Transfer Associated With a Single Bubble During Nucleate Boiling on a Horizontal Surface.* Journal of Heat Transfer, 1999. 121(3): p. 623-631.
27. Malla, S., *Experimental investigation of nucleate boiling and thin-film evaporation on enhanced silicon surfaces.* 2014.
28. O'Hanley, H., et al., *Separate effects of surface roughness, wettability, and porosity on the boiling critical heat flux.* Applied Physics Letters, 2013. 103(2): p. 024102.
29. Betz, A.R., et al., *Do surfaces with mixed hydrophilic and hydrophobic areas enhance pool boiling?* Applied Physics Letters, 2010. 97(14): p. 141909.
30. Liaw, S.-P. and D.V.K. Dhir. *Effect of surface wettability on transition boiling heat transfer from a vertical surface*. in *International Heat Transfer Conference Digital Library*. 1986. Begel House Inc.
31. Chen, H., et al., *Experimental investigations on bubble departure diameter and frequency of methane saturated nucleate pool boiling at four different pressures.* International Journal of Heat and Mass Transfer, 2017. 112: p. 662-675.
32. Ruckenstein, E., *A physical model for nucleate boiling heat transfer.* International Journal of Heat and Mass Transfer, 1964. 7(2): p. 191-198.
33. Cole, R., *Bubble frequencies and departure volumes at subatmospheric pressures.* AIChE Journal, 1967. 13(4): p. 779-783.
34. Cole, R. and W. Rohsenow. *Correlation of bubble departure diameters for boiling of saturated liquids*. in *Chem. Eng. Prog. Symp. Ser*. 1969. 211 213.
35. Kutateladze, S. and I. Gogonin, *Growth rate and detachment diameter of a vapor bubble in free convection boiling of a saturated liquid.* Teplofizika Vysokikh Temperatur, 1979. 17: p. 792-797.

36. Jensen, M.K. and G.J. Memmel. *Evaluation of bubble departure diameter correlations*. in *International Heat Transfer Conference Digital Library*. 1986. Begel House Inc.
37. Kim, J. and M.H. Kim, *On the departure behaviors of bubble at nucleate pool boiling.* International journal of multiphase flow, 2006. 32(10-11): p. 1269-1286.
38. Fazel, S.A.A. and S.B. Shafaee, *Bubble dynamics for nucleate pool boiling of electrolyte solutions.* Journal of Heat Transfer, 2010. 132(8): p. 081502.
39. Kolev, N.I., *Bubble Departure Diameter*, in *Multiphase Flow Dynamics 2: Thermal and Mechanical Interactions*. 2007, Springer Berlin Heidelberg: Berlin, Heidelberg. p. 417-438.
40. Mikic, B.B. and W.M. Rohsenow, *A New Correlation of Pool-Boiling Data Including the Effect of Heating Surface Characteristics.* Journal of Heat Transfer, 1969. 91(2): p. 245-250.
41. Sharma, P.R., et al., *Effect of Pressure and Heat Flux on Bubble Departure Diameters and Bubble Emission Frequency*. 1996, DTIC Document.
42. Jakob, M. and W. Fritz, *Versuche über den Verdampfungsvorgang.* Forschung im Ingenieurwesen, 1931. 2(12): p. 435-447.
43. Zuber, N., *Hydrodynamic aspects of boiling heat transfer (thesis)*. 1959, California. Univ., Los Angeles; and Ramo-Wooldridge Corp., Los Angeles.
44. Peebles, F.N., *Studies on the motion of gas bubbles in liquid.* Chem. Eng. Prog., 1953. 49(2): p. 88-97.
45. Cole, R., *A photographic study of pool boiling in the region of the critical heat flux.* AIChE Journal, 1960. 6(4): p. 533-538.
46. Ivey, H., *Relationships between bubble frequency, departure diameter and rise velocity in nucleate boiling.* International Journal of Heat and Mass Transfer, 1967. 10(8): p. 1023-1040.
47. Kim, J., S. You, and J. Pak, *Effects of heater size and working fluids on nucleate boiling heat transfer.* International journal of heat and mass transfer, 2006. 49(1-2): p. 122-131.
48. Mikic, B., W. Rohsenow, and P. Griffith, *On bubble growth rates.* International Journal of Heat and Mass Transfer, 1970. 13(4): p. 657-666.
49. MALLA, S., *Experimental investigation of nucleate boiling and thin-film evaporation on enhanced silicon surfaces*, in *Mechanical Engineering*. 2014, THE UNIVERSITY OF TEXAS AT ARLINGTON.
50. Griffith, P. and J.D. Wallis, *The role of surface conditions in nucleate boiling*. 1958, Cambridge, Mass.: Massachusetts Institute of Technology, Division of Industrial Cooperation,[1958].
51. Nam, Y., et al., *Experimental and Numerical Study of Single Bubble Dynamics on a Hydrophobic Surface.* Journal of Heat Transfer, 2009. 131(12): p. 121004-121004.
52. Gerardi, C., et al., *Study of bubble growth in water pool boiling through synchronized, infrared thermometry and high-speed video.* International Journal of Heat and Mass Transfer, 2010. 53(19-20): p. 4185-4192.
53. Phan, H.T., et al., *How does surface wettability influence nucleate boiling?* Comptes Rendus Mécanique, 2009. 337(5): p. 251-259.

54. Nam, Y., et al., *Single bubble dynamics on a superhydrophilic surface with artificial nucleation sites.* International Journal of Heat and Mass Transfer, 2011. 54(7-8): p. 1572-1577.
55. Schweizer, N., *Multi-Scale Investigation of Nucleate Boiling Phenomena in Microgravity*, in *Institute of Technical Thermodynamics*. 2010, Universitäts- und Landesbibliothek Darmstadt tuprints: Universitäts- und Landesbibliothek Darmstadt tuprints. p. 156.
56. Sielaff, A., *Experimental Investigation of Single Bubbles and Bubble Interactions in Nucleate Boiling*, in *Institut für Technische Thermodynamik*. 2014, Technische Universität Darmstadt: Darmstadt. p. 154.
57. Zhao, Y.-H., T. Masuoka, and T. Tsuruta, *Unified theoretical prediction of fully developed nucleate boiling and critical heat flux based on a dynamic microlayer model.* International Journal of Heat and Mass Transfer, 2002. 45(15): p. 3189-3197.
58. Wiesbaden, S.F.a., *Experimental Investigation of Heat Transfer during Evaporation in the Vicinity of Moving Three-Phase Contact Lines*, in *Institut für Technische Thermodynamik*. 2015, Technische Universität Darmstadt: Technische Universität Darmstadt. p. 132.
59. Cooper, M.G., A.J.P. Lloyd, *The Microlayer in Nucleate Pool Boiling.* International Journal of Heat and Mass Transfer, 1969.
60. Utaka, Y., Y. Kashiwabara, and M. Ozaki, *Microlayer structure in nucleate boiling of water and ethanol at atmospheric pressure.* International Journal of Heat and Mass Transfer, 2013. 57(1): p. 222-230.
61. Fridrikhson, Y.V., V.Y. Kravets, and M.G. Semena, *Calculation of the density of active nucleation sites in the boiling of liquids on metal-fibrous capillary-porous structures.* Journal of Engineering Physics and Thermophysics, 1994. 66(5): p. 534-540.
62. *Calculation of Active Nucleation Site Density in Boiling Systems.*
63. Gaertner, R.F., *Photographic Study of Nucleate Pool Boiling on a Horizontal Surface.* Journal of Heat Transfer, 1965. 87(1): p. 17-27.
64. Chen, R., et al., *Nanowires for Enhanced Boiling Heat Transfer.* Nano Letters, 2009. 9(2): p. 548-553.
65. Kandlikar, S.G., *A Theoretical Model to Predict Pool Boiling CHF Incorporating Effects of Contact Angle and Orientation.* Journal of Heat Transfer, 2001. 123(6): p. 1071.
66. Rahman, M.M., J. Pollack, and M. McCarthy, *Increasing Boiling Heat Transfer using Low Conductivity Materials.* Sci Rep, 2015. 5: p. 13145.
67. Mentor, *POWER CYCLING & THERMAL RELIABILITY OF AUTOMOTIVE IGBTS*. 2015, Mentor Graphics Corporation.
68. McGlen, R.J., R. Jachuck, and S. Lin, *Integrated thermal management techniques for high power electronic devices.* Applied thermal engineering, 2004. 24(8-9): p. 1143-1156.
69. Bhunia, A., S. Chandrasekaran, and C.-L. Chen, *Performance improvement of a power conversion module by liquid micro-jet impingement cooling.* IEEE Transactions on Components and Packaging Technologies, 2007. 30(2): p. 309-316.
70. Issam Mudawar, D.B., Kenneth Kelly, and Sreekant Narumanchi, *Two-Phase Spray Cooling of Hybrid Vehicle Electronics.* IEEE Transactions

On Components And Packaging Technologies,, 2009. VOL. 32: p. 501-512.
71. Wang, P., P. McCluskey, and A. Bar-Cohen, *Two-Phase Liquid Cooling for Thermal Management of IGBT Power Electronic Module.* Journal of Electronic Packaging, 2013. 135(2): p. 021001.
72. Mertens, R.G., et al., *Spray cooling of IGBT devices.* Journal of Electronic Packaging, 2007. 129(3): p. 316-323.
73. Crisafulli, V., *IGBT Technologies and Applications Overview: How and When to Use an IGBT* 2018, On Semiconductor.
74. Morozumi, A., et al. *Direct liquid cooling module with high reliability solder joining technology for automotive applications*. in *2013 25th International Symposium on Power Semiconductor Devices & IC's (ISPSD)*. 2013. IEEE.
75. Biela, J., et al. *SiC vs. Si-evaluation of potentials for performance improvement of power electronics converter systems by SiC power semiconductors*. in *Materials Science Forum*. 2010. Trans Tech Publ.
76. Gohara, H., et al. *Next-gen IGBT module structure for hybrid vehicle with high cooling performance and high temperature operation*. in *PCIM Europe 2014; International Exhibition and Conference for Power Electronics, Intelligent Motion, Renewable Energy and Energy Management*. 2014. VDE.
77. Kuang, S., B.W. Williams, and S.J. Finney, *A review of IGBT models.* IEEE Transactions on Power Electronics, 2000. 15(6): p. 1250-1266.
78. Mohammed, S.A., M. Abdel-Moamen, and B. Hasanin, *A review of the state-of-the-art of power electronics for power system applications.* Quest Journal of Electronics and Communication Engineering Research (JECER), 2013. 1(1): p. 43-52.
79. Qian, C., et al., *Thermal management on IGBT power electronic devices and modules.* IEEE Access, 2018. 6: p. 12868-12884.
80. Oh, H., et al., *Physics-of-failure, condition monitoring, and prognostics of insulated gate bipolar transistor modules: A review.* IEEE Transactions on power electronics, 2014. 30(5): p. 2413-2426.
81. Xu, C., C. Gang, and M. Sakane, *Prediction of stress-strain relationship with an improved Anand constitutive Model For lead-free solder Sn-3.5Ag.* IEEE Transactions on Components and Packaging Technologies, 2005. 28(1): p. 111-116.
82. Medjahed, H., P.-E. Vidal, and B. Nogarede, *Thermo-mechanical stress of bonded wires used in high power modules with alternating and direct current modes.* Microelectronics Reliability, 2012. 52(6): p. 1099-1104.
83. *U.S. Air Force Avionics Integrity Program (AVIP) notes*. 1989.
84. *The Market for Thermal Management Technologies*. 2016, Research and markets.
85. Drive, U., *Electrical and electronics technical team roadmap.* Partnership Plan, Roadmaps, and Other Documents, 2013.
86. Kandlikar, S.G. and C.N. Hayner, *Liquid Cooled Cold Plates for Industrial High-Power Electronic Devices—Thermal Design and Manufacturing Considerations.* Heat Transfer Engineering, 2009. 30(12): p. 918-930.

87. Yin, S., K.J. Tseng, and J. Zhao, *Design of AlN-based micro-channel heat sink in direct bond copper for power electronics packaging.* Applied Thermal Engineering, 2013. 52(1): p. 120-129.
88. Stevanovic, L., et al., *Integral Micro-channel Liquid Cooling for Power Electronics*. 2010. 1591-1597.
89. Vafai, K. and L. Zhu, *Analysis of two-layered micro-channel heat sink concept in electronic cooling.* International Journal of Heat and Mass Transfer, 1999. 42(12): p. 2287-2297.
90. Naqiuddin, N.H., et al., *Overview of micro-channel design for high heat flux application.* Renewable and Sustainable Energy Reviews, 2018. 82: p. 901-914.
91. Jörg, J., et al., *Direct single impinging jet cooling of a MOSFET power electronic module.* IEEE Transactions on Power Electronics, 2017.
92. Bhunia, A. and C. Chen, *On the scalability of liquid microjet array impingement cooling for large area systems.* Journal of Heat Transfer, 2011. 133(6): p. 064501.
93. Gould, K., et al., *Liquid jet impingement cooling of a silicon carbide power conversion module for vehicle applications.* IEEE Transactions on Power Electronics, 2015. 30(6): p. 2975-2984.
94. Oliphant, K., B. Webb, and M. McQuay, *An experimental comparison of liquid jet array and spray impingement cooling in the non-boiling regime.* Experimental Thermal and Fluid Science, 1998. 18(1): p. 1-10.
95. Fabbri, M., S. Jiang, and V.K. Dhir. *Experimental investigation of single-phase micro jets impingement cooling for electronic applications*. in *Proceedings of the HT2003 ASME Summer Heat Transfer Conference, July*. 2003.
96. Bhunia, A., Q. Cai, and C.-L. Chen. *Liquid impingement and phase change for high power density electronic cooling*. in *Proceeding of the 41st AIAA Aerospace Sciences Meeting and Exhibit, Reno, NV, January*. 2003.
97. Dupont, L., *Contribution à l'étude de la durée de vie des assemblages de puissance dans des environnements haute température et avec des cycles thermiques de grande amplitude*. 2006, École normale supérieure de Cachan-ENS Cachan.
98. Howes, J.C., et al. *Cooling of an IGBT drive system with vaporizable dielectric fluid (VDF)*. in *2008 Twenty-fourth Annual IEEE Semiconductor Thermal Measurement and Management Symposium*. 2008. IEEE.
99. Lee, T.-Y., *Design optimization of an integrated liquid-cooled IGBT power module using CFD technique.* IEEE Transactions on Components and Packaging Technologies, 2000. 23(1): p. 55-60.
100. Bostanci, H., et al., *Thermal management of power inverter modules at high fluxes via two-phase spray cooling.* IEEE Transactions on Components, Packaging and Manufacturing Technology, 2012. 2(9): p. 1480-1485.
101. Semikron, *Semikron 600 V IGBT Advanced Drive System Preliminary Data Sheet*. 2004, Semikron Inc: Hudson, NH.
102. Gillot, C., et al., *Double-sided cooling for high power IGBT modules using flip chip technology*. IEEE Transactions on components and packaging technologies, 2001. 24(4): p. 698-704.

103. Turek, L.J., et al. *Evaporative spray cooling of power electronics using high temperature coolant*. in *2008 11th Intersociety Conference on Thermal and Thermomechanical Phenomena in Electronic Systems*. 2008. IEEE.
104. Fu, R., et al., *Experimental investigation of turbulent forced heat transfer of Fe3O4 ethylene glycol–Water nanofluid with highly disaggregated particles.* Thermal Science and Engineering Progress, 2019. 10: p. 1-9.
105. Gao, N., et al., *Superhydrophobic composite films based on THS and nanoparticles.* Journal of Bionic Engineering, 2010. 7(4): p. S59-S66.
106. Young, T. *An essay on the cohesion of fluids*. in *Abstracts of the Papers Printed in the Philosophical Transactions of the Royal Society of London*. 1832. The Royal Society London.
107. Moffat, R.J., *Describing the uncertainties in experimental results.* Experimental Thermal and Fluid Science, 1988. 1(1): p. 3-17.
108. Patil, C.M., K. Santhanam, and S.G. Kandlikar, *Development of a two-step electrodeposition process for enhancing pool boiling.* International Journal of Heat and Mass Transfer, 2014. 79: p. 989-1001.
109. Wang, Y.-Q., et al., *Wettability modification to further enhance the pool boiling performance of the micro nano bi-porous copper surface structure.* International Journal of Heat and Mass Transfer, 2018. 119: p. 333-342.
110. Akbari, E., et al., *Effect of silver nanoparticle deposition in re-entrant inclined minichannel on bubble dynamics for pool boiling enhancement.* Experimental Thermal and Fluid Science, 2017. 82: p. 390-401.
111. Gheitaghy, A.M., H. Saffari, and G.Q. Zhang, *Effect of Nanostructured Microporous Surfaces on Pool Boiling Augmentation.* Heat Transfer Engineering, 2019. 40(9-10): p. 762-771.
112. Mori, S. and K. Okuyama, *Enhancement of the critical heat flux in saturated pool boiling using honeycomb porous media.* International Journal of Multiphase Flow, 2009. 35(10): p. 946-951.
113. Dhir, V.K., *Nucleation site density*. Vol. 15. 2003. 315-321.
114. Wang, C. and V. Dhir, *Effect of surface wettability on active nucleation site density during pool boiling of water on a vertical surface.* Journal of Heat Transfer, 1993. 115(3): p. 659-669.
115. Ambrose, S., *The rise of Taylor bubbles in vertical pipes*, in *Department of Chemical and Environmental Engineering*. 2015, University of Nottingham: Nottingham.
116. Zuber, N., *Nucleate boiling. The region of isolated bubbles and the similarity with natural convection.* International Journal of Heat and Mass Transfer, 1963. 6(1): p. 53-78.
117. Mizo, V.R., *Investigation of inertia controlled bubble departure mechanism in subcooled flow boiling using high speed photography.* 1995.
118. Chien, L.-H. and R.L. Webb, *Measurement of bubble dynamics on an enhanced boiling surface.* Experimental thermal and fluid science, 1998. 16(3): p. 177-186.
119. Hatton, A. and I. Hall. *Photographic study of boiling on prepared surfaces*. in *International Heat Transfer Conference Digital Library*. 1966. Begel House Inc.

120. Kong, X., Y. Zhang, and J. Wei, *Experimental study of pool boiling heat transfer on novel bistructured surfaces based on micro-pin-finned structure.* Experimental Thermal and Fluid Science, 2018. 91: p. 9-19.
121. Kurose, R., R. Misumi, and S. Komori, *Drag and lift forces acting on a spherical bubble in a linear shear flow.* International journal of multiphase flow, 2001. 27(7): p. 1247-1258.
122. Li, Y., et al., *Thermal responses of heat pipes with different wick structures under variable centrifugal accelerations.* Applied Thermal Engineering, 2016. 96: p. 352-363.
123. Li, Y., et al., *Thermal performance of ultra-thin flattened heat pipes with composite wick structure.* Applied Thermal Engineering, 2016. 102: p. 487-499.
124. Li, Y., et al., *Experimental investigation of vapor chambers with different wick structures at various parameters.* Experimental Thermal and Fluid Science, 2016. 77: p. 132-143.
125. Avenas, Y., et al. *On the use of flat heat pipes as thermal spreaders in power electronics cooling*. in *Power Electronics Specialists Conference, 2002. pesc 02. 2002 IEEE 33rd Annual*. 2002. IEEE.
126. Ivanova, M., et al., *Heat pipe integrated in direct bonded copper (DBC) technology for cooling of power electronics packaging.* IEEE Transactions on Power electronics, 2006. 21(6): p. 1541-1547.
127. Bose, J.R., N. Ahammed, and L.G. Asirvatham, *Thermal performance of a vapor chamber for electronic cooling applications.* Journal of Mechanical Science and Technology, 2017. 31(4): p. 1995-2003.
128. Wong, S.-C., et al., *A novel vapor chamber and its performance.* International Journal of Heat and Mass Transfer, 2010. 53(11): p. 2377-2384.
129. Barbagallo, C., et al., *Thermal fatigue life evaluation of SnAgCu solder joints in a multi-chip power module.*
130. Wen, S.S. and G.-Q. Lu. *Finite element modeling of heat transfer and thermal stresses for three-dimensional packaging of power electronics modules*. in *Power Electronics and Motion Control Conference, 2000. Proceedings. IPEMC 2000. The Third International*. 2000. IEEE.
131. Wang, D., Y. Yuan, and L. Luo. *Failure analysis of Sn-3.5 Ag solder joints for FCOB using 2-D FEA model*. in *Electronic Packaging Technology & High Density Packaging (ICEPT-HDP), 2010 11th International Conference on*. 2010. IEEE.
132. Busca, C. *Modeling lifetime of high power IGBTs in wind power applications-An overview*. in *Industrial Electronics (ISIE), 2011 IEEE International Symposium on*. 2011. IEEE.
133. Choi, U.-M., F. Blaabjerg, and K.-B. Lee, *Study and handling methods of power IGBT module failures in power electronic converter systems.* IEEE Transactions on Power Electronics, 2015. 30(5): p. 2517-2533.
134. Xu, Z., et al. *Si IGBT phase-leg module packaging and cooling design for operation at 200 °C in hybrid electrical vehicle applications*. in *2012 Twenty-Seventh Annual IEEE Applied Power Electronics Conference and Exposition (APEC)*. 2012.
135. Avenas, Y., L. Dupont, and Z. Khatir, *Temperature measurement of power semiconductor devices by thermo-sensitive electrical*

parameters—A review. IEEE Transactions on Power Electronics, 2012. 27(6): p. 3081-3092.
136. Saums, D.L. *Vaporizable dielectric fluid cooling for IGBT power semiconductors*. in *Integrated Power Electronics Systems (CIPS), 2010 6th International Conference on*. 2010. IEEE.
137. Tang, Y., et al., *A multi-artery vapor chamber and its performance.* Applied Thermal Engineering, 2013. 60(1-2): p. 15-23.
138. Pietranico, S., et al., *Thermal fatigue and failure of electronic power device substrates.* International Journal of Fatigue, 2009. 31(11): p. 1911-1920.
139. Cotterell, B. and J. Rice, *Slightly curved or kinked cracks.* International journal of fracture, 1980. 16(2): p. 155-169.
140. Jouini, Z., Z. Valdez-Nava, and D. Malec, *Failure Analysis of Ceramic Substrates Used in High Power IGBT Modules.* Engineering, 2016. 8(09): p. 561.
141. Chong, D.Y.R., et al., *Evaluation on Influencing Factors of Board-Level Drop Reliability for Chip Scale Packages (Fine-Pitch Ball Grid Array).* IEEE Transactions on Advanced Packaging, 2008. 31(1): p. 66-75.
142. Hwang, J. and R. Vargas, *Solder joint reliability—Can solder creep?* Soldering & Surface Mount Technology, 1990. 2(2): p. 38-45.
143. Kim, I. and S.-B. Lee. *Fatigue life evaluation of lead-free solder under thermal and mechanical loads*. in *Electronic Components and Technology Conference, 2007. ECTC'07. Proceedings. 57th*. 2007. IEEE.
144. Syed, A. *Accumulated creep strain and energy density based thermal fatigue life prediction models for SnAgCu solder joints*. in *Electronic Components and Technology Conference, 2004. Proceedings. 54th*. 2004. IEEE.
145. Schubert, A., et al. *Fatigue life models for SnAgCu and SnPb solder joints evaluated by experiments and simulation*. in *Electronic Components and Technology Conference, 2003. Proceedings. 53rd*. 2003. IEEE.
146. Shi, X., et al., *A modified energy-based low cycle fatigue model for eutectic solder alloy.* Scripta Materialia, 1999. 41(3): p. 289-296.